The Dissertation Committee for Bohua Li Certifies
that this is the approved version of the following dissertation:

Cosmology in a Universe with Bose-Einstein-Condensed Scalar Field Dark Matter

Committee:

Paul R. Shapiro, Supervisor

Tanja Rindler-Daller

Karl Gebhardt

Milos Milosavljevic

Can Kilic

Cosmology in a Universe with Bose-Einstein-Condensed Scalar Field Dark Matter

by

Bohua Li

DISSERTATION

Presented to the Faculty of the Graduate School of

The University of Texas at Austin

in Partial Fulfillment

of the Requirements

for the Degree of

DOCTOR OF PHILOSOPHY

THE UNIVERSITY OF TEXAS AT AUSTIN

August 2017

Acknowledgments

I wish to thank the multitudes of people who helped me along this path. Time would fail me to tell of the numerous occasions I benefitted from scientific discussions and collaboration with my PhD advisor, Dr. Paul R. Shapiro, and my collaborator, Dr. Tanja Rindler-Daller. It would not possible for me to reach this goal without their dedicated instructions, counsel, and encouragement, both inside and outside academia. In addition, I would like to thank all my committee members, Karl, Milos and Can, for their constructive comments on our work and career advice provided to me during these years. I would also like to thank my parents for their steadfast support and sympathetic ear. You are always there for me, no matter what condition I was in or what challenge I went thru.

For Chapter 1, my collaborators and I are grateful for helpful discussions with Can Kilic, Dustin Lorshbough, Tonatiuh Matos and Eiichiro Komatsu. This work was supported in part by NSF grant AST-1009799 and NASA grant NNX11AE09G to my advisor, Paul R. Shapiro.

For Chapter 2, we benefitted from discussions with many people to whom we express our gratitude: Joel Meyers, Dustin Lorshbough, Aditya Aravind, Thomas Crawford, Can Kilic, Raphael Flauger, Takeshi Kobayashi, and Eiichiro Komatsu. We thank Paul Lasky especially for sharing his code for plotting current experimental constraints on the present-day SGWB background. We are grateful to members of the LIGO Scientific Collaboration for helpful discussion, including Tania Regimbau and David Reitze. We give special thanks

to Joseph Romano for sharing his code for computing aLIGO/Virgo sensitivity and the signal-to-noise ratios for a stochastic background of GWs with a power-law spectra. We modified this code to compute these for the non-power-law spectrum of the SGWB from inflation in our ΛSFDM model. We are grateful to Andrew Matas and the LIGO Scientific Collaboration for providing us with the noise characteristics for the O1 run and to Joseph Romano, again, for helping us to interpret it. This work was supported in part by U.S. NSF grant AST-1009799, NASA grant NNX11AE09G, NASA/JPL grant RSA Nos.1492788 and 1515294, and supercomputer resources from NSF XSEDE grant TG-AST090005 and the Texas Advanced Computing Center (TACC) at the University of Texas at Austin.

Thank you very much, everyone!

Bohua Li

Austin, August 8, 2017.

Cosmology in a Universe with Bose-Einstein-Condensed Scalar Field Dark Matter

Bohua Li, Ph.D.
The University of Texas at Austin, 2017

Supervisor: Paul R. Shapiro

We consider an alternative to WIMP cold dark matter (CDM), ultralight bosonic dark matter ($m \gtrsim 10^{-22}\mathrm{eV}/c^2$) described by a complex scalar field (SFDM) with a global $U(1)$ symmetry, for which the comoving particle number density, or charge density, is conserved after particle production during standard reheating. We allow for a repulsive self-interaction. In a ΛSFDM universe, SFDM starts relativistic, evolving from stiff ($w = 1$) to radiation-like ($w = 1/3$), before becoming nonrelativistic at late times ($w = 0$). Thus, before the familiar radiation-dominated era, there is an earlier era of stiff-SFDM-domination. During both the stiff-SFDM-dominated and radiation-dominated eras, the expansion rate is *higher* than in ΛCDM. SFDM particle mass m and quartic self-interaction coupling strength λ, are therefore constrained by cosmological observables, particularly N_{eff}, the effective number of neutrino species during BBN, and z_{eq}, the redshift of matter-radiation equality. Furthermore, since the stochastic gravitational wave background (SGWB) from inflation is amplified during the stiff-SFDM-dominated era, it can contribute a radiationlike component large enough to affect these observables, by further boosting the expansion rate after the stiff era ends. Remarkably, this same amplification makes detection of the SGWB possible at high frequencies by

current laser interferometer experiments, e.g., aLIGO/Virgo and LISA. For SFDM particle parameters that satisfy these cosmological constraints, the amplified SGWB is detectable by LIGO for a broad range of reheat temperatures $T_{\rm reheat}$, for values of the tensor-to-scalar ratio r currently allowed by CMB polarization measurements. For a given r and $\lambda/(mc^2)^2$, the marginally-allowed ΛSFDM model for each $T_{\rm reheat}$ has the smallest m that satisfies the cosmological constraints, and maximizes the present SGWB energy density for that $T_{\rm reheat}$. This SGWB is then maximally *detectable* for values of $T_{\rm reheat}$ for which modes that reenter the horizon when reheating ended have frequencies today that lie within the LIGO sensitive band. For example, for the family of marginally-allowed models with $r = 0.01$ and $\lambda/(mc^2)^2 = 10^{-18}$ eV^{-1}cm^3, the maximally detectable ΛSFDM model has $T_{\rm reheat} \simeq 2 \times 10^4$ GeV and $m \simeq 1.6 \times 10^{-19}$ eV$/c^2$, for which we predict an aLIGO O1 run detection with signal-to-noise ratio of ~ 10. We show that the null detection of the SGWB recently reported by the aLIGO O1 run excludes the parameter range $8.75 \times 10^3 \lesssim T_{\rm reheat}$ (GeV) $\lesssim 1.7 \times 10^5$ for this illustrative family at 95% confidence, thereby demonstrating that GW detection experiments can already place a new kind of cosmological constraint on SFDM. A wider range of SFDM parameters and reheat temperatures should be accessible to aLIGO/Virgo O5, with the potential to detect this unique signature of the ΛSFDM model. For this same illustrative family, for example, a 3σ detection is predicted for $600 \lesssim T_{\rm reheat}$ (GeV) $\lesssim 10^7$.

Table of Contents

List of Tables

List of Figures

Chapter 1

Scalar Field Dark Matter Cosmology[1]

1.1 Introduction

1.1.1 Cold dark matter

Since the discovery of the accelerating expanding Universe, ΛCDM has become the standard cosmological model as supported by various astronomical observations. Cosmic microwave background (CMB) observations have shown that about 25% of the energy density of the present Universe is comprised of non-baryonic cold dark matter. Cold dark matter (CDM) does not interact under electromagnetism and the strong force, and moves non-relativistically, thus acting like cold, pressureless dust in the present Universe. Despite these characteristics, its particle nature is still unknown and no candidate can be found within the Standard Model of particle physics (SM). So far, diverse extensions of the SM have predicted candidate particles for CDM, among which the most popular ones at present are in the form of weakly interacting massive particles (WIMPs) (see Refs. [2, 3, 4]). WIMPs are collisionless and massive ($>$ GeV).

The standard collisionless CDM, in a universe perturbed by Gaussian-random-noise primordial density fluctuations with a nearly scale-independent primordial power spectrum,

[1]This chapter is based on our paper published in *Phys. Rev. D*, Li, Rindler-Daller, Shapiro 2014 [1] ("Paper I"). Bohua Li is the lead author of this publication, who was responsible for the formulation of the scientific problem from basic equations and most of the analytical and numerical calculations both required to produce the results (including all the figures) of this paper.

provides a well-accepted scenario for cosmic structure formation: the hierarchical clustering of dark matter fluctuations and the infall of baryons into CDM potential wells after recombination, to form galaxies. Despite the fact that this story line is in good agreement with many observational constraints, including CMB anisotropy [5, 6, 7], large-scale structure [8, 9] and the general properties of dark-matter-dominated halos [10, 11, 12], some crucial issues on small scales are subject to controversy (see Ref. [13] for a recent, brief review). First, hierarchical clustering in the standard CDM model overpredicts the number of substructures in a halo the size of the Local Group by an order of magnitude as compared with the number of satellite galaxies observed in the Local Group, a discrepancy referred to as the "missing satellite problem" (see Refs. [14, 15, 16, 17]). Second, the density profiles of collisionless CDM halos in N-body simulations show a universal profile with a central cusp ($\sim r^{-1}$ in the NFW profile [18]), while observations of low-surface brightness galaxies and dwarf galaxies mostly favor a flat central slope. This has been known as the "cuspy core problem" (see Refs. [19, 20, 21, 22]). Furthermore, current dark matter detection experiments, both direct and indirect ones, have not yet discovered any compelling signals of WIMPs [23]. As a matter of fact, while WIMPs are mostly expected to be the lightest supersymmetric particle in the Minimal Supersymmetric Standard Model (MSSM), e.g., neutralinos [24], recent data from the Large Hadron Collider has found no evidence of a deviation from the SM on GeV scales, significantly restricting the allowed region of MSSM parameters [25, 26]. All these facts taken together, it is evident that the microscopic nature of dark matter is sufficiently unsettled as to justify the consideration of alternative candidates for the CDM paradigm, especially in the hope of resolving the above difficulties.

1.1.2 Bose-Einstein-condensed ultra-light particles as dark matter candidate

We assume that the dark matter particles are described by a spin-0 scalar field ('scalar field dark matter', for short; henceforth, SFDM) with a possible self-interaction. In fact, one type of bosonic particle suggested as a major candidate for dark matter is the QCD axion. It is the pseudo-Nambu-Goldstone boson in the Peccei-Quinn mechanism, proposed as a dynamical solution to the strong CP-problem in QCD. For the axion to be CDM, it has to be very light, $m \sim 10^{-5}$ eV$/c^2$ [27, 28].

In addition to the QCD axion, several fundamental scalar fields have been predicted by a variety of unification theories, e.g., string theories and other multi-dimensional theories [29, 30, 31, 32]. The bosonic particles envisaged are typically ultralight, with masses down to the order of 10^{-33} eV$/c^2$. This suggests an ultrahigh phase-space density, leading to the possibility of formation of a Bose-Einstein condensate (BEC), i.e., a macroscopic occupancy of the many-body ground state. In principle, for a fixed number of (locally) thermalized identical bosons, a BEC will form if $n\lambda_{\rm deB}^3 \gg 1$, where n is the number density and $\lambda_{\rm deB}$ is the de Broglie wavelength. This is equivalent to there being a critical temperature T_c, below which a BEC can form.

For a non-relativistic, ideal (i.e. non-interacting) boson gas, the well-known result for T_c is

$$T_c = \frac{2\pi\hbar^2}{mk_B}\left(\frac{n}{\zeta(3/2)}\right)^{2/3}, \tag{1.1}$$

which was used, for example, by Refs. [33, 34]. Equation (1.1) is not an adequate description of the case considered here, however. For the ultralight particles with which we are concerned, $k_B T_c/mc^2 \gg 1$, so a fully relativistic treatment is required.

We are interested in a complex scalar field, for which the presence of dark matter results from the asymmetry associated with the difference between the number density of bosons and that of their anti-particles, a conserved *charge* density in the comoving frame (see also Appendix A.2 for more discussion about the charge). A fully relativistic treatment of Bose-Einstein ('BE') condensation was given by Refs. [35] and [36], including the relationship between BE condensation and symmetry breaking of a scalar field. Those authors showed that, for an ultra-relativistic ideal *charged* boson gas, described by a *complex* scalar field,

$$T_c = \frac{(\hbar^3 c)^{1/2}}{k_B} \left(\frac{3q}{m} \right)^{1/2}, \tag{1.2}$$

where q is the charge per unit *proper* volume. This does not, however, take self-interaction into account. Reference [36] showed that, in the case of an adiabatically expanding boson gas, relevant to cosmology, if the scalar field has a generic quartic self-interaction, then the bosons must either be condensed at all temperatures (i.e. at all times) or else never form a BEC. In this case, the charge per unit *comoving* volume, Q ($Q = qa^3$), and entropy per unit comoving volume, S, are both conserved. According to equation (4.7) of that paper, a (local) BEC will exist from the beginning and remain at all times, if

$$\frac{Q}{S} \gg \frac{5}{4\pi^2 k_B} \left(\frac{\hat{\lambda}}{4} \right)^{1/2}, \tag{1.3}$$

where $\hat{\lambda}$ is the *dimensionless* coupling strength of the quartic self-interaction, in natural units. Our SFDM has essentially zero entropy per unit comoving volume. Also, for the small boson masses that we will be considering, the conserved charge density in the comoving frame, Q, is extremely high, given the observed present-day dark matter energy density $\bar{\rho}_{\rm dm}(t_0)$, for $Q \approx \bar{\rho}_{\rm dm}(t_0)/(mc^2)$. Therefore, we are always in the regime described by inequality (1.3),

and thus the bosons are fully condensed from the time they are born, i.e., almost all of the bosons occupy the lowest available energy state.

Hence, the cosmological Bose-Einstein-condensed SFDM can be described by a single (coherent) classical scalar field, of which the value at each point in space equals to that of the local order parameter [37]. Even though the condensation requires Bose-Einstein statistics in the first place, i.e., local thermalization (see Refs. [38, 39]), we argue that thermal decoupling within the bosonic dark matter can occur when the expansion rate exceeds its thermalization rate, without disturbing the condensate. Most of the bosons will stay in the ground state (BEC), and the classical field (SFDM) remains a good description, analogous to the fact that CMB photons after decoupling still follow a black-body distribution. In summary, we consider the Bose-Einstein condensate as an initial condition for our model, such that we can use and trust the effective field description throughout the evolution of the universe up to very early times.

A scalar field description of BEC dark matter has been studied by several authors before; see, for instance, Refs. [40, 41, 42, 43, 33, 44, 45, 46]. With regard to the aforementioned initial condition, one may also envisage a scenario in which the coherent scalar field is created gravitationally at the end of inflation, as has been considered, e.g., by Refs. [47, 48, 49]. On the other hand, it might also be that SFDM was just another scalar field, in place along with the inflaton before and during inflation [50, 51], emanating from yet earlier initial conditions. Speculations of that kind are beyond the scope of this paper. However, we find some interesting early-time features which will deserve more discussion in due course.

A prime motivation for studying SFDM has been its ability to suppress small-scale clustering and hence potentially resolve the dark matter problems mentioned above. For

non-self-interacting particles, $\lambda_{\rm deB} = h/(mv)$ sets a natural lower limit to the scale on which equilibrium halos can form, where v corresponds to the virial velocity of the galactic halos. While this paper shall deal only with the consequences of SFDM for the homogeneous background universe, this argument would suggest that there is a lower limit to the particle mass for SFDM of $m \gtrsim 10^{-22}$ eV$/c^2$, since then $\lambda_{\rm deB} \lesssim 1$ kpc [45, 52], the core size of the dark matter halo of a typical dwarf spheroidal galaxy in the present Universe [53]. If self-interaction of SFDM is included, the associated characteristic gravitational equilibrium scale $l_{\rm SI}$ is proportional to $\sqrt{\lambda/(mc^2)^2}$, where λ is the *dimensional* coupling strength of the quartic self-interaction (related to $\hat{\lambda}$ by $\lambda \equiv \hat{\lambda}\frac{\hbar^3}{m^2c}$), i.e., $l_{\rm SI} \simeq 1$ kpc if $\lambda/(mc^2)^2 \simeq 2\times10^{-18}$ eV^{-1} cm^3, and for this ratio of $\lambda/(mc^2)^2$, $\lambda \simeq 2\times10^{-62}$ eV cm^3 when $m \simeq 10^{-22}$ eV (see Refs. [45], and references therein). Therefore, SFDM provides $\lambda_{\rm deB}$ and $l_{\rm SI}$ as two mechanisms to suppress small-scale structures. When $l_{\rm SI} \gg \lambda_{\rm deB}$, only $l_{\rm SI}$ is responsible for affecting structure formation. This is the self-interaction-dominated limit, also known as the Thomas-Fermi regime; we called it TYPE II BEC-CDM in Ref. [45]. We will also address the limit in which there is *no* self-interaction (i.e. $\lambda \equiv 0$, also known as fuzzy dark matter (FDM) in Refs. [43, 54]; we called it TYPE I BEC-CDM in Ref. [45]).

This paper is organized as follows: in Section 1.2, we present the fundamental equations underlying the description of SFDM with a quartic, positive self-interaction. In Section 1.3, we solve for the homogenous background evolution of a universe with the same cosmic inventory as ΛCDM, but with CDM replaced by SFDM, over cosmic time. We identify three distinctive phases in the evolution of SFDM: non-relativistic, dust-like behavior at late times, which is indicative of the usefulness of SFDM as cold dark matter, a radiationlike phase at intermediate times, and an even earlier phase when SFDM behaves as a "stiff" relativistic

fluid. We note that SFDM is relativistic in both the radiationlike phase and the stiff phase (in this work, the word "relativistic" does not only refer to radiation, but generally refers to any type of matter for which the ratio of pressure p to energy density ρ is in the physically allowed range $1/3 \leq p/\rho \leq 1$). While the former two phases and the corresponding constraint from the time of matter-radiation equality at $z_{\rm eq} \sim 3000$ have been identified and appreciated previously (e.g. in Refs. [42, 49]), the latter one has only been sporadically encountered, and often as a result of special assumptions; see, e.g. Refs. [55, 51, 56]. However, we find that the stiff phase is generic for complex SFDM, no matter which values of SFDM parameter one adopts. We will comment more on this later. In Section 1.4, we present the most important results of this work, namely the constraints on the SFDM model parameters, boson mass m, and *positive* boson self-interaction coupling strength λ (or equivalently $\lambda/(mc^2)^2$, in which the final results will actually be presented), which follow from the constraints on the homogeneous background evolution by current cosmological observations. These include the aforementioned redshift of matter-radiation equality $z_{\rm eq}$ and the effective number of neutrino species $N_{\rm eff}$ at the time of big bang nucleosynthesis (BBN). They constrain the timing and longevity of the stiff and radiationlike phases of SFDM, and thereby set severe restrictions on the allowed parameter space. Finally, Section 1.5 contains detailed discussions on the many implications of our results, while Section 1.6 presents a brief summary. Appendices A.1-A.3 contains some more technical aspects which have been deferred from the main text, but help to make the presentation more self-contained.

In deriving those constraints on SFDM in concordance with current cosmological observations, we obtain three main results: First, we are able to restrict the allowed parameter space of SFDM *severely*, despite the fact that we limit our consideration to the homogeneous

background universe. Second, there, nevertheless, remains a semi-infinite stripe in parameter space which is in accordance with observations, including parameter sets which are able to resolve the small-scale problems of CDM. Third, the currently favored value of $N_{\rm eff}$ during BBN, which exceeds the standard value of 3.046 for a universe containing just three neutrino species and no extra relativistic species, excludes the possibility that the dark matter is SFDM with *vanishing* self-interaction, i.e., fuzzy dark matter, at $> 68\%$ confidence. On the contrary, SFDM with self-interaction provides a natural explanation of why $N_{\rm eff}$ during BBN [57] is higher than that inferred from the Cosmic Microwave Background [7].

1.2 Basic equations

We will assume in this paper that dark matter is described by a complex field. There are several motivations for considering a complex, rather than a real field, namely the U(1) symmetry corresponding to the dark matter particle number (charge) conservation (see Appendix A.2 and Ref. [58]), and the richer dynamics of halos, e.g. formation of vortices (see Refs. [45, 52]).

1.2.1 Equation of motion for SFDM

The ground state of a bosonic system can be described by a classic scalar field theory. We choose the following generic Lagrangian density of the complex scalar field

$$\mathscr{L} = \frac{\hbar^2}{2m} g^{\mu\nu} \partial_\mu \psi^* \partial_\nu \psi - V(\psi). \tag{1.4}$$

The metric signature we adopt here is $(+,-,-,-)$. The potential in the Lagrangian above contains a quadratic term accounting for the rest-mass plus a quartic term accounting for

the self-interaction

$$V(\psi) = \frac{1}{2}mc^2|\psi|^2 + \frac{\lambda}{2}|\psi|^4. \tag{1.5}$$

This model has been adopted in other works, as well; see, e.g., Refs. [42], [59], [60]. We choose physical units throughout, in contrast to the convention usually used in high-energy particle physics. The main reason is that this is the first paper in a series of works on the cosmological behavior of SFDM, which will include the linear and nonlinear growth of fluctuations. There, we are concerned with non-relativistic ($c \to \infty$) and classical limits ($\hbar \to 0$), where natural units become disadvantageous. In order for $\mathscr{L}$ to have units of energy density, the field has units of $[\psi] = \mathrm{cm}^{-3/2}$ and the unit for the coupling constant is $[\lambda] = \mathrm{eV\ cm}^3$. A value of $\lambda = 2 \times 10^{-62}$ eV cm^3 would correspond to $\hat{\lambda} = 2.6 \times 10^{-86}$. For the purpose of comparison, we take a look at the dimensionless self-interaction strength of QCD axions. According to equation (2) and (3) in Ref. [38], $\hat{\lambda}_{\mathrm{axion}} \sim 10^{-53}$, also tiny, for the axion decay constant $f \simeq 10^{12}$ GeV.

The quartic term in the above potential models the two-particle self-interaction. It is a good approximation to ignore higher order interactions when the bosonic gas is dilute, i.e., when the particle self-interaction range is much smaller than the mean interparticle distance. Moreover, since particles in non-zero-momentum states can be neglected, it is sufficient to consider only two-body s-wave scatterings. This means the coupling coefficient λ is a constant and related to the s-wave scattering length a_s as $\lambda = 4\pi\hbar^2 a_s/m$, which is effectively the first Born approximation.

The equation of motion for the scalar field is the relativistic Klein-Gordon equation,

$$\frac{1}{\sqrt{-g}}\partial_\mu\left(g^{\mu\nu}\sqrt{-g}\partial_\nu\psi\right) + \frac{m^2c^2}{\hbar^2}\psi + \frac{2\lambda m}{\hbar^2}|\psi|^2\psi = 0, \tag{1.6}$$

or

$$g^{\mu\nu}\partial_\mu\partial_\nu\psi - g^{\mu\nu}\Gamma^\sigma{}_{\mu\nu}\partial_\sigma\psi + \frac{m^2c^2}{\hbar^2}\psi + \frac{2\lambda m}{\hbar^2}|\psi|^2\psi = 0, \tag{1.7}$$

where $g_{\mu\nu}$ is the metric tensor and $\Gamma^\sigma{}_{\mu\nu} = \frac{1}{2}g^{\sigma\rho}(\partial_\mu g_{\rho\nu} + \partial_\nu g_{\rho\mu} - \partial_\rho g_{\mu\nu})$ is the Christoffel symbol, calculated in Appendix A.1.1 for the perturbed Friedmann-Robertson-Walker (FRW) metric. Combining such a metric in the conformal Newtonian gauge with the Klein-Gordon equation (1.7) yields

$$\begin{aligned}\left(1 - 2\frac{\Psi}{c^2}\right)\frac{\partial_t^2\psi}{c^2} - \left(1 + 2\frac{\Phi}{c^2}\right)\frac{\nabla^2\psi}{a^2} + \frac{3\mathrm{d}a/\mathrm{d}t}{c^2 a}\partial_t\psi - \\ - \left(\partial_t\Psi + 3\partial_t\Phi + 6\frac{\mathrm{d}a/\mathrm{d}t}{a}\Psi\right)\frac{\partial_t\psi}{c^4} - \\ -\nabla(\Psi - \Phi)\cdot\frac{\nabla\psi}{c^2a^2} + \frac{m^2c^2}{\hbar^2}\psi + \frac{2\lambda m}{\hbar^2}|\psi|^2\psi = 0.\end{aligned} \tag{1.8}$$

Here, a denotes the scale factor of the expanding FRW universe, and Ψ and Φ are the perturbations to the otherwise homogeneous metric (see Appendix A.1, where we summarize some of the more technical, but otherwise known derivations).

1.2.2 Einstein field equations

The perturbed metric given by equation (A.2) is related to the total mass-energy density of the universe through the Einstein field equations. With the Ricci tensor calculated in Appendix A.1.3, let us consider the contribution from the time-time component,

$$R^0{}_0 - \frac{1}{2}R = \frac{8\pi G}{c^4}T^0{}_0. \tag{1.9}$$

In fact, the left-hand side is

$$\begin{aligned}R^0{}_0 - \frac{1}{2}R &= (1 - 2\Psi/c^2)R_{00} - R/2 \\ &= \frac{3(\mathrm{d}a/\mathrm{d}t)^2}{c^2a^2} + \frac{2\nabla^2\Phi}{c^2a^2} - \frac{6\mathrm{d}a/\mathrm{d}t}{c^4 a}\left(\partial_t\Phi + \frac{\mathrm{d}a/\mathrm{d}t}{a}\Psi\right).\end{aligned} \tag{1.10}$$

Thus, the time-time component (1.9) becomes

$$3\frac{(\mathrm{d}a/\mathrm{d}t)^2}{a^2}+2\frac{\nabla^2\Phi}{a^2}-6\frac{\mathrm{d}a/\mathrm{d}t}{c^2a}\left(\partial_t\Phi+\frac{\mathrm{d}a/\mathrm{d}t}{a}\Psi\right)=\frac{8\pi G}{c^2}T^0_{\ 0}. \tag{1.11}$$

We can evaluate the contribution of the scalar field to the energy-momentum tensor, using the Lagrangian density in equation (1.4) and equation (A.9), which yields

$$\begin{aligned}T_{\mu\nu,\ \mathrm{SFDM}}=&\frac{\hbar^2}{2m}(\partial_\mu\psi^*\partial_\nu\psi+\partial_\nu\psi^*\partial_\mu\psi)-\\&-g_{\mu\nu}\left(\frac{\hbar^2}{2m}g^{\rho\sigma}\partial_\rho\psi^*\partial_\sigma\psi-\frac{1}{2}mc^2|\psi|^2-\frac{\lambda}{2}|\psi|^4\right).\end{aligned} \tag{1.12}$$

Its time-time component is recognized as

$$\begin{aligned}T^0_{\ 0,\ \mathrm{SFDM}}=\mathscr{H}=&\frac{\hbar^2}{2mc^2}\left(1-2\frac{\Psi}{c^2}\right)|\partial_t\psi|^2+\\&+\frac{\hbar^2}{2ma^2}\left(1+2\frac{\Phi}{c^2}\right)|\nabla\psi|^2+\frac{1}{2}mc^2|\psi|^2+\frac{1}{2}\lambda|\psi|^4.\end{aligned} \tag{1.13}$$

where $\mathscr{H}$ is the Hamiltonian density of SFDM. Note that $\mathscr{H}$ is not invariant under coordinate transformations, because matter is coupled to the gravitational field, hence the energy of the bosons is not conserved.

1.3 Homogenous background universe

1.3.1 Mass-energy content of the FRW universe and the Friedmann equation

In this paper, we will consider a universe with the same cosmic inventory as the basic ΛCDM model except that CDM is replaced by SFDM (we will call it ΛSFDM model from now on). We will use the set of cosmological parameters from the recent Planck data release [7] (listed as basic in Table 1.1) to solve for the evolution of the homogeneous background universe below. From those we derive some other cosmological parameters needed for the calculation. Note again that here $\Omega_{\mathrm{dm}}h^2$ refers to the present-day SFDM energy density

instead of CDM. We will see later that SFDM indeed behaves as CDM at present. $\Omega_r h^2$ accounts for the ordinary radiation component, i.e., photons and the Standard Model neutrinos. For simplicity, the neutrinos are considered as *massless* so that the total matter density fraction today is $\Omega_m = \Omega_b + \Omega_{\rm dm}$, where Ω_b stands for the baryon density fraction at present. The density fraction of the cosmological constant is $\Omega_\Lambda = 1 - \Omega_m - \Omega_r$.

Basic		Derived	
h	0.673	$\Omega_m h^2$	0.14187
$\Omega_b h^2$	0.02207	$\Omega_r h^2$	4.184×10^{-5}
$\Omega_{\rm dm} h^2$	0.1198	$z_{\rm eq}$	3390
$T_{\rm CMB}/{\rm K}$	2.7255	Ω_Λ	0.687

Table 1.1: Cosmological parameters. The values in the left column ('Basic') are quoted from the Planck collaboration: central values of the 68% confidence intervals for the base ΛCDM model with Planck+WP+highL data, see Table 5 in Ref. [7]. We calculate those in the right column ('Derived').

The expansion of the homogeneous FRW universe is governed by the Friedmann equation, which is a special case of equation (1.11),

$$\begin{aligned} H^2(t) &\equiv \left(\frac{{\rm d}a/{\rm d}t}{a}\right)^2 \\ &= \frac{8\pi G}{3c^2}\left[\bar\rho_r(t) + \bar\rho_b(t) + \bar\rho_\Lambda(t) + \bar\rho_{\rm SFDM}(t)\right], \end{aligned} \tag{1.14}$$

where we have $\bar\rho_r(t) = \Omega_r \rho_{0,\rm crit}/a^4$ for radiation, $\bar\rho_b(t) = \Omega_b \rho_{0,\rm crit}/a^3$ for baryons, $\bar\rho_\Lambda(t) = \Omega_\Lambda \rho_{0,\rm crit}$ for the cosmological constant and the SFDM energy density $\bar\rho_{\rm SFDM}(t)$ defined in the next section. The critical energy density at the present epoch is

$$\rho_{0,\rm crit} = \frac{3H_0^2 c^2}{8\pi G}. \tag{1.15}$$

Here is a technical detail: during the electron-positron annihilation that occurs around 0.5 MeV, $\bar{\rho}_r$ does not simply evolve as a^{-4} since photons get heated. Hence, we need to calculate the cosmic thermal history exactly, i.e., the photon temperature T as a function of a during that period, to acquire the evolution of $\bar{\rho}_r$. This effect will be reflected on the solutions in Section 1.4.2 (see Chapter 3 in Ref. [27] for a standard treatment).

As for the SFDM, we will see in the next section that $\bar{\rho}_{\rm SFDM}$ evolves through three phases which can be characterized by different equations of state.

1.3.2 Evolution of scalar field dark matter

In the case of the unperturbed homogeneous universe where $\Psi = \Phi = 0$, the scalar field is only a function of time, i.e., its energy-momentum tensor is diagonal. Hence, SFDM can be treated as a perfect fluid characterized by energy density $\bar{\rho}$, pressure $\bar{p}$ and 4-velocity u^μ (for brevity, we omit the subscript SFDM in this section). The corresponding energy-momentum tensor is

$$T_{\mu\nu} = (\bar{\rho} + \bar{p})u_\mu u_\nu / c^2 - g_{\mu\nu}\bar{p}, \tag{1.16}$$

where $u^0 = c$ and $u^i = 0$ for the homogeneous background universe. In fact, the energy density and pressure can be derived from equations (1.12) and (1.16),

$$\bar{\rho} = T^0_{\ 0} = \frac{\hbar^2}{2mc^2}|\partial_t\psi|^2 + \frac{1}{2}mc^2|\psi|^2 + \frac{1}{2}\lambda|\psi|^4, \tag{1.17}$$

$$\bar{p} = -T^i_{\ i} = \frac{\hbar^2}{2mc^2}|\partial_t\psi|^2 - \frac{1}{2}mc^2|\psi|^2 - \frac{1}{2}\lambda|\psi|^4. \tag{1.18}$$

Without perturbation terms in equation (1.8), the equation of motion for homogeneous SFDM is then

$$\frac{\hbar^2}{2mc^2}\partial_t^2\psi + \frac{\hbar^2}{2mc^2}\frac{3{\rm d}a/{\rm d}t}{a}\partial_t\psi + \frac{1}{2}mc^2\psi + \lambda|\psi|^2\psi = 0, \tag{1.19}$$

It can be transformed into an equivalent form, namely the energy conservation equation, given the expressions for $\bar{\rho}$ and $\bar{p}$ above,

$$\frac{\partial \bar{\rho}}{\partial t} + \frac{3\mathrm{d}a/\mathrm{d}t}{a}(\bar{\rho} + \bar{p}) = 0. \tag{1.20}$$

Note that this is also one of the conservation laws of the energy-momentum tensor $T^{0\nu}{}_{;\nu} = 0$, which is not surprising since the energy-momentum tensor is the Noether current of the spacetime translational symmetry and its conservation laws hold when the field follows the equation of motion (1.19).

If there were an *explicit* equation of state (EOS), relating $\bar{p}$ to $\bar{\rho}$, we could solve for the evolution of the entire background universe directly by combining it with equation (1.20) and the Friedmann equation (1.14). As we show below, this is only possible in certain limits of $\bar{w} \equiv \bar{p}/\bar{\rho}$, but the SFDM will pass through these limits as it evolves. Hence, it will be instructive to identify these phases of its evolution first, before we solve the general evolution equation in detail.

One of the basic behaviors of a scalar field is oscillation over time [61], characterized by its changes in phase θ. The oscillation angular frequency is defined as $\omega = \partial_t \theta$, the same as in Appendix A.2. We will see that the scalar field behaves differently whether ω predominates over the expansion rate H or the contrary (oscillation vs. roll).

1.3.2.1 Scalar field oscillation faster than Hubble expansion ($\omega/H \gg 1$)

In this regime, the oscillation angular frequency can be derived as (see Appendix A.2)

$$\omega = \frac{mc^2}{\hbar}\sqrt{1 + \frac{2\lambda}{mc^2}|\psi|^2}. \tag{1.21}$$

If ω is much larger than the Hubble expansion rate H, the exact cosmological time evolution of the scalar field will be hard to solve numerically, given that the necessary time step is essentially too tiny ($\propto 1/\omega$). Instead, we follow the evolution of the time-average values of $\bar{\rho}$ and $\bar{p}$ over several oscillation cycles. Multiplying the field equation (1.19) by ψ^* and then averaging over a time interval that is much longer than the field oscillation period, but much shorter than the Hubble time, results in (see Refs. [61, 59], and Appendix A.2 for detailed derivation)

$$\frac{\hbar^2}{2mc^2}\langle|\partial_t\psi|^2\rangle = \frac{1}{2}mc^2\langle|\psi|^2\rangle + \lambda\langle|\psi|^4\rangle. \tag{1.22}$$

Combining this relation with the expressions for energy density and pressure yields,

$$\begin{aligned}\langle\bar{\rho}\rangle &= mc^2\langle|\psi|^2\rangle + \frac{3}{2}\lambda\langle|\psi|^4\rangle \\ &\approx mc^2\langle|\psi|^2\rangle + \frac{3}{2}\lambda\langle|\psi|^2\rangle^2, \qquad (1.23)\\ \langle\bar{p}\rangle &= \frac{1}{2}\lambda\langle|\psi|^4\rangle \approx \frac{1}{2}\lambda\langle|\psi|^2\rangle^2. \qquad (1.24)\end{aligned}$$

The equation of state is then

$$\langle\bar{p}\rangle = \frac{m^2c^4}{18\lambda}\left(\sqrt{1+\frac{6\lambda\langle\bar{\rho}\rangle}{m^2c^4}}-1\right)^2, \tag{1.25}$$

or equivalently,

$$\langle\bar{w}\rangle \equiv \frac{\langle\bar{p}\rangle}{\langle\bar{\rho}\rangle} = \frac{1}{3}\left[\frac{1}{1+\frac{2mc^2}{3\lambda\langle|\psi|^2\rangle}}\right], \tag{1.26}$$

as found also in Ref. [62] for a real scalar field. This equation of state (1.25) was also derived in Ref. [63], in the context of boson stars. This approach will be called the *fast oscillation approximation* in this paper.

(1) CDM-like phase: non-relativistic ($\langle\bar{w}\rangle = 0$)

As the universe expands, the dark matter energy density will continuously decrease to the point when the rest-mass energy density dominates the total SFDM energy density, i.e., $\frac{3}{2}\lambda\langle|\psi|^2\rangle^2 \ll mc^2\langle|\psi|^2\rangle$. In this limit, equation (1.25) reduces to

$$\langle\bar{p}\rangle \approx \frac{\lambda}{2m^2c^4}\langle\bar{\rho}\rangle^2 \approx 0, \tag{1.27}$$

thus SFDM behaves like non-relativistic dust. Its self-interaction is weak, so that on large scales SFDM is virtually collisionless. Therefore, it evolves like CDM, following the familiar relation,

$$\langle\bar{\rho}\rangle \propto a^{-3}. \tag{1.28}$$

Then, the field amplitude decays as $|\psi| \propto a^{-3/2}$ and the scale factor goes as $a \sim t^{2/3}$.

(2) Radiation-like phase: relativistic ($\langle\bar{w}\rangle = 1/3$)

At some point early enough, the SFDM will be so dense that the quartic term in the energy density (1.23), the self-interaction energy, dominates, i.e., $\frac{3}{2}\lambda\langle|\psi|^2\rangle^2 \gg mc^2\langle|\psi|^2\rangle$. In this limit, equation (1.25) reduces to

$$\langle\bar{p}\rangle \approx \frac{1}{3}\langle\bar{\rho}\rangle \approx \frac{1}{2}\lambda\langle|\psi|^2\rangle^2, \tag{1.29}$$

thus the SFDM behaves like radiation. The time evolution is accordingly

$$\langle\bar{\rho}\rangle \propto a^{-4}, \tag{1.30}$$

while the field amplitude decays as $|\psi| \propto a^{-2}$ with the scale factor $a \sim t^{1/2}$.

It is important to note that SFDM without self-interaction, i.e., when $\lambda = 0$, does *not* undergo this radiationlike phase. This has severe implications for such models, as will be discussed in Section 1.5.4.

1.3.2.2 Scalar field oscillation slower than Hubble expansion ($\omega/H \ll 1$)

The Hubble parameter increases as one goes back in time, eventually exceeding the oscillation frequency, and the fast oscillation approximation will break down. There is no simple explicit equation of state then. In this case, one has to solve the coupled equations (1.14), (1.17), (1.18) and (1.20) exactly, with which we will be concerned in the next section. Nonetheless, one can still find a heuristic qualitative description, as follows.

(1) Stiff phase: relativistic limit ($\bar{w} = 1$)

At sufficiently early times, the expansion rate is much greater than the oscillation frequency, $\omega/H \ll 1$. The energy density and pressure are both dominated by the first, kinetic term of (1.17) and (1.18), for $(|\partial_t\psi|/|\psi|)^2 \propto H^2$. Therefore,

$$\bar{p} \approx \bar{\rho} \approx \frac{\hbar^2}{2mc^2}|\partial_t\psi|^2. \tag{1.31}$$

This stiff EOS implies that the sound speed almost reaches the speed of light, the maximal value possible, which is an analogue to the incompressible fluid in Newtonian gas dynamics, where the sound speed is infinity. In this case,

$$\bar{\rho} \propto a^{-6}, \tag{1.32}$$

and it can be shown that $\partial_t\psi \propto a^{-3}$, and hence $\psi \propto \log a$, where $a \sim t^{1/3}$. The physical picture of the stiff phase is that, at such an early epoch, the Hubble time is much smaller than the oscillation period so that the complex scalar field cannot even complete one cycle of spin, instead, it rolls down the potential well. The field value now evolves as $|\log a|$, which increases moderately compared with power laws as $a \to 0$, suggesting that no undesirable blow-up occurs in this very early universe.

1.3.3 Evolution of the FRW homogeneous background universe with SFDM

Now we are ready to calculate the full evolution history of the homogeneous background universe, in which SFDM follows different equations of state (either explicit or implicit) at different cosmic epochs, while the other components can be treated straightforwardly as explained in Section 1.3.1.

1.3.3.1 Numerical Method

We have seen in Section 1.3.2.1 that SFDM oscillates rapidly in comparison with the Hubble expansion rate at later times in the cosmic history. When $\omega/H \gg 1$, the fast oscillation approximation can be applied, and we are able to use the equation of state (1.25) for the time-average SFDM energy density and pressure. From the energy conservation equation (1.20), we see that as long as the oscillation is much faster than the rate at which the scale factor changes, the time evolution of the SFDM energy density should be quite smooth, with minute oscillation amplitude, since the oscillations in $\bar{\rho}_{\rm SFDM}$ and $\bar{p}_{\rm SFDM}$ cancel out through integration. Therefore, $\bar{\rho}_{\rm SFDM}$ should almost equal its time-average value $\langle\bar{\rho}_{\rm SFDM}\rangle$, which is even true in the real scalar field case [44]. Furthermore, we can convert the energy conservation equation (1.20) as follows,

$$\frac{\mathrm{d}}{\mathrm{d}a}\langle\bar{\rho}_{\rm SFDM}\rangle + \frac{3(\langle\bar{\rho}_{\rm SFDM}\rangle + \langle\bar{p}_{\rm SFDM}\rangle)}{a} = 0, \tag{1.33}$$

so that it can be coupled to the equation of state (1.25) to solve for the evolution of $\langle\bar{\rho}_{\rm SFDM}\rangle$ and $\langle\bar{p}_{\rm SFDM}\rangle$ as a function of scale factor a, by integrating from the present-day backwards to the point where $\omega/H = 200$ (still well into the fast oscillation regime). We then solve the Friedmann equation (1.14) with $\bar{\rho}_{\rm SFDM}$ replaced by $\langle\bar{\rho}_{\rm SFDM}\rangle$. The resulting time-average

Hubble expansion rate $\langle H^2\rangle$ should be almost the same as its exact value, since $\bar{\rho}_{\rm SFDM} \simeq \langle\bar{\rho}_{\rm SFDM}\rangle$. The present-day values are inferred from Table 1.1. We will refer to the solution obtained above as the 'late-time solution', during the period in which time-averages are excellent approximations to the exact values.

At earlier times up to the big bang, the system has to be solved exactly, since ω/H decreases and the fast oscillation approximation becomes invalid. Combining equations (1.17) and (1.18), the equation of state is implicitly given by the following coupled ordinary differential equations,

$$\partial_t(\bar{\rho}_{\rm SFDM} - \bar{p}_{\rm SFDM}) = B\sqrt{1+\frac{4\lambda}{m^2c^4}(\bar{\rho}_{\rm SFDM} - \bar{p}_{\rm SFDM})}, \tag{1.34}$$

$$\begin{aligned}&\frac{\hbar^2}{2m^2c^4}\left(\partial_t B + \frac{3{\rm d}a/{\rm d}t}{a}B\right)\\ =\;& 2\bar{p}_{\rm SFDM} - \frac{m^2c^4}{4\lambda}\times\left(\sqrt{1+\frac{4\lambda}{m^2c^4}(\bar{\rho}_{\rm SFDM} - \bar{p}_{\rm SFDM})}-1\right)^2,\end{aligned} \tag{1.35}$$

where the auxiliary variable B is defined as $B \equiv mc^2\partial_t|\psi|^2$. We will refer to it as the 'early-time solution'. One can verify that, if the left-hand side of equation (2.33) is zero, i.e., Hubble expansion is negligible, the equation of state reduces to the one in (1.25) in the limit $\omega/H \gg 1$. We solve for the time-dependence of $\bar{\rho}_{\rm SFDM}$, $\bar{p}_{\rm SFDM}$ and scale factor a by solving the combination of the Friedmann equation (1.14), the energy conservation equation (1.20) along with (1.34) and (2.33), using a fourth-order Runge-Kutta solver. The integration starts from the point where we cease to apply the fast oscillation approximation at $\omega/H = 200$, as mentioned above, back to the big bang, in a way that it matches to the late-time solution. The matching is not trivial, since there are 3 variables in the late-time solution ($\langle\bar{\rho}_{\rm SFDM}\rangle$, $\langle\bar{p}_{\rm SFDM}\rangle$ and a) but 4 variables in the early-time solution ($\bar{\rho}_{\rm SFDM}$, $\bar{p}_{\rm SFDM}$, a and B). For details on the matching condition, see Appendix A.3.

1.3.3.2 Numerical solution: evolution of the fiducial model

Anticipating our later results with regard to the cosmologically allowed range of SFDM particle parameters, we will henceforth adopt the following fiducial values for particle mass and self-interaction coupling strength:

$$(m, \lambda)_{\text{fiducial}} = (3 \times 10^{-21}\ \text{eV/c}^2, 1.8 \times 10^{-59}\ \text{eV cm}^3),$$
$$\lambda/(mc^2)^2 = 2 \times 10^{-18}\ \text{eV}^{-1}\ \text{cm}^3. \tag{1.36}$$

In this work, it is more convenient to work with the ratio $\lambda/(mc^2)^2$ rather than λ, as will be seen in the rest of the paper. The evolution for this fiducial SFDM model is shown in Figures 1.1 and 1.2. The smooth transition between the two parts of the solution (early-time and late-time) follows from the correctness of the matching conditions (see Appendix A.3). The evolution of the SFDM energy density $\bar{\rho}_{\text{SFDM}}$ in Figure 1.1 (left-hand plot) shows not only the transition of SFDM from CDM-like to radiationlike around $a \sim 10^{-4}$, but that at an even earlier time $a \lesssim 10^{-10}$, SFDM follows, indeed, a stiff equation of state. The evolution of the equation of state is plotted in Figure 1.1 (right-hand plot), where we can also clearly see the transition from the stiff phase, to the radiationlike phase, to the CDM-like phase.

The evolution of the energy content in our fiducial model can be found in Figure 1.3. The energy density of SFDM $\bar{\rho}_{\text{SFDM}} \propto a^{-6}$ surpasses that of radiation $\bar{\rho}_r \propto a^{-4}$ in the stiff phase of SFDM. Hence, the expansion rate in the stiff phase is higher, $H \propto a^{-3}$, than that in the radiation-dominated era, $H \propto a^{-2}$. This is a "scalar-field-dark-matter-dominated" era, before the radiation-dominated era. Here, the transition time from the stiff phase to the radiationlike phase depends on both $\lambda/(mc^2)^2$ *and* m. This can be understood by realizing that, the transition happens when the first term (kinetic term, which depends on m) and the third term (self-interaction term, which depends on λ) on the rhs of (1.17) and (1.18) become of equal order. Another way to see this is that, the equations which we solve when

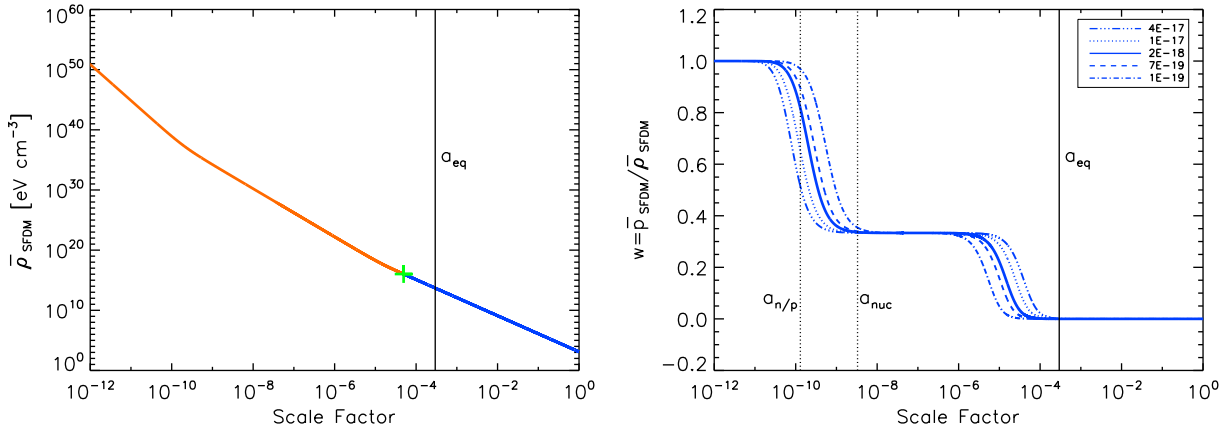

Figure 1.1: *Left-hand plot:* Evolution of the SFDM energy density $\bar{\rho}_{\rm SFDM}$ vs. scale factor a. The SFDM parameters are $m = 3 \times 10^{-21}$ eV$/c^2$ and $\lambda/(mc^2)^2 = 2 \times 10^{-18}$ eV^{-1} cm^3 (fiducial model). The vertical solid line depicts the epoch of matter-radiation equality $a_{\rm eq}$ from Table 1.1, while the cross indicates the point after which SFDM is well described as fully non-relativistic matter (CDM-like). *Right-hand plot:* Evolution of the equation of state $\bar{w} = \bar{p}_{\rm SFDM}/\bar{\rho}_{\rm SFDM}$. The solid curve corresponds to the fiducial model plotted in the left panel. The other curves represent models with the same mass m, but different ratios of $\lambda/(mc^2)^2$ in unit of eV^{-1} cm^3, as seen in the legend. The vertical dotted lines depict the epoch of neutron-proton freeze-out $a_{\rm n/p}$ and the epoch of light-element production $a_{\rm nuc}$, respectively (see Section 1.4.2). The larger the value of $\lambda/(mc^2)^2$, the longer lasts the radiationlike phase of SFDM: this provides constraints on this ratio from CMB observations of $a_{\rm eq}$ and $N_{\rm eff}$ during BBN, see Sections 1.4.1 and 1.4.2.

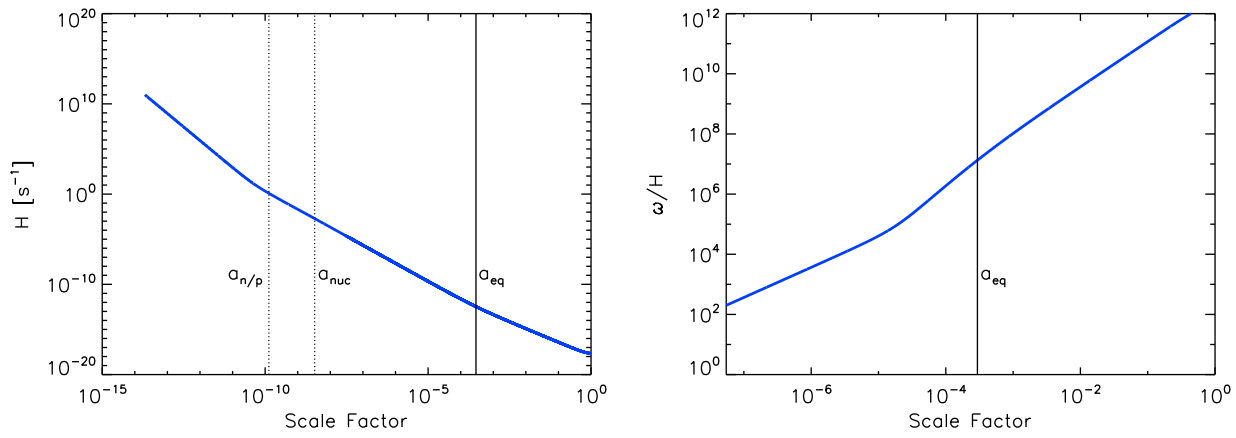

Figure 1.2: *Left-hand plot:* Hubble parameter $H(a)$ vs. scale factor a for our fiducial SFDM model with $m = 3 \times 10^{-21}$ eV$/c^2$ and $\lambda/(mc^2)^2 = 2 \times 10^{-18}$ eV^{-1} cm^3. *Right-hand plot:* Evolution of the ratio of the oscillation angular frequency and Hubble parameter, ω/H, for that same model. The vertical solid line depicts the epoch of matter-radiation equality $a_{\rm eq}$ from Table 1.1. The vertical dotted lines depict the beginning of the neutron-proton ratio freeze-out $a_{\rm n/p}$ and the epoch of light-element production $a_{\rm nuc}$, respectively (see Section 1.4.2).

scalar field oscillation is slower than the Hubble expansion rate involve both these two parameters (see equations (1.34) and (2.33)). After the stiff-to-radiation transition, the energy fraction of SFDM reaches a "plateau" as well as that of the regular radiation component, since both components have radiationlike equations of state. This already implies that the kinetic term diminishes to the point where it is comparable to the self-interaction term (see equation(1.22)), as the scalar field oscillation becomes faster than the Hubble expansion rate, which is verified below. Therefore, the height of the plateau, i.e., the energy fraction of SFDM in the radiationlike phase, is determined by $\lambda/(mc^2)^2$ alone, because the equations for the fast oscillation approximation only concern this ratio (see equation (1.25)). It should be noted that the plateau height would vanish if there is no self-interaction ($\lambda = 0$), see also Section 1.5.4.

The energy fraction of SFDM starts to rise from the plateau value after a second transition from the radiationlike phase to the CDM-like phase. The energy density of SFDM evolves as $\bar{\rho}_{\rm SFDM} \propto a^{-3}$ like standard CDM, and the expansion rate as $H \propto a^{-3/2}$ when SFDM dominates. The background evolution of the fiducial model is then the same as the basic ΛCDM model.

It is interesting to note that, in the ΛSFDM model, dark matter dominates over the other cosmological components *twice* during the cosmic history, first in the stiff-matter phase, where it is highly relativistic, and later, when it behaves as pressureless dust, as in the standard scenario of CDM. As we will see in the next section, there are indeed constraints to be derived from both epochs. Also, the radiation-dominated era of the universe basically coincides with the radiationlike phase (plateau) of SFDM, since both of the SFDM transitions occur rapidly.

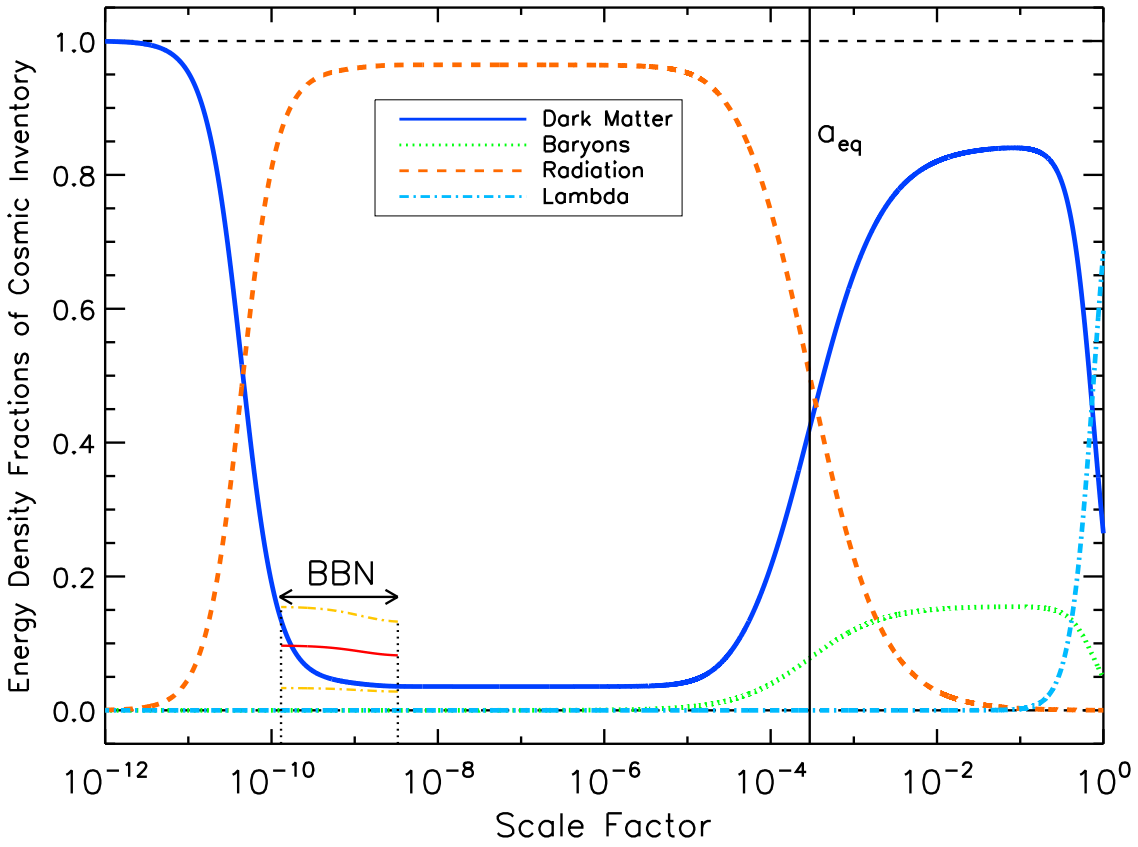

Figure 1.3: Evolution of the fractions Ω_i of the energy density of each cosmic component i with SFDM of mass $m = 3 \times 10^{-21}$ eV/c^2 and self-interaction $\lambda/(mc^2)^2 = 2 \times 10^{-18}$ eV^{-1} cm^3 (fiducial model) represented by the thick curves. Different components are depicted with different line styles, as labeled in the legend. The solid vertical line corresponds to $a_{\rm eq}$. On the lower left part of the figure, the thin curves represent the constraint from BBN. The solid one refers to a universe with a constant $N_{\rm eff}$ of the central value in (1.40) and the two dash-dotted ones refer to such universes with $N_{\rm eff}$ of the 1σ limits there. The dotted vertical lines indicate the beginning of the neutron-proton ratio freeze-out $a_{\rm n/p}$ and the epoch of light-element production $a_{\rm nuc}$, respectively.

We would like to verify that the fast oscillation approximation discussed in Section 1.3.2.1 is indeed applicable for the fiducial model, for large enough a, where we solve for the evolution of the time-averages of $\bar{\rho}_{\rm SFDM}$ and $\bar{p}_{\rm SFDM}$, instead of solving for their exact values. In other words, we would like to see that its condition $\omega/H \gg 1$ is fulfilled during that era, for our fiducial model. The plot of ω/H can be found in Figure 1.2 (right-hand plot). Apparently, $\omega/H > 200$ for all a therein, justifying the fast oscillation approximation at later times.

1.4 Constraints on particle parameters from CMB and BBN measurements

1.4.1 Constraint from $z_{\rm eq}$

As has been noted before ([42, 49, 51]) the transition of SFDM from the radiationlike phase to the CDM-like phase must happen early enough to be in agreement with the redshift of matter-radiation equality $z_{\rm eq}$ determined by the CMB temperature power spectrum, since its shape is subject to the early integrated Sachs-Wolfe (ISW) effect, which depends upon $z_{\rm eq}$ [64]. In other words, in order to preserve $z_{\rm eq}$, SFDM should be well into the CDM-like phase at $z_{\rm eq}$. Before we proceed, it should be marked that the requirement above actually prohibits any freedom in choosing one of the initial conditions $\Omega_{\rm dm}h^2$, the present-day SFDM density parameter, which must be the same as that in the six-parameter base ΛCDM model (see Table 1.1). In fact, one can derive from the definition of $z_{\rm eq}$ that

$$1 + z_{\rm eq} \equiv \frac{1}{a_{\rm eq}} = \frac{\Omega_b h^2 + \Omega_{\rm dm} h^2}{\Omega_r h^2}, \tag{1.37}$$

where $a_{\rm eq}$ is the scale factor at matter-radiation equality. This justifies our choice of $\Omega_{\rm dm}h^2$.

The requirement that SFDM be fully non-relativistic at $z_{\rm eq}$ sets a constraint on the SFDM particle parameters, which is illustrated in Figure 1.1. The redshift of matter-radiation equality $z_{\rm eq}$, according to Table 1.1, is marked as the vertical solid line in every plot. We define the cross in the left-hand plot to be the point at which $\langle \bar{w} \rangle \equiv \langle \bar{p} \rangle / \langle \bar{\rho} \rangle$ (neglecting the subscript SFDM here) is 0.001, a tiny deviation from zero, and consider SFDM after this point as fully non-relativistic. We can see that for the fiducial model, this point is indeed early enough compared with $z_{\rm eq}$. In fact, *only* the ratio $\lambda/(mc^2)^2$ is constrained by this requirement, as it alone determines the radiation-to-matter transition point of SFDM, resulting in

$$\frac{\lambda}{(mc^2)^2} \leq 4 \times 10^{-17}\ {\rm eV}^{-1}\ {\rm cm}^3. \tag{1.38}$$

This is the upper bound which would make the cross in the left-hand plot of Figure 1.1 lie on top of the vertical line indicating $z_{\rm eq}$, i.e., the marginal case where SFDM has just fully morphed into CDM at matter-radiation equality (see also the right-hand plot for the evolution of $\langle \bar{w} \rangle$ in the marginal case). Equation (1.38) implies that, even SFDM with large values of λ *and* m, as adopted in some literature, is able to fulfill this constraint (this is in the self-interaction-dominated limit, since large m indicates small $\lambda_{\rm deB}$).

The choice of the threshold 0.001 is artificial, though. If we relax it to 0.01, i.e., consider SFDM as fully non-relativistic when $\langle \bar{w} \rangle$ is less than 0.01, the corresponding constraint on $\lambda/(mc^2)^2$ would become $\lambda/(mc^2)^2 \leq 4.2 \times 10^{-16}\ {\rm eV}^{-1}\ {\rm cm}^3$, allowing a broader range of values. To determine this threshold, we need to calculate the CMB power spectrum for given SFDM particle parameters and see the range of them that preserves the early ISW effect. We plan this for future work.

1.4.2 Constraint from $N_{\rm eff}$ during big bang nucleosynthesis

The abundances of the big bang nucleosynthesis (BBN) products set a constraint on the Hubble expansion rate at that time, which depends on the total energy density of the relativistic species, parameterized by an effective number of relativistic degrees of freedom, also known as an effective number of neutrino species, $N_{\rm eff}$ (see Ref. [57] for a recent review). Thus, measurements of the primordial abundance of helium and deuterium can constrain the expansion rate or, equivalently, $N_{\rm eff}$, during BBN. In the ΛCDM model, where there are only three SM neutrino species, $N_{\rm eff,standard} = 3.046$ [65]. In contrast, in ΛSFDM model, if SFDM is relativistic then, it will contribute to $N_{\rm eff}$ as an extra relativistic component, and the constraints on $N_{\rm eff}$ consequently put control on the properties of SFDM, i.e., its particle parameters again.

The standard BBN scenario consists of two stages, the freeze-out of the neutron fractional abundance and the production of light elements combining free neutrons into nuclei, each affected by the expansion rate at its own epoch. The attempts to determine $N_{\rm eff}$ from BBN usually fit a cosmological model with constant extra number of neutrino species $\Delta N_{\rm eff} \equiv N_{\rm eff} - N_{\rm eff,standard}$, e.g., with a constant portion of sterile neutrinos, to the primordial abundances of light elements extrapolated from observations. However, in ΛSFDM, the $\Delta N_{\rm eff}$ caused by SFDM is changing over time as its equation of state varies during different eras. Therefore, we must study the *evolution* of $N_{\rm eff}$ throughout BBN, which is an extended period from the beginning of the neutron-proton ratio freeze-out around $T_{\rm n/p} = 1.293$ MeV (the difference between the neutron and the proton mass) to the epoch of nuclei production around $T_{\rm nuc} \approx 0.07$ MeV.

In a ΛSFDM model, we infer the $N_{\rm eff}$ during BBN, namely from $T_{\rm n/p}$ to $T_{\rm nuc}$, from the

energy density of relativistic SFDM $\bar{\rho}_{\rm SFDM}$, which is determined by the particle parameters. In fact, SFDM is completely relativistic then and is the only source for $\Delta N_{\rm eff}$,

$$\frac{\Delta N_{\rm eff}}{N_{\rm eff,standard}} = \frac{\bar{\rho}_{\rm SFDM}}{\bar{\rho}_\nu}, \tag{1.39}$$

where $\bar{\rho}_\nu$ is the total energy density of the SM neutrinos. We compare the $N_{\rm eff}$ obtained this way to the measured value (constant over time) and impose a conservative constraint that the $N_{\rm eff}$ during BBN be all the time within 1σ of the measured value,

$$N_{\rm eff} = 3.71^{+0.47}_{-0.45}, \tag{1.40}$$

which we adopt from Ref. [57]. We shall adopt this 68% confidence interval in constraining the parameters of SFDM in what follows. We note that while the standard ΛCDM model with $N_{\rm eff,standard} = 3.046$ is inconsistent with the 1σ constraint, it is, nevertheless, consistent within 95% confidence. Ideally, we need to fit our model not to such a constant $N_{\rm eff}$ value, but to the data of primordial abundances directly by deriving those for ΛSFDM with a BBN code, which is intended as our future work.

The result is plotted in Figure 1.4. The upper plots show the Hubble expansion rate of ΛSFDM universes with different particle parameters normalized to the expansion rate of the basic ΛCDM universe, which is an equivalent illustration of the evolution of $N_{\rm eff}$, as in the lower plots. The thin curves are benchmarks. The solid ones refer to a universe with a constant $N_{\rm eff}$ of the central value in equation (1.40) and the dash-dotted ones refer to such universes with $N_{\rm eff}$ of the 1σ limits there, respectively. Note that in the upper plots for the normalized expansion rate, these thin curves are not straight lines due to the electron-positron annihilation. After this event, the neutrinos contribute less to the total energy

density of the universe as their energy density fraction shrinks, because they are decoupled and do not get heated.

In each plot, the thick curves denote different models of ($\lambda/(mc^2)^2$, m), according to the legend. The solid ones represent the fiducial model again: it complies with the constraint mentioned above (1.40). It can be seen that these curves all reach the "plateau", i.e., the radiationlike phase, before the epoch of light-element production $a_{\rm nuc}$. The plateau height is purely determined by $\lambda/(mc^2)^2$, as explained in Section 1.3.3.2. In the left-hand plots, where we fix m, the higher the $\lambda/(mc^2)^2$, the higher the plateau. Meanwhile, earlier at $a_{\rm n/p}$ the transition from the stiff phase to the radiationlike phase may not have finished and the value of $N_{\rm eff}$ can be higher than its plateau, which is a function of both $\lambda/(mc^2)^2$ and m. In the right-hand plots, models with the same $\lambda/(mc^2)^2$, but different m, have the same plateau height, but diverge with a different rate as we go back in time: the lower the m, the later is the transition to the radiationlike phase. Therefore, the evolution of $N_{\rm eff}$ during BBN restricts both SFDM particle parameters, $\lambda/(mc^2)^2$ and m. This constraint is demonstrated in the next section and Figure 1.5.

Note that this constraint is also illustrated in Figure 1.3, where the definitions of the thin curves between $a_{\rm n/p}$ and $a_{\rm nuc}$, among which one is solid and two are dash-dotted, are the same as above, and the fraction of the SFDM energy density $\Omega_{\rm SFDM}$ is restricted by the two dash-dotted curves, which correspond to the 1σ limits of $N_{\rm eff}$ in equation (1.40). Again, these thin curves, which represent the energy fractions of extra radiation in models with constant $N_{\rm eff}$, slightly drop because of the electron-position annihilation. While $N_{\rm eff}$ characterizes the SFDM energy density (see equation (1.39)), the relation between $\Omega_{\rm SFDM}$ and $N_{\rm eff}$ has a simple analytical form *during the plateau*. The total energy density of a ΛSFDM universe

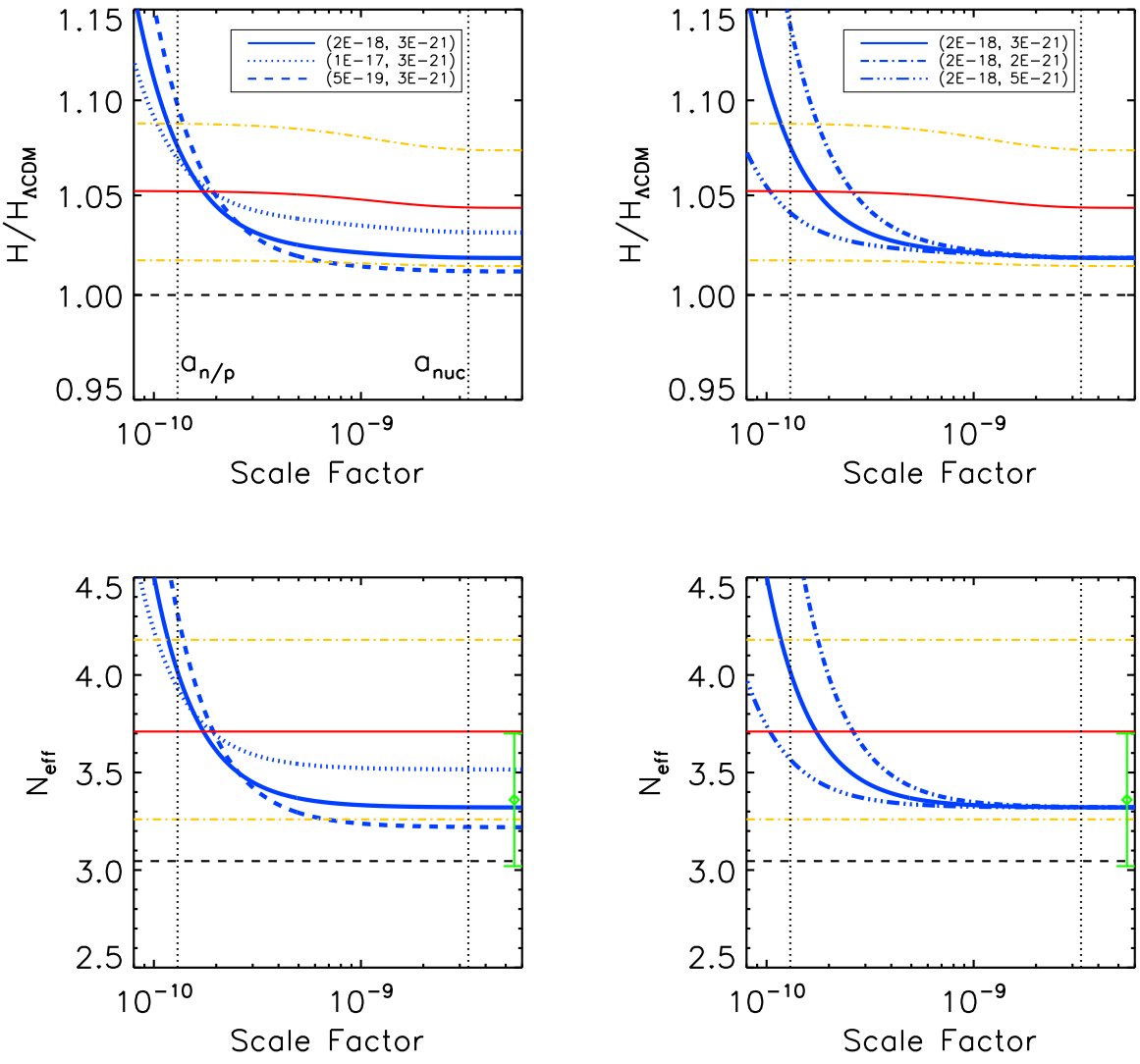

Figure 1.4: *Upper plots:* Evolution of the normalized Hubble expansion rate $H(a)/H_{\Lambda\mathrm{CDM}}(a)$ vs. scale factor a. *Lower plots:* Evolution of the effective number of neutrino species, N_{eff}, vs. scale factor a. The thick curves represent the evolution of ΛSFDM models with various particle parameters. In the left-hand plots, m is fixed. In the right-hand plots, $\lambda/(mc^2)^2$ is fixed. The solid ones again correspond to our fiducial model with SFDM parameters $m = 3\times10^{-21}$ eV/c^2 and $\lambda/(mc^2)^2 = 2\times10^{-18}$ eV cm^3, see legends for the corresponding values of $(\lambda/(mc^2)^2, m)$ of each thick curve, in units of (eV^{-1} cm^3, eV/c^2). Among the thin curves, the solid (dash-dotted) ones refer to universes with constant N_{eff} at the central value (68% confidence limits) of the measured N_{eff} (1.40). The error bar in the lower plots is from the result of CMB measurements, $N_{\mathrm{eff}} = 3.36\pm0.34$ [7].

during the radiation-dominated era is proportional to

$$\begin{aligned} & 2 + 2N_{\rm eff}({\rm plateau}) \cdot \frac{7}{8}\left(\frac{4}{11}\right)^{4/3} \\ = \ & \left(2 + 2N_{\rm eff,standard} \cdot \frac{7}{8}\left(\frac{4}{11}\right)^{4/3}\right) \times \frac{1}{1-\Omega_{\rm SFDM}({\rm plateau})}. \end{aligned} \tag{1.41}$$

Thus, if SFDM reaches the plateau before $a_{\rm nuc}$, the 68% confidence interval of $N_{\rm eff}$ (1.40) can be converted to that of $\Omega_{\rm SFDM}$ during the plateau (its plateau height), using the equation above,

$$0.028 \leq \Omega_{\rm SFDM}({\rm plateau}) \leq 0.132. \tag{1.42}$$

Consequently, we can use either (1.40) or (1.42) to constrain the SFDM parameter $\lambda/(mc^2)^2$, in terms of the plateau height, of those models in which SFDM has reached the radiationlike phase by the end of BBN. The result is

$$9.5 \times 10^{-19}\ {\rm eV}^{-1}\ {\rm cm}^3 \leq \lambda/({\rm mc}^2)^2 \leq 1.5 \times 10^{-16}\ {\rm eV}^{-1}\ {\rm cm}^3, \tag{1.43}$$

as will be seen in Figure 1.5. It should be also heeded that, in principle, SFDM does not have to reach the plateau by $a_{\rm nuc}$, and the result above (1.43) is not applicable for those models.

1.4.3 Result: allowed SFDM particle parameter space

Combining the results from the above two sources of constraints, we can confine the allowed region in the parameter space of SFDM, or ultralight bosonic particle, see Figure 1.5 for the parameter space plot. The constraint from $z_{\rm eq}$ is given by the solid vertical line: the region on its left side is allowed, as shown by equation (1.38). For the constraint from $N_{\rm eff}$ during BBN, we sample the parameter space to obtain the critical parameter

values which marginally fulfill the 1σ limits (1.40). The two shaded bands correspond to the constraints that $N_{\rm eff}$ be within 1σ at $a_{\rm n/p}$ and $a_{\rm nuc}$, as labeled respectively. For each band, the thick solid (dashed) boundary curve refers to the upper (lower) 1σ limit of $N_{\rm eff}$. The intersection of these two bands represents the range of parameters that is consistent with the $N_{\rm eff}$ constraint within 1σ throughout BBN. It is easily seen from the figure that all allowed choices of $(\lambda/(mc^2)^2,\, m)$ from the $N_{\rm eff}$ constraint indeed correspond to models in which SFDM has reached the radiationlike phase by the end of BBN, so that $\lambda/(mc^2)^2$ must be bounded within the asymptotic vertical lines (1.43) explained in the last section. This fact is completely due to the present-day measured $N_{\rm eff}$ value (1.40). Should the 68% confidence interval of $N_{\rm eff}$ be broaden, models in which SFDM had not reached the plateau by the end of BBN might also be allowed. Such models would not lie within the asymptotic vertical bounds of $\lambda/(mc^2)^2$ in the parameter space, as mentioned at the end of the last section.

The final allowed region is given by combining all the constraints, leaving the crosshatched area. The dotted vertical line, where the fiducial model sits, has the value $\lambda/(mc^2)^2 = 2 \times 10^{-18}$ eV^{-1} cm^3, which corresponds to models with parameters for an equilibrium halo of size about 1 kpc, see equation (1.44) in Section 1.5.1. We can see that it lies within the allowed region, for high enough particle mass m. The significance of this result will be discussed in Section 1.5.1.

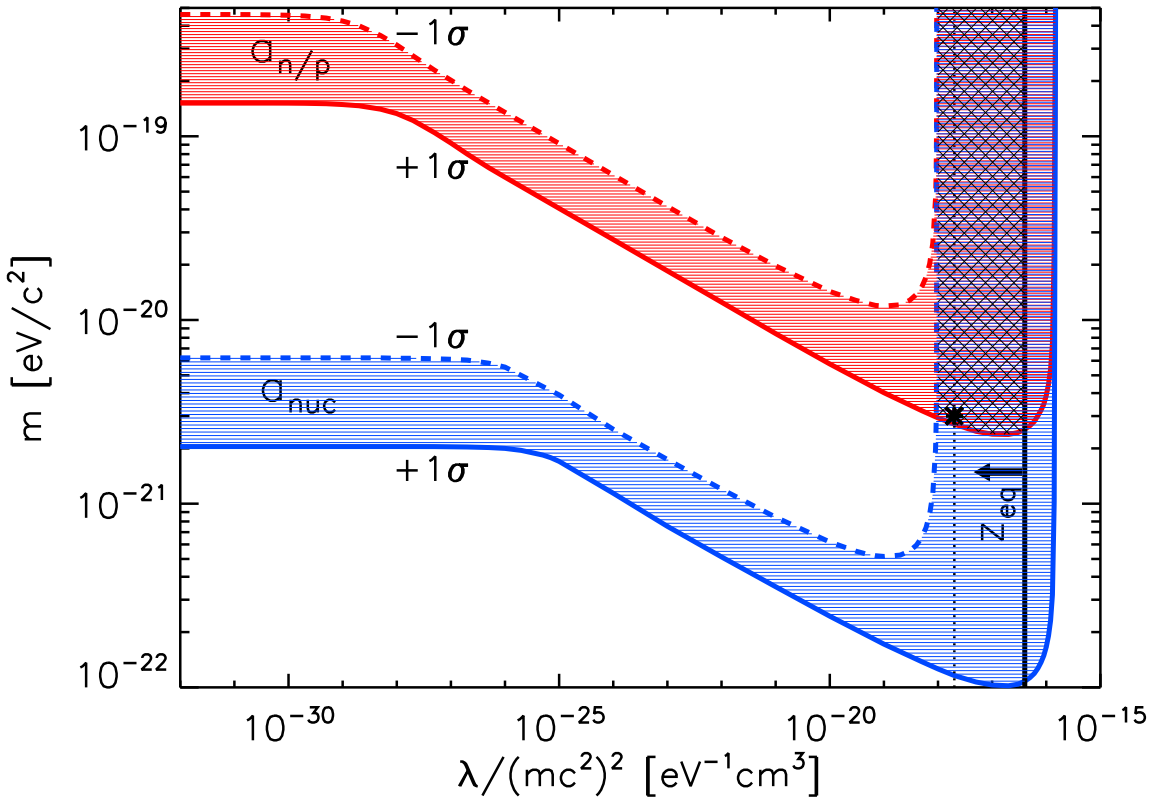

Figure 1.5: Parameter space of SFDM ($\lambda/(mc^2)^2$, m). The solid vertical line represent the upper bound on $\lambda/(mc^2)^2$ which makes SFDM complete its transition from radiationlike to CDM-like (i.e. $\langle\bar{w}\rangle = 0.001$) just before the observed $z_{\rm eq}$. The arrow indicates that the region on the left side of the solid vertical line is allowed by this constraint from $z_{\rm eq}$. The two shaded bands are the allowed regions derived from the constraints that $N_{\rm eff}$ be within the 1σ interval of the value measured by BBN, at $a_{\rm n/p}$ and $a_{\rm nuc}$, as labeled respectively. For each band, the thick solid (dashed) boundary curve corresponds to the upper (lower) 1σ limit of the measured value of $N_{\rm eff}$ in equation (1.40). The final allowed region is crosshatched, after combining all constraints. Our fiducial model, indicated by the star at $m = 3\times10^{-21}{\rm eV/c^2}$, lies on the dotted vertical line at $\lambda/(mc^2)^2 = 2\times10^{-18}$ eV^{-1} cm^3 which corresponds to a radius of an equilibrium halo around 1 kpc .

1.5 discussion

1.5.1 Relation between $N_{\rm eff}$ and smallest dark matter structure

We mentioned in the introduction that standard CDM meets challenges on small scales (mainly the cuspy core problem and the missing satellites problem), which could be possibly resolved if dark matter clustering is prohibited below certain scales. As a matter of fact, it has been pointed out in previous literature, e.g., Refs. [42, 66, 45], that self-interacting SFDM implies a minimum length scale $\sim l_{\rm SI}$ for a virialized object. Though it is negligible compared with the energy density, as we pointed out in Section 1.3.2.1 (i.e., SFDM behaves as collisionless dust on large scales), this self-interaction pressure affects the dynamics of small-scale nonlinear structures in the dark matter, just as thermal gas pressure does for the baryons.

In fact, equation (1.27) is an $n = 1$ polytropic equation of state $p \propto \rho^2$, whose coefficient is proportional to $\lambda/(mc^2)^2$. This is true even for the inhomogeneous case, if we replace the background $\langle\bar{p}_{\rm SFDM}\rangle$ and $\langle\bar{\rho}_{\rm SFDM}\rangle$ by local values. Therefore, the minimum length scale in the self-interaction-dominated limit is then given by the radius of a virialized $n = 1$ polytrope

$$R = \pi\sqrt{\frac{\lambda}{4\pi G m^2}} = \pi c^2\sqrt{\frac{\lambda}{4\pi G(mc^2)^2}}, \tag{1.44}$$

which is a function of $\lambda/(mc^2)^2$ only [42]. Note that $R \propto l_{\rm SI}$ up to a factor of order unity, and it is more precise to use R for purposes with regard to a virialized dark matter halo.

On the other hand, we have verified in Section 1.4.2 that as $N_{\rm eff}$ reaches the plateau (SFDM reaches the radiationlike phase), its value is also purely determined by $\lambda/(mc^2)^2$. Therefore, we can plot the polytrope radius against $N_{\rm eff}$ corresponding to the plateau, re-

vealing a hitherto unnoticed relation between the scale of the smallest dark matter structures and the number of relativistic species in the radiation-dominated era, see Figure 1.6.

The plot shows that higher $N_{\rm eff}$ implies stronger self-interaction pressure hence larger minimum scale for dark matter structure. The constraints discussed in the above section gives the allowed window of the minimum length scale, which is the segment of the curve between the left dotted vertical, the lower 1σ limit from BBN measurement, and the solid vertical, the bound from the constraint on $\lambda/(mc^2)^2$ by $z_{\rm eq}$, see equation (1.38). We can see that our fiducial model which corresponds to a minimum length scale of 1.1 kpc lies within the allowed window. It is a satisfactory result since this is about the scales where the small-scale CDM problems start to be significant from observations [20, 21, 22]. We should also note that the allowed window for the minimum length scale is subject to changes in future observational results from CMB and BBN.

1.5.2 Imprints on the CMB from a time varying $N_{\rm eff}$

Besides BBN, the angular power spectrum of the CMB temperature fluctuations can also be used to constrain the expansion rate of the universe during the radiation-dominated era by the ratio of the Silk damping scale θ_D to the sound horizon scale θ_* [7]. This provides a different constraint on $N_{\rm eff}$ from that described above from BBN. While the expansion rate depends upon the number of relativistic species present as well, it should be noted, though, that because of its possible evolution, the $N_{\rm eff}$ affecting the CMB power spectrum is not the same as the $N_{\rm eff}$ during BBN. The former concerns its value during the epoch spanned by the moment at which the smallest angular scale probed ($l \sim 3000$) enters the horizon, $z_{\rm entry} \sim 6 \times 10^4$, to that of matter-radiation equality at $z_{\rm eq} \sim 3 \times 10^3$, as pointed out in Ref.

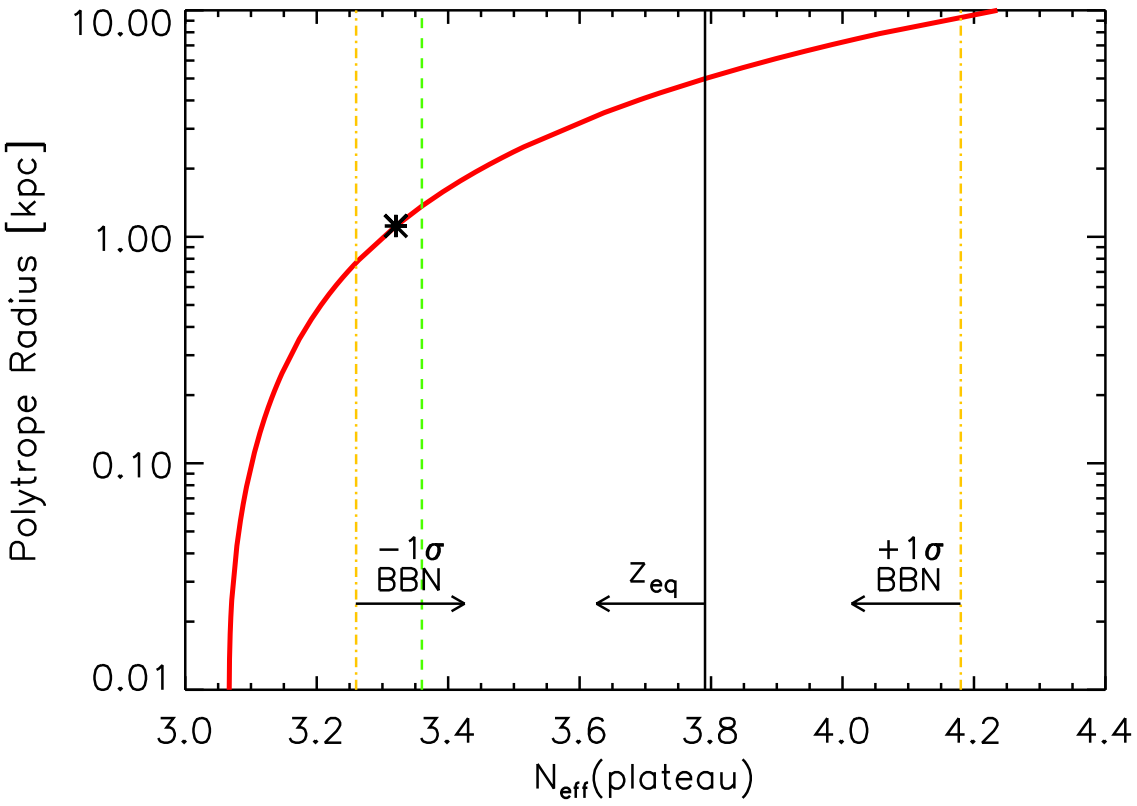

Figure 1.6: Radius of a virialized, polytropic SFDM halo, which forms during the matter-dominated era, as a function of $N_{\rm eff}$ during the radiation-dominated era. The relation is shown by the solid curve, on which the star represents our fiducial model. The polytrope radius is considered as the minimum length scale of structures. The two dash-dotted vertical lines indicate the 1σ limits of $N_{\rm eff}$ from BBN measurements, while the dashed vertical line indicates the central value of $N_{\rm eff}$ from CMB measurements (the latter is the same as in Fig. 1.4, lower plots). The solid vertical line denotes the upper bound of $N_{\rm eff}$ during the plateau so as to fulfill the constraint from fixed $z_{\rm eq}$.

[67]. By contrast, the BBN constraint probes $N_{\rm eff}$ at $z \gtrsim z_{\rm nuc} \sim 3 \times 10^8$. In the ΛSFDM model, $N_{\rm eff}$ evolves over time in such a way that $N_{\rm eff}$ is (at most) its plateau value at $z_{\rm entry}$, and finally reduces to the standard value of 3.046 when SFDM becomes fully non-relativistic (before $z_{\rm eq}$, as explained in Section 1.4.1). Therefore, the plateau value of $N_{\rm eff}$ during the radiation-dominated era serves as an upper bound for what is responsible for the expansion rate from $z_{\rm entry}$ to $z_{\rm eq}$.

However, a complication arises that the ratio of θ_D/θ_* does not only depend on the expansion rate during the period mentioned above, but also on the primordial Helium abundance Y_P, since the damping tail is subject to the number density of free electrons n_e [6]. Actually,

$$\theta_D/\theta_* \propto \sqrt{\frac{H}{n_e}} \propto \sqrt{\frac{H}{1-Y_P}}, \tag{1.45}$$

where H refers to the Hubble expansion rate between $z_{\rm entry}$ and $z_{\rm eq}$. We also know that Y_P is dependent upon $N_{\rm eff}$ during BBN (an increase in $N_{\rm eff}$ results in a higher Y_P). Therefore, the relativistic degrees of freedom suggested by CMB measurements, e.g., $N_{\rm eff} = 3.36 \pm 0.34$ given by Planck+WP+highL [7], (again, models with *constant* $N_{\rm eff}$ are fitted to the data) is in fact an imprint from both $N_{\rm eff}$ during BBN at early times (through Y_P) and its later evolution from $z_{\rm entry}$ to $z_{\rm eq}$ (through H), in ΛSFDM. In fact, equation (1.45) implies that θ_D/θ_* increases when either H or Y_P increases, provided a higher $N_{\rm eff}$ at the respective epoch, which then suggests that, $N_{\rm eff}$ given by CMB measurements be between the $N_{\rm eff}$ during BBN and the $N_{\rm eff}$ from $z_{\rm entry}$ to $z_{\rm eq}$ (the exact relation requires the calculation of linear growth). We then note that SFDM naturally provides an explanation for the difference between the $N_{\rm eff}$ values currently measured from BBN and CMB, in which the BBN value is larger than the CMB value.

1.5.3 Early stiff-matter phase

We have seen in Section 1.3.2.2 that SFDM undergoes a stiff phase, when $\bar{p}_{\rm SFDM} \approx \bar{\rho}_{\rm SFDM}$ and $\bar{\rho}_{\rm SFDM} \propto a^{-6}$. This feature of scalar fields has been noted before in models where the scalar field describes post-inflation universe or dark energy; see, e.g., Refs. [68, 55, 69]. In Ref. [51], this feature has been found for SFDM without self-interaction. However, these authors did not find the accompanying constraint on the particle parameters, and also were limited to analytic treatment, while we calculated the evolution numerically and explore the parameter space where the stiff phase is important. The first suggestion of a stiff equation of state for the baryonic fluid in the early universe seems to be by Refs. [70, 71]. The possibility of pre-BBN non-standard expansion histories, which includes a component decaying as a^{-6}, has been considered, e.g. in Refs. [72] and [56]. However, the stiff components studied there do not undergo any transition, i.e., always decay as a^{-6}, unlike our model.

In a ΛSFDM universe, the stiff phase can last until BBN occurs due to the constraints on the expansion rate. As we have seen in Section 1.4.2, for all viable models the stiff phase completely ends before $a_{\rm nuc}$. An interesting question is whether the stiff phase before $a_{\rm n/p}$ will affect baryonic processes so as to leave an imprint on BBN products. In fact, the free neutron abundance is subject to beta decay, which happens ever since neutrons have existed, going as e^{-t/τ_n} with the neutron decay time τ_n. Thus, the number of free neutrons left for nucleosynthesis depends on the age of the Universe, t, since the QCD phase transition. Now, if $t = 1/(3H)$ in the stiff phase, instead of the radiation-era dependence, $t = 1/(2H)$, this will change the number of available free neutrons before $a_{\rm nuc}$. The change in the age of the Universe is marginal, though, with a factor of 1/3, instead of 1/2, to multiply the decay-factor. As shown in the left-hand plot of Figure 1.2, the Hubble time at the epoch of the

stiff-radiation transition is $\lesssim 1s \ll \tau_n$, which actually applies to all viable models. It is thus safe enough to constrain SFDM parameters only during BBN.

As far as the QCD phase transition is concerned, which happens somewhere between 150 – 300 MeV, there is still a lot of ongoing work to understand those processes in full. However, the relaxation time of the strong force is so tiny, in contrast to the Hubble time, that the QCD transition takes place in chemical equilibrium all the time, without a freeze-out timing issue. Therefore, we think the universe can be in the SFDM-dominated era in the stiff phase with a higher expansion rate, as suggested by our model, and yet accomplish a standard hadron era.

1.5.4 Implications for fuzzy dark matter

Our analysis above is valid for arbitrary value of λ. It is natural, therefore, to ask what the implications of our constraints are for the limiting case of $\lambda = 0$. SFDM without self-interaction, $\lambda \equiv 0$, or fuzzy dark matter, is left with the quadratic potential in (1.5). Its popularity is reflected by numerous previous investigations; see, e.g., Refs. [73, 40, 44]. One reason is that, even without the self-interaction pressure associated with nonzero λ, FDM still provides a mechanism to suppress structures on scales below $\lambda_{\rm deB}$, as a result of quantum pressure due to the Heisenberg Uncertainty Principle. Since it is an important special case of the model we have investigated, we devote this subsection to summarize the implications for this model from our analysis.

Without the self-interaction term, FDM has only two evolutionary phases, the early relativistic, stiff-matter phase, followed by the non-relativistic, CDM-like phase. For values of m which are large enough to make this transition occur before the BBN epoch, the redshift

of matter-radiation equality, $z_{\rm eq}$, is unaffected because of the absence of the plateau (the radiationlike phase). Nevertheless, BBN sets a constraint on the only parameter left, the mass m. Since the kinetic term in the SFDM energy density (1.17) goes inversely with m, the transition between stiff and dust-like equation of state happens *later* with *decreasing* mass. In fact, according to Figure 1.5, if we accept the 1σ limits on $N_{\rm eff}$ allowed by BBN to constrain m, there is *no* value of m for which $\lambda = 0$ can be consistent, which indicates a rejection of the FDM model at $\geq 1\sigma$. We highlight this result, since FDM with $m \sim 10^{-23} - 10^{-22}$ eV$/c^2$ has been a very popular candidate in the literature because the minimum length scale $\sim \lambda_{\rm deB}$ that corresponds to such particle mass is roughly 1 kpc, as mentioned in the introduction. Again, we should admit that, placing a less tight constraint, e.g., within 2σ, FDM may be able to fit BBN measurements.

1.6 Conclusions

We presented the cosmological evolution of a universe in which dark matter is comprised of ultralight self-interacting bosonic particles, which form a Bose-Einstein condensate, described by a classical complex scalar field (SFDM). We solved the Klein-Gordon and Einstein field equations for the time-dependence of an FRW universe with this form of dark matter, and placed constraints on the SFDM particle mass m and self-interaction coupling strength λ (or equivalently $\lambda/(mc^2)^2$) from cosmological observations.

Unlike standard CDM, which is always non-relativistic once it decouples from the background, SFDM has an evolving equation of state. As a result, there are four eras in the evolution of a homogeneous ΛSFDM universe: the familiar radiation-dominated, matter-dominated and Lambda-dominated eras common to standard ΛCDM as well, but also an

earlier era dominated by SFDM with a stiff equation of state. Then, $\bar{p} \simeq \bar{\rho} \propto a^{-6}$ and $a \propto t^{1/3}$. The manifestation of this era does not depend on whether self-interaction has been included or not. It appears in fuzzy dark matter models with $\lambda \equiv 0$ as well. The timing and longevity of this era (or the stiff phase of SFDM), however, depend on the particular values of SFDM particle parameters, m along with $\lambda/(mc^2)^2$. It is necessary to ensure that the stiff phase is ending when big bang nucleosynthesis begins. This finding is a special novelty of our analysis. At intermediate times, SFDM is radiationlike, with $\bar{p} \simeq \bar{\rho}/3$. Finally, SFDM must transition to the CDM-like phase before the epoch of matter-radiation equality, and thereafter behaves as a pressureless dust.

The effect of this SFDM equation of state evolution on the expansion rate and mass-energy content of the universe enables us to place constraints on m and $\lambda/(mc^2)^2$, by using $N_{\rm eff}$ at BBN, and $z_{\rm eq}$ measured by CMB anisotropy. We find that $m \geq 2.4 \times 10^{-21}{\rm eV}/c^2$ and $9.5 \times 10^{-19}{\rm eV}^{-1}{\rm cm}^3 \leq \lambda/({\rm mc}^2)^2 \leq 4 \times 10^{-17}{\rm eV}^{-1}{\rm cm}^3$. While we are able to place more stringent bounds on these particle parameters than the previous literature, there remains a large range of SFDM parameters which provides an expansion history in conformity with cosmological observations. Our investigations thereby contribute to previous efforts in establishing SFDM as a viable dark matter candidate. Work is in progress to study the linear and nonlinear growth of structures in a ΛSFDM universe, in order to find out which part of the parameter space of SFDM is able to explain observations on all scales self-consistently.

Chapter 2

Inflationary Stochastic Gravitational-Wave Background in ΛSFDM Cosmology[1]

2.1 Introduction

2.1.1 Cold dark matter: WIMPs or something else?

The nature of the dark matter (DM) remains one of the most profound open problems in cosmology. Observations of the large-scale structure (LSS) of the universe and the cosmic microwave background (CMB) are consistent with dark matter which forms structure as if it was created "cold", i.e., it can be modeled as collisionless particles with nonrelativistic random microscopic motions. The cold dark matter (CDM) model has been very successful in describing structure formation on large scales as hierarchical, with the smallest objects forming first and merging over time to form ever-larger objects — "halos" in virial equilibrium — connected by filaments surrounding largely empty voids in a "cosmic web of structure" [75], [76, 77], [78], [10, 79], [80]. Candidate particles for DM can be found in many extensions to the Standard Model (SM) of particle physics. Traditionally, the most studied candidate particles for the standard, collisionless CDM are WIMPs (weakly interacting massive parti-

[1]This chapter is based on our paper published in *Phys. Rev. D*, Li, Shapiro, Rindler-Daller 2017 [74] ("Paper II"). Bohua Li is the lead author of this publication, who integrated the ideas which led to the formulation of the basic equations of this model, developed the iteration algorithm to calculate its numerical solutions to produce the results (including most of the figures) of this paper, and incorporated the method of the SGWB signal analysis from LIGO to enable the LIGO detectability prediction of this model.

cles), the lightest supersymmetric partner particles predicted by models of supersymmetry ("SUSY"), thermal relics whose mass range allows gravitational clustering to form objects down to Earth-mass.

Despite its success on large scales, the standard, collisionless CDM model has been challenged by observations of galactic and sub-galactic scales. First, N-body simulations of collisionless CDM predict a universal cuspy density profile for DM halos. However, measurements of the density profiles of various dark-matter-dominated systems, e.g., dwarf spheroidal galaxies, low-surface-brightness galaxies, even some galaxy clusters, have suggested shallower profiles, or even cores at their centers (the "cusp/core problem") [19, 81, 22, 82, 83]. Such N-body simulations also predict a large-overabundance of subhalos in the Local Group compared with the observed number of satellite galaxies (the "missing satellites problem") [14, 15]. In addition, it has been pointed out that, after abundance matching, the most massive subhalos of a Milky-Way-like galaxy predicted by standard CDM simulations are too dense to host the brightest satellites of the Milky Way (the "too big to fail" problem) [84, 85].

Meanwhile, attempts to detect WIMP DM particles either directly or indirectly (i.e., as astronomical sources following their decay or annihilation into radiation or other particles) have thus far been unsuccessful [86, 87, 88, 89]. The range of particle models and parameters which remain viable for WIMP DM has, in fact, been substantially reduced by these nondetections.

These nondetections of WIMPs and the structure formation discrepancies described above, between theory and observations, for the standard model of CDM as cold, collisionless particles suggest that an alternative at the particle level to WIMPs as CDM may be required.

Such an alternative must retain the successes of CDM with regard to LSS formation and the CMB, as well as the thermodynamic evolution of the background universe in the standard Big Bang cosmology.

One such variant of CDM which we have considered before is that of complex scalar field dark matter (SFDM), for which *all* cosmological dark matter is composed of ultralight bosons [45, 52, 90] (where it is referred to as Bose-Einstein condensate CDM, or BEC-CDM); [1] (hereafter "Paper I"). For additional descriptions of this model and the related literature, we refer the reader to these papers. With regard to LSS, SFDM provides a natural length scale, below which structure formation is suppressed, leading to fewer subhalos and generally, to a lower density of DM in the central regions of galaxies. On larger scales, however, structure formation in SFDM is the same as for cold, collisionless particles.

In Paper I, we considered the cosmological evolution of the homogeneous Big-Bang background universe in the presence of SFDM and showed that the SFDM behaved like a perfect fluid with an equation-of-state (EOS) parameter $w \equiv p/\rho$ which evolved from stiff ($w = 1$) to radiationlike ($w = 1/3$) to nonrelativistic CDM-like ($w = 0$). The energy density of SFDM during this last CDM-like phase, equal to the product of the rest-mass energy density per particle and the particle number density, is chosen to match the observed dark matter mass-energy density in the Universe today. At early times the stiff EOS made the SFDM dominate the total energy density of the universe, with consequences for the expansion history. This made it possible for us to use observational constraints to derive the allowed range of SFDM particle parameters. Here we will revisit this problem by making two significant advances, as described in the sections below. First, we will embed the SFDM model more fully in the standard inflationary paradigm, to create a more holistic ΛSFDM

cosmology. Second, we will take account of the gravitational-wave (GW) background from inflation and its amplification in the presence of SFDM, leading to the possibility of its detection at high frequencies by laser interferometer experiments like the Advanced LIGO/Virgo experiment (shortened as "aLIGO/Virgo"). A preliminary summary of some of this new work was presented in [91].

2.1.2 Complex SFDM: Bose-Einstein-condensed ultralight particles as cold dark matter

The SFDM model considered in Paper I and in [45, 52, 90] is one type in a family of cold dark matter candidates involving bosonic particles associated with a scalar field. The best-known example of bosonic dark matter is the QCD axion, a real (pseudo-)scalar field proposed to resolve the strong CP problem. Its attractive self-interaction is so weak that it is usually neglected, leaving only the quadratic mass term in the potential. The mass of the QCD axion currently allowed by astronomical observational constraints is $\sim 10^{-5}$ eV/c^2. Structure formation in QCD axion DM is like that for cold, collisionless particles on all scales of astrophysical interest, so the small-scale structure problems of CDM described above in §2.1.1 remain for the QCD axion DM, as well. As a generalization, ultralight axions or axion-like particles (ALPs) are also predicted by extensions to the Standard Model, which could serve as dark matter as long as their mass is $> 10^{-33}$ eV/c^2 $\sim$ $H_0 \cdot \hbar/c^2$ (H_0 is the Hubble constant at the present). The self-interaction of these ultralight ALPs, too, is generally assumed to be so weak that it can be neglected when comparing model predictions to astrophysical data. However, we caution against this neglect, since our SFDM results for the case which includes a *repulsive* self-interaction, show that even a tiny self-interaction can be dynamically important; it is not clear why the same should not be true for attractive cases.

When the mass of the non-interacting axion is above 10^{-18} eV/c^2, dark matter comprised of ALPs is dynamically indistinguishable from collisionless CDM on large scales [92]. For particle masses smaller than this, however, their de Broglie wavelength inside galactic halos, which sets a scale below which structure formation is suppressed, can be large enough to affect the small scales identified in §2.1.1 above as problematic for standard CDM.

In fact, other ultralight scalar field particles have been proposed as DM candidates by various authors, which all mimic standard CDM above some length scale but deviate on sufficiently small scales, motivated by the small-scale problems of standard CDM. While the genesis of ultralight bosonic DM is *a priori* model-dependent, many of those models share the property of axion DM that the DM bosons are considered to be born cold with high occupation number, such that they can be described by a classical scalar field. The choice of potentials and particle masses does vary, however. Non-interacting DM has been considered by, e.g., [40], [59], [43, 54, 93] ("fuzzy dark matter"), [94] ("quantum wave dark matter"), [95, 96] ("ultralight axions"), [97, 44] ("scalar field dark matter"), [98]. On the other hand, self-interacting DM has been studied in, e.g., [49] ("fluid dark matter"), [42, 99] ("repulsive dark matter"), and [100, 62, 66, 33, 46, 101, 102]. In the self-interacting[2] DM case (including our SFDM model with a quartic potential [45, 52, 90], referred to there as BEC-CDM), the suppression of small-scale structure can also result from the pressure force associated with its repulsive potential, rather than solely from the "quantum pressure" associated with large de Broglie wavelength as in the non-interacting case. When the minimum length scale for

[2]The self-interaction term used here should not be confused with the kind of self-interacting CDM particles referred to elsewhere in the literature as SIDM, suggested by [103], which we have studied in [104] and [105]. In SIDM, particle self-interaction manifests itself as two-body elastic scattering which adds "collisionality" to the otherwise collisionless CDM gas, but does not make a BEC or exhibit any form of macroscopic quantum coherence.

structure associated with the repulsive self-interaction is greater than that due to quantum pressure, this is referred to as the Thomas-Fermi regime.

Amongst the models mentioned above, there are many which propose that DM bosons are initially in a Bose-Einstein condensate (BEC), or will form a BEC at some stage in cosmic history. In our previous work [45, 52, 90], we studied the nonlinear behavior of the BEC wave function (or, the order parameter), in the context of DM halo structure. We applied the Gross-Pitaevskii equation coupled to the Poisson equation to study the equilibrium structure of BEC-CDM halos, including the effects of angular momentum and the possible formation of quantum vortices.

The formation of a BEC in QCD axion DM has also been studied in the literature. A detailed analysis of the condensation process for the QCD axion has been made by [38, 39]. However, controversies remain about the formation of a BEC and whether it depends on the sign of the self-interaction or whether the classical field description is sufficient in general [106, 107]. This debate is partly due to the difficulty of forming a BEC for bosons described by a *real* scalar field (the axion case), while the condensation process occurs naturally, even in the early universe, for bosons described by a *complex* scalar field (the case for our SFDM model) with a global $U(1)$ symmetry, associated with a (conserved) Noether charge [36, 35, 108], as described below.

In the *complex* SFDM model presented here, DM appears in the wake of reheating, following inflation. An example of such a microphysical implementation can be found in [108]. The idea is that, upon inflaton decay, DM bosons and antibosons are created, as are the SM particles. We assume that the complex scalar field was born with a large charge, or comoving charge density, Q, which is the difference between the comoving number density of bosons

and antibosons, i.e., $Q \equiv n_+ - n_-$. Owing to the global $U(1)$ symmetry of the complex scalar field, Q is a conserved quantity. In thermal equilibrium, while DM bosons and antibosons are annihilated away (leaving no antibosons behind), the majority of DM particles will find themselves rapidly occupying their ground state (the zero-momentum state). In Paper I, following [36] and [35], we pointed out that Bose-Einstein condensation for DM particles of mass m occurs as long as $k_{\rm B}Q/S \gg 1$ initially, where $k_{\rm B}$ is the Boltzmann constant and S is the comoving entropy density. In a cosmological setting, both Q and S are conserved. Now, that ground state which remains is a BEC with charge approximately equal to Q. As a result, the DM can thereafter be described as a classical field, hence complex scalar field dark matter – SFDM.

We note that complex SFDM belongs to the wider family of *asymmetric* DM, in which the DM antiparticles annihilate away, along with an equal number of particles, leaving only the excess of particles over antiparticles behind. In this "large-charge" limit, the charge density Q (where $Q \simeq n_+$) is then related to the present-day SFDM energy density, $\rho_{\rm SFDM,0}$, by $Qmc^2/\rho_{\rm SFDM,0} \simeq 1$. This situation is described by [51] as leading to a "spintessence" phase at later times (see also [109], [58]). They also described the other limit in which $Qmc^2/\rho_{\rm SFDM,0} \ll 1$, the "small-charge" limit , i.e., negligible comoving charge density. This small-charge limit would correspond, instead, to the opposite assumption of *symmetric* DM, i.e., nearly equal numbers of particles and antiparticles today, so $n_+ \simeq n_-$. Hereafter, since we shall only be interested in the large-charge limit, in which the dynamics of the complex scalar field differs from that of a real scalar field, as we discuss below in §2.1.3, the notation "SFDM" shall only refer to the *complex* scalar field dark matter in the large-charge limit considered here.

2.1.3 Cosmic Evolution of ΛSFDM

We studied the (background) evolution of complex SFDM in detail in Paper I, by solving numerically the equation of motion of SFDM in an expanding universe, adopting a spatially flat Friedmann-Lemaître-Robertson-Walker (FLRW) background metric. We called it ΛSFDM, since all the cosmic components of the ΛCDM model are adopted, except for collisionless CDM, which is replaced by SFDM. We assumed that the present cosmic DM abundance is entirely given by the current $\rho_{\rm SFDM}$, which also determines the (conserved) comoving charge density of SFDM, Q, as described in the sections above. The evolution of SFDM is determined by the form of the potential in its Lagrangian, as for any other cosmological scalar field. Let ψ be the complex scalar field describing the condensate of DM bosons. We adopt the following Lagrangian density (in units of energy density),

$$\mathcal{L} = \frac{\hbar^2}{2m} g^{\mu\nu} \partial_\mu \psi^* \partial_\nu \psi - \frac{1}{2} m c^2 |\psi|^2 - \frac{\lambda}{2} |\psi|^4, \tag{2.1}$$

with signature $(+,-,-,-)$. $|\psi|$ denotes the modulus of ψ. m is the DM boson mass, and we choose the energy-independent 2-boson self-interaction strength to be repulsive or zero, $\lambda \geq 0$. We will elaborate more on this Lagrangian density in §2.2.1.1.

The range of SFDM parameters of interest is motivated by the small-scale CDM structure problems mentioned above. In its CDM-like phase—when the quadratic term in Eq. (2.1) dominates—, SFDM can provide two characteristic (Jeans) length scales below which structure formation is suppressed. Regardless of self-interaction, the quantum nature of SFDM particles always smoothes fluctuations below their de-Broglie wavelength. For example, DM particles with mass $m \simeq 10^{-22}$ eV/c^2 would have a corresponding de-Broglie wave length $\lambda_{\rm deB}$ of order a kpc (i.e., typical scale of CDM small-scale structure problems).

Moreover, there arises another length scale, $l_{\rm SI}$, from the (repulsive) self-interaction, should it be significant, given by $\lambda/(mc^2)^2$. In fact, in the Thomas-Fermi regime, $l_{\rm SI}$ is the only length scale that is responsible for suppressing structure growth, because then $l_{\rm SI} \gg \lambda_{\rm deB}$. For instance, $l_{\rm SI} \simeq 1$ kpc if $\lambda/(mc^2)^2 = 2 \times 10^{-18}$ eV^{-1} cm^3. Hence, m can be larger than the value of interest suggested by the noninteracting case, if λ is higher as well, and yet the model retains its characteristic length scale, as long as the ratio $\lambda/(mc^2)^2$ stays constant (see [45] for details). In this paper, the SI is adopted as the system of units, in which $[m] =$ eV$/c^2$ and $[\lambda] =$ eV cm^3. We note that fiducial dimensional couplings of order $\lambda \approx 10^{-62}$ eV cm^3 correspond to dimensionless couplings of order[3] $\lambda m^2 c/\hbar^3 \approx 10^{-92}$ for $m = 10^{-22}$ eV$/c^2$. While couplings even this small are enough to resolve the small-scale problems for higher mass DM particles, they also render these models qualitatively different[4] from those with $\lambda \equiv 0$.

In Paper I we found that, for the large-charge regime of interest, self-interacting SFDM starts relativistic in the early universe, with an equation of state (EOS) evolving from stiff ($w \equiv p/\rho \simeq 1$) to radiationlike ($w \simeq 1/3$), before becoming nonrelativistic at late times ($w \simeq 0$). In the limit of a vanishing self-interaction ($\lambda \to 0$), the intermediate radiationlike phase of SFDM simply vanishes. In either case, it is the kinetic term in Eq. (2.1) that dominates the energy density of SFDM at early times, with a negligible oscillation whose frequency is less than the expansion rate, and the EOS of SFDM approaches that of maximally "stiff" matter, $w_{\rm SFDM} \simeq 1$. When the kinetic-energy-dominated scalar field is

[3]This number is roughly 40 orders of magnitudes below the coupling for a $m \sim 10^{-5}$ eV QCD axion. The self-interaction is attractive for the latter, however.

[4]This qualitative change in models, when a small coupling is added (i.e. a quartic term), has been found already earlier in the literature on boson stars, which are also described as self-gravitating scalar fields, see [63]. So, it is not too surprising to rediscover similar consequences for scalar fields as the dark matter.

also the dominant component of the universe, this period of the expansion history is referred to as "kination" [55, 110, 56].

It is important to note that this earliest stiff phase of SFDM is a generic feature of scalar field dynamics, e.g., [111]. However, unlike the case of a single real scalar field, a complex scalar field in the *large-charge* limit of interest here does not evolve from the stiff ($w = 1$) phase toward a slow-roll attractor (i.e., behaving like a cosmological constant, $w = -1$). The dynamical possibilities for a complex scalar field are actually richer than this, even for simple power-law potentials like $\frac{1}{2}mc^2|\psi|^2$. This is shown, for example, by [112]. For a complex scalar field with a $U(1)$ symmetry, the dynamical evolution of the field is different in the large- and small-charge limits, respectively. In the *small-charge* limit, the complex field can behave as an effective real scalar field, in which case the slow-roll phase described above is expected to appear, until the oscillation frequency of the field exceeds the expansion rate. After that, the phase angle of the complex scalar field remains almost fixed, while the oscillation is in the amplitude alone [51]. However, in the *large-charge* limit ($Q \simeq \rho_{\mathrm{SFDM},0}/mc^2$, the case of interest here), something very different happens. In this case, if the field starts out in a stiff phase, it does not evolve into a slow-roll phase before its oscillation frequency exceeds the expansion rate. And after that, the field evolves according to the pattern for which the oscillation is actually in the phase angle, rather than in the amplitude. In the latter case, the behavior of the field when the oscillation frequency exceeds the expansion rate is referred to as "spintessence", as mentioned in §2.1.2.

During this phase in which the oscillation frequency of the complex scalar field exceeds the expansion rate (the spintessence phase), the quartic term in Eq. (2.1) can dominate the SFDM energy density, for large enough $\lambda/(mc^2)^2$. Then, the EOS of SFDM is that of

radiation, namely $w_{\rm SFDM} \simeq 1/3$. The early universe thus experiences a boost in its expansion rate due to this extra relativistic species in both the stiff and radiationlike phases of SFDM. Eventually, the (quadratic) mass term in Eq. (2.1) comes to dominate, which guarantees that SFDM behaves like CDM in the late universe, with or without self-interaction. More precisely, this term must dominate after the time of matter-radiation equality at a scale factor of $a_{\rm eq} \simeq 3 \times 10^{-4}$, in order to reproduce a period of "CDM-like" matter domination with $w_{\rm SFDM} \simeq 0$, the same as that in ΛCDM during which structure forms.

The transitions between these phases, determined by SFDM particle mass and self-interaction coupling strength, are therefore constrained by cosmological observables, particularly $N_{\rm eff}$, the effective number of neutrino species during Big Bang nucleosynthesis (BBN), and $z_{\rm eq}$, the redshift of matter-radiation equality. There are other models that also change the expansion rate at early times relative to the standard model. Some of those do it by making the EOS of the universe stiffer than radiationlike (i.e., $w > 1/3$), while others do it by changing the number of relativistic species while leaving the EOS still radiationlike. For those models with an early era with an EOS stiffer-than-radiation, BBN abundance observations primarily place an upper limit on the duration of the stiff era – i.e., the stiff era must end before BBN. For those models with extra contributions to the total energy density with a radiationlike EOS, instead, the BBN constraint places an upper limit on the number of extra relativistic species, which is the same during BBN and at later times when observables like $z_{\rm eq}$ and the CMB anisotropy place additional constraints on $N_{\rm eff}$, independently. In our model, however, the evolution of the SFDM EOS causes *both* of these effects to occur: the stiff-SFDM-dominated early era *and* a relic radiationlike contribution *after* the stiff era ends. In this case, the SFDM model must satisfy both kinds of constraints, that

which limits the expansion rate *during* BBN and that which limits the extra radiationlike contributions *after* BBN, as well. For most other models, those constraints are expressed as an allowed range of values of $N_{\rm eff}$, assumed to be a fixed quantity which does not evolve during BBN or *between* BBN and $z_{\rm eq}$. The standard value of $N_{\rm eff,standard} = 3.046$ [65] accounts for the presence of the three Standard Model neutrinos. For the SFDM model, however, we must consider the *evolution* of $N_{\rm eff}$ and subject it to different constraints at different epochs. SFDM allows $N_{\rm eff}$ to be *higher* at BBN than at $z_{\rm eq}$, in fact, which current observations seem to prefer (see §2.4.2). In Paper I, we found that $m \geq 2.4 \times 10^{-21}$ eV$/c^2$ and 9.5×10^{-19} eV^{-1} cm$^3 \leq \lambda/(mc^2)^2 \leq 4 \times 10^{-17}$ eV^{-1} cm^3, due to cosmological constraints on $N_{\rm eff}$ and $z_{\rm eq}$.

To reiterate, before the familiar radiation-dominated era, there is an earlier era of stiff-SFDM-domination, and the expansion rate in the early ΛSFDM universe is increased compared with that in ΛCDM. Interestingly, in our model, dark matter dominates twice in the history of the universe: first in its stiff phase before BBN, and later in its dust-like phase, giving rise to a standard CDM-like matter era.

In this paper, we will expand our previous analysis by embedding ΛSFDM in the standard inflation paradigm and studying the impact of SFDM on primordial gravitational waves (GWs) produced during inflation, which contribute to $N_{\rm eff}$ as well.

2.1.4 SFDM within the standard inflationary cosmology

In Paper I, we showed that by setting the conserved charge of the complex scalar field so as to match the abundance of the DM in the observed universe at the present, and evolving the field and background universe together over time, the field was compelled to dominate the total energy density at early times. We stopped short, however, of asking how

this SFDM-dominated phase was consistent with standard inflationary cosmology in which the energy density was dominated initially by the inflaton field. Here we merge these two pictures self-consistently by postulating that the end of inflation was followed by reheating, in which the inflaton decayed primarily into SFDM, while also producing the other particles of the SM.

More precisely, we envisage the early cosmic evolution as follows. Standard slow-roll single-field inflation produces nearly scale-invariant fluctuations of the metric of the universe, which can be decomposed into scalar, vector and tensor fluctuations. The energy scale during inflation is related to the ratio of the amplitude of tensor perturbations to the scalar amplitude, also called the tensor-to-scalar ratio, r. This quantity is pursued by CMB polarization experiments [113, 114], because primordial tensor perturbations induce quadrupole anisotropies in the CMB temperature, which leaves an imprint on the B-mode of CMB polarization (the "recombination bump" in the BB power spectrum) [115, 114]. The spectrum of (nearly) scale-invariant tensor perturbations can be parametrized by a power law, determined by the tensor amplitude A_t (the product of the scalar amplitude A_s and r) and the tensor spectral index n_t. These tensor perturbations will become gravitational waves (GWs) once they reenter the horizon. We further assume that inflation is followed by an epoch of reheating with matter-like EOS, $w = 0$. This is a reasonable, standard choice for a prolonged period of reheating (see, e.g., [116]). As already described in §2.1.2, we are interested in scenarios in which the DM bosons are born at the end of reheating with a high charge density and low entropy density, and thus find themselves rapidly occupying their ground state (the zero-momentum state). As soon as SFDM arises, its energy density obeys a stiff EOS ($w = 1$). Again, this is because, for a scalar field, the kinetic term in

the Lagrangian, Eq. (2.1), goes as a^{-6}. Since SFDM dominates the cosmic energy budget at early times, compared to other cosmic components, the stiff EOS of the SFDM is also the EOS of the universe at this time. For simplicity, we adopt an instant transition, i.e. the reheating temperature $T_{\rm reheat}$ at the end of reheating also corresponds to the point after which there is the "stiff-SFDM-dominated" era.

We note that in this work the only source of primordial GWs that we consider are those predicted by the "plain-vanilla" single-field, slow-roll inflation model, for which the consistency relation, $n_t = -r/8$, holds. Tensor fluctuations from inflation are isotropic and stochastic in nature. Therefore, they contribute to the stochastic gravitational wave background (SGWB), giving rise to an effective homogeneous energy density of primordial GWs, which we will elaborate in more detail in §2.2.1.2. Such a SGWB is described by its energy density spectrum, $\Omega_{\rm GW}(k, a)$, i.e. the fraction of the critical energy density carried by GWs per logarithmic wavenumber interval at any comoving wavenumber k and scale factor a. The dispersion relation of GWs today is simply given by $f = kc/2\pi$, in which f is the (comoving) frequency. The differential GW energy density at any frequency f generically decays like radiation $\sim a^{-4}$ once that mode reenters the horizon.

As we will show in this paper, it is the stiff era caused by SFDM that will amplify the GWs produced during inflation. It was first considered by Grishchuk in his seminal paper [117] that cosmological GWs can be amplified in a universe whose EOS is stiffer than that of radiation, i.e., $w > 1/3$, implying that the corresponding $\Omega_{\rm GW}(k, a)$, which indicates their contribution to the total energy density of the universe, will increase over time. The results in Grishchuk's paper showed the conditions in which gravitons can be massively produced in the early universe, from initial tensor-type quantum fluctuations, which were later developed

and applied to the modern-day inflationary paradigm (see [118] and references therein for a review). In contrast, we study the post-inflationary evolution of existing GWs produced during standard inflation.

We will point out in this paper that, for any mode k, the value of $\Omega_{\rm GW}(k,a)$ measured at some time long after that mode reenters the horizon depends on the critical energy density of the universe when it is measured, and two things which are k-dependent: the critical energy density at the time of its horizon-crossing and the number of e-foldings between the horizon-crossing and the measurement. We will show that, for any mode k which reenters prior to the end of the stiff phase, it is the shortening of the time spent undergoing radiationlike decay due to the stiff phase, compared to the ΛCDM expansion history, that is responsible for the amplification of $\Omega_{\rm GW}(k,a)$. The expansion history of ΛSFDM with its stiff era will, therefore, predict a characteristic GW energy density spectrum $\Omega_{\rm GW}(k,a)$ at a late time, in which the spectrum shows a blue-tilt, $\Omega_{\rm GW}(k,a) \propto k$, for any mode k reentering during the stiff era ($w=1$), a peak at $k_{\rm reheat}$ for the mode that reenters at the end of reheating ($w=0$), and a decline for higher k as $\Omega_{\rm GW}(k,a) \propto k^{-2}$ (red-tilt).

We calculate here the present-day GW energy density spectrum, $\Omega_{\rm GW}(f) \equiv \Omega_{\rm GW}(k = 2\pi f/c, a=1)$, as probed by current and future laser interferometer experiments [119, 120]. These experiments are sensitive to the tensor deformation of space, or the strain, induced by incoming GWs, to a high accuracy. We predict a detectable signal from the SGWB generated by *standard* inflation, which is within reach of the sensitivity of the ongoing Advanced LIGO/Virgo experiments, for a broad range of $T_{\rm reheat}$ and SFDM parameters. This provides a novel science target, given that the expected signal from the standard cosmological model lies many orders of magnitudes below the sensitivity limit of those experiments. Meanwhile,

pulsar timing array (PTA) experiments [121, 122, 123] also detect strain signals, but at lower frequency ranges. We remark that the predicted SGWB signal in the ΛSFDM model, however, lies well below the upper bounds reported by current PTA experiments in those frequency ranges.

The SGWB also affects the expansion history as an extra relativistic degree of freedom by boosting the expansion rate of the background universe, thereby contributing to $N_{\rm eff}$. In contrast to ΛCDM with standard inflation, in which the contribution to the background energy density of the universe from primordial GWs is negligible (and thus uninteresting), ΛSFDM, however, amplifies those primordial GWs so that they need to be taken into account in the budget of $N_{\rm eff}$. Therefore, the SGWB from inflation actually needs to be included in the Friedmann equation for the average universe in a self-consistent manner. In other words, we must study the back-reaction of the inflationary SGWB on the expansion rate of the average universe, which in turn affects the evolution of the SGWB, itself, an effect which has been neglected in previous literature. We stress that we include the fully-coupled evolution of *all* the cosmic components in our calculation of the back-reaction. In light of this effect, $N_{\rm eff}$ thus has two additional sources: the direct contribution from SFDM, and a new one from the *enhanced* $\Omega_{\rm GW}$. This puts additional constraints on the SFDM parameters, m and $\lambda/(mc^2)^2$. In what follows, we will update the $N_{\rm eff}$ and $z_{\rm eq}$ constraints on the SFDM parameters studied in our Paper I, incorporating the new effect from primordial SGWB.

The impact on the primordial SGWB of an early era whose EOS is stiffer than radiation (with $1 \geq w \geq 1/3$) has been considered in different contexts in previous literature, in which such an era was postulated to arise before BBN. The possibility that inflation ended with the onset of a brief stiff era was considered by [124], who calculated the effect on the

inflationary SGWB energy density of assuming the EOS switched from a constant value of w in the range $1/3 < w \leq 1$ for the stiff era to $w = 1/3$ for the standard radiation-dominated era. A possible agent considered for the stiff era was quintessential inflation, studied in [48], in which the inflaton field transitions from a slow-roll phase to a kinetic-energy-dominated phase. Its impact on the SGWB has been considered in [125, 126], where a blue tilt in the GW energy density spectrum was predicted. However, unlike the present work, there was no standard reheating epoch between the end of inflation and the stiff era in those investigations. The requirement that the amplification of the SGWB relative to the standard radiation components not violate observational constraints on the early universe was discussed by [127] (based on [128]). They expressed this by defining an effective EOS parameter $\hat{w}$, which is a weighted mean of w over cosmic time, for which they calculated an upper limit. The above works pointed out that the high-frequency extrapolation of the same SGWB which contributed to the expansion rate at early times might be detected or constrained by GW laser interferometer experiments. Unlike the present work described, however, the back-reaction of the GWs on the expansion rate has been neglected in the aforementioned literature. [5] Finally, we note that the context in which the stiff era appears in the present work as an inevitable consequence of the evolution of the complex scalar field in the ΛSFDM model has no precedent in earlier work.

This paper is organized as follows. In §2.2, we present the basic equations concerning the composition and expansion history of the ΛSFDM model, and the homogeneous evolution

[5] Regarding back-reaction, [124] considered the evolution of a 2-component universe consisting of a stiff component with a constant w and a radiationlike SGWB component, but treated the latter only as a perturbation. [129] also considered the SGWB produced in pre-big-bang models *without* inflation and its back-reaction on the bouncing solutions for such models.

of each component, especially SFDM and the SGWB from inflation. In §2.3, we discuss the solutions to these equations, providing both analytical insights and numerical treatment, especially with regard to the SGWB, and show the holistic expansion history of ΛSFDM from inflation through the present. We also describe our numerical method for a self-consistent account of the SGWB, and show the evolution of several example ΛSFDM models from our numerical calculations, which delineate the evolutionary phases in ΛSFDM and demonstrate a nontrivial contribution from the amplified SGWB from inflation. In §2.4, we then derive the new constraints on the SFDM particle parameters required to satisfy the cosmological observables $z_{\rm eq}$ and $N_{\rm eff}$, and discuss the impact of the SGWB on these constraints, which is dependent on the values of r and $T_{\rm reheat}$. In §2.5, we present one of our most remarkable results: the present-day inflationary SGWB energy density spectrum in the ΛSFDM model is so highly amplified relative to its amplitude in ΛCDM that it may be detectable by the ongoing Advanced LIGO/Virgo (aLIGO/Virgo) experiment. We will show that the expected signal-to-noise ratio (SNR) of this unique SGWB signal can be significant for a wide range of SFDM parameters and reheat temperatures, for currently allowed values of r. The SFDM model can thus be tested for parameters in this range. In fact, we show that the null detection of the SGWB recently reported by the aLIGO O1 run excludes part of the parameter range for an illustrative family of ΛSFDM models, thereby demonstrating that GW detection experiments can already place a new kind of cosmological constraint on SFDM. The accessible range will grow over time as aLIGO/Virgo completes its planned observing runs. Hence, our results provide an additional motivation for LIGO to search for SGWB signals, since this has the potential to probe the nature of dark matter, reheating physics and inflation parameters. In §2.6, we briefly discuss several aspects in which our results in this

paper can be extended in anticipation of future developments of measurements of BBN light-element abundances, and of the space laser interferometer mission LISA. We summarize our conclusions in §2.7. Appendices B.1–B.4 contain some additional materials which we defer from the main text for better readability.

2.2 Basic Equations

2.2.1 The Background universe

As in Paper I, we will consider the background universe to be homogeneous and isotropic on large scales, as described by the spatially-flat Friedmann-Lemaître-Robertson-Walker (FLRW) metric tensor. In this work, we must also consider the perturbations $\delta g_{\mu\nu}$ to this unperturbed FLRW metric $\bar{g}_{\mu\nu}$, corresponding to the tensor modes. In the cosmological "comoving frame" [6], it can be written as

$$\begin{aligned} \mathrm{d}s^2 &\equiv g_{\mu\nu}\mathrm{d}x^\mu \mathrm{d}x^\nu = (\bar{g}_{\mu\nu} + \delta g_{\mu\nu})\mathrm{d}x^\mu \mathrm{d}x^\nu \\ &= c^2\mathrm{d}t^2 - a^2(t)(\delta_{ij} + h_{ij})\mathrm{d}x^i \mathrm{d}x^j, \end{aligned} \tag{2.2}$$

where $a(t)$ is the scale factor, and h_{ij} is a symmetric tensor which characterizes tensor perturbations to the metric, $|h_{ij}| \ll 1$ (weak-field limit). The gauge-invariant h_{ij} satisfies the transverse and traceless conditions (see, e.g., [130]), [7]

$$\partial_i h^{ij} = 0, \quad h_i{}^i = 0, \tag{2.3}$$

where indices of h_{ij} are raised and lowered by the spatial background metric δ_{ij}; $h^{ij} = \delta^{ik}\delta^{jl}h_{kl}$. In this paper, we follow the Einstein summation convention. It is understood that there also be generic small perturbations corresponding to scalar and vector modes as

[6] Rigorously speaking, this reference frame is exactly comoving with cosmic flows only if the universe is perfectly homogeneous and isotropic, i.e., no fluctuations.

[7] If h_{ij} is instead a generic 3-tensor that describes spatial metric perturbations, the conditions in Eq. (2.3) would be regarded as coordinate conditions, known as the transverse-traceless (TT) gauge [131].

well, the growth of which we do not study in this paper. The metric perturbations associated with tensor modes are special, however, in that they also contribute an effective stress-energy tensor $T_{\mu\nu,\,\mathrm{GW}}$ as gravitational waves, as we show in §2.2.1.2 and Appendix B.1.1.

The evolution of the metric of the background universe is governed by the Einstein field equations,

$$R^{\mu}_{\ \nu} - \frac{1}{2}R = \frac{8\pi G}{c^4}T^{\mu}_{\ \nu}, \tag{2.4}$$

where $R^{\mu}_{\ \nu}$ is the Ricci tensor which can be calculated from the metric in Eq. (2.2). The time-time component of the stress-energy tensor, $T^0_{\ 0}$, defines the energy density. For the background universe, it is sufficient to solve only the time-time component of the Einstein field equations, which amounts to the Friedmann equation, plus the energy conservation equations of each component that constitutes the total $T_{\mu\nu}$ of the universe (see [27]). In many cases, the latter can be derived from the equation of motion of the component. Therefore, we will evaluate both sides of the time-time component of Eq. (2.4) and also find the contribution to the total energy density of the universe from each component.

The expansion of the homogeneous FLRW universe is governed by the Friedmann equation, which is derived from the time-time component of the Einstein equations (2.4). For our model,

$$H^2(t) \equiv \left(\frac{\mathrm{d}a/\mathrm{d}t}{a}\right)^2 = \begin{cases} H_{\mathrm{inf}}^2, & a < a_{\mathrm{inf}}, \quad (2.5) \\ H_{\mathrm{inf}}^2 \left(\dfrac{a_{\mathrm{inf}}}{a(t)}\right)^3, & a_{\mathrm{inf}} < a < a_{\mathrm{reheat}}, \quad (2.6) \\ \dfrac{8\pi G}{3c^2}\left[\rho_r(t) + \rho_b(t) + \rho_\Lambda(t) + \rho_{\mathrm{SFDM}}(t) + \rho_{\mathrm{GW}}(t)\right], & a > a_{\mathrm{reheat}}, \quad (2.7) \end{cases}$$

where a_{inf} is the scale factor at the end of inflation when $H(t) = H_{\mathrm{inf}}$, a_{reheat} is the scale factor when reheating ends at $T = T_{\mathrm{reheat}}$, and we have assumed that $w = 0$ during reheating.

In our model, SFDM accounts for all of the cosmological dark matter. Apart from SFDM and gravitational waves, all the other cosmic components are the same than in ΛCDM, i.e. a radiation component ρ_r, baryons ρ_b, and a cosmological constant ρ_Λ (see Eq. [2.7]). The evolution of each component is described in §2.3.

2.2.1.1 Energy density contribution from SFDM

Let us write down the Lagrangian density of the SFDM again,

$$\mathcal{L} = \frac{\hbar^2}{2m} g^{\mu\nu} \partial_\mu \psi^* \partial_\nu \psi - \frac{1}{2} m c^2 |\psi|^2 - \frac{\lambda}{2} |\psi|^4,$$

where the metric $g_{\mu\nu}$ is described in Eq. (2.2) and the definitions of the particle mass m and self-interaction coupling strength λ have been explained in §2.1.3. The field ψ can be written as

$$\psi = |\psi| e^{\mathrm{i}\theta}, \tag{2.8}$$

where $|\psi|$ is its modulus and θ is its phase.

In general, the stress-energy tensor of a field with Lagrangian density $\mathcal{L}$ is given by

$$T_{\mu\nu} = 2 \frac{\delta \mathcal{L}}{\delta g^{\mu\nu}} - g_{\mu\nu} \mathcal{L}. \tag{2.9}$$

Hence, the stress-energy tensor of SFDM can be evaluated as

$$\begin{aligned} T_{\mu\nu,\ \mathrm{SFDM}} = & \frac{\hbar^2}{2m} (\partial_\mu \psi^* \partial_\nu \psi + \partial_\nu \psi^* \partial_\mu \psi) - \\ & - g_{\mu\nu} \left(\frac{\hbar^2}{2m} g^{\rho\sigma} \partial_\rho \psi^* \partial_\sigma \psi - \right. \\ & \left. - \frac{1}{2} m c^2 |\psi|^2 - \frac{\lambda}{2} |\psi|^4 \right). \end{aligned} \tag{2.10}$$

In linear theory with the perturbed FLRW metric (2.2), we have verified that, to the first order, the complex SFDM behaves as a perfect fluid, because $T_{\mu\nu,\ \mathrm{SFDM}}$ can be written in

the following form as for a perfect fluid, characterized by its energy density $\rho_{\rm SFDM}$, isotropic pressure $p_{\rm SFDM}$ and 4-velocity $u^\mu \equiv c(\mathrm{d}x^\mu/\mathrm{d}s)$, with no anisotropic stress,

$$T_{\mu\nu,\ \rm SFDM} = (\rho_{\rm SFDM} + p_{\rm SFDM})u_\mu u_\nu/c^2 - g_{\mu\nu}p_{\rm SFDM}. \tag{2.11}$$

For the homogeneous and isotropic background universe, $u^0 = c$ and $u^i = 0$, and thus, $T_{\mu\nu,\ \rm SFDM}$ becomes diagonal. Its time-time component is recognized as the spatially-averaged energy density of SFDM,

$$\begin{aligned}\rho_{\rm SFDM} \equiv T^0_{\ 0,\ \rm SFDM} &= \frac{\hbar^2}{2mc^2}|\partial_t\psi|^2 + \\ &+\frac{1}{2}mc^2|\psi|^2 + \frac{1}{2}\lambda|\psi|^4 \\ &= \frac{\hbar^2}{2mc^2}\left[|\dot{\psi}|^2 + |\psi|^2\dot{\theta}^2\right] \\ &+\frac{1}{2}mc^2|\psi|^2 + \frac{1}{2}\lambda|\psi|^4,\end{aligned} \tag{2.12}$$

where an "overdot" ($\dot{}$) indicates the derivative with respect to the cosmic time $\mathrm{d}/\mathrm{d}t$, throughout this paper. In the equation above and thereafter, we assume that the complex function ψ always means the spatially-averaged value of the BEC wave function, which adequately accounts for the SFDM contribution to the background universe. The space-space component of $T_{\mu\nu,\ \rm SFDM}$ is recognized as the spatially-averaged pressure,

$$\begin{aligned}p_{\rm SFDM} \equiv -T^i_{\ i,\ \rm SFDM} &= \frac{\hbar^2}{2mc^2}\left[|\dot{\psi}|^2 + |\psi|^2\dot{\theta}^2\right] \\ &-\frac{1}{2}mc^2|\psi|^2 - \frac{1}{2}\lambda|\psi|^4.\end{aligned} \tag{2.13}$$

Hereafter in this paper, $\rho_{\rm SFDM}$ and $p_{\rm SFDM}$ will always refer to the homogeneous part of the energy density and pressure of SFDM, which are only functions of time.

Eqs. (2.12) and (2.13) can also be rearranged into a useful form, in which $\rho_{\rm SFDM}$ and

$p_{\rm SFDM}$ are related to $|\psi|^2$,

$$\rho_{\rm SFDM} = \frac{\hbar^2}{2mc^2}\left(\frac{({\rm d}|\psi|^2/{\rm d}t)^2}{4|\psi|^2} + \frac{(a^3|\psi|^2\dot{\theta})^2}{a^6|\psi|^2}\right) + \frac{1}{2}mc^2|\psi|^2 + \frac{1}{2}\lambda|\psi|^4, \tag{2.14}$$

$$p_{\rm SFDM} = \frac{\hbar^2}{2mc^2}\left(\frac{({\rm d}|\psi|^2/{\rm d}t)^2}{4|\psi|^2} + \frac{(a^3|\psi|^2\dot{\theta})^2}{a^6|\psi|^2}\right) - \frac{1}{2}mc^2|\psi|^2 - \frac{1}{2}\lambda|\psi|^4. \tag{2.15}$$

We note that in the numerator of the 2nd term above, $a^3|\psi|^2\dot{\theta}$ is a conserved quantity as it is proportional to the comoving charge density (see Appendix B in Paper I). In fact,

$$a^3|\psi|^2\dot{\theta} \equiv \frac{mc^2}{\hbar}Q = \rho_{\rm SFDM,0}/\hbar, \tag{2.16}$$

where $\rho_{\rm SFDM,0}$ is the present-day dark matter energy density. The last equality in the equation above expresses the fact that our SFDM today can be treated as nonrelativistic particles. On the other hand, it is shown in Paper I that $\dot{\theta} \cong mc^2/\hbar$ when SFDM is nonrelativistic as "dust-like". Therefore, the number density of SFDM at present, equivalent to the comoving charge density, is given by

$$|\psi|^2\Big|_{a=1} = Q = \rho_{\rm SFDM,0}/mc^2. \tag{2.17}$$

2.2.1.2 Energy density contribution from gravitational waves

As pointed out in [131], gravitational waves, squeezing and stretching the local metric perpendicular to their direction of propagation through space-time, must carry energy. In fact, an (effective) stress-energy tensor of GWs, $T_{\mu\nu,\ {\rm GW}}$, can be defined for small tensor perturbations to the background metric, which is slowly-varying on scales larger than the wavelength, as shown in Appendix B.1.1.

The effective energy density associated with tensor perturbations h_{ij} can be written as follows:

$$\rho_{\rm GW} \equiv T^0{}_{0,\ \rm GW} = \frac{c^2}{64\pi G}\langle \partial_t h_{ij} \partial_t h^{ij} + \frac{c^2}{a^2} \nabla h_{ij} \cdot \nabla h^{ij} \rangle, \tag{2.18}$$

[128] where the brackets $\langle \cdot \rangle$ denote the spatial average over several wavelengths. In particular, this will describe the effect of the SGWB from inflation of interest here. Since primordial fluctuations (including the tensor sector) produced by most inflation models are predicted to be Gaussian, the SGWB can therefore be fully characterized by its power spectrum. As a result, the spatial average $\langle \cdot \rangle$ defined above is equal to the ensemble average. Furthermore, we assume that this ensemble average of tensor fluctuations is unpolarized and isotropic on large scales, according to the standard paradigm of inflation and reheating, as mentioned in §2.1.4. This guarantees that the SGWB produced by inflation is homogeneous on large scales. Hence, applying the Fourier decomposition to h_{ij} (see Appendix B.1.2, Eq. [B.6]), we can write down the (dimensionless) power spectrum of the SGWB, $\Delta_h^2(k,t)$, or the tensor power spectrum, in terms of its mode functions $h_{\mathbf{k}}^P$, as follows:

$$k^3 \langle h_{\mathbf{k}}^P(t) (h_{\mathbf{k}'}^{P'}(t))^* \rangle \equiv 2\pi^2 \Delta_h^2(k,t) \delta_D^{(3)}(\mathbf{k} - \mathbf{k}') \frac{\delta_{PP'}}{4}, \tag{2.19}$$

where $k = |\mathbf{k}|$ is the comoving wavenumber, $P = +, \times$ stands for the two linear polarization states of h_{ij}, $\delta_D^{(3)}$ is the Dirac delta function and $\delta_{PP'}$ denotes the Kronecker delta. As required, $\Delta_h^2(k,t)$ does not depend on the direction of the comoving wave vector $\mathbf{k}$ nor the polarization state P, but only on the magnitude $k = |\mathbf{k}|$, capturing all statistical properties of the stochastic metric perturbation h_{ij}.[8] Inserting Eq. (2.19) and Eq. (B.6) into Eq. (2.18)

[8]Strictly speaking, to ensure that the tensor power spectrum is only a function of the wavenumber k at any time t, we also need to investigate the evolution of h_{ij} via its equation of motion, which is explained in §2.2.3.

yields

$$\rho_{\rm GW}(t) = \frac{c^2}{64\pi G}\int_0^\infty {\rm d}\ln k \left(\left| \frac{\dot{h}^P_{\mathbf{k}}(t)}{h^P_{\mathbf{k}}(t)} \right|^2 \Delta^2_h(k,t) + \frac{k^2c^2}{a^2(t)}\Delta^2_h(k,t) \right), \tag{2.20}$$

where the term $|\dot{h}^P_{\mathbf{k}}(t)/h^P_{\mathbf{k}}(t)|^2$ has been extracted out of the ensemble average $\langle\cdot\rangle$, because it is deterministic, governed by the equation of motion of $h^P_{\mathbf{k}}(t)$, which we will show in §2.2.3. There we will also explain why $|\dot{h}^P_{\mathbf{k}}(t)/h^P_{\mathbf{k}}(t)|^2$ does not depend on P, i.e., P can be either $+$ or $\times$. As expected, Eq. (2.20) shows that $\rho_{\rm GW}(t)$ is homogeneous in space, since it does not depend on position $\mathbf{x}$.

It is useful to define the differential SGWB energy density per logarithmic k as

$$\frac{{\rm d}\rho_{\rm GW}}{{\rm d}\ln k}(k,t) = \frac{c^2}{64\pi G}\left(\left| \frac{\dot{h}^P_{\mathbf{k}}(t)}{h^P_{\mathbf{k}}(t)} \right|^2 + \frac{k^2c^2}{a^2(t)} \right) \Delta^2_h(k,t). \tag{2.21}$$

2.2.2 Equation of motion: scalar field dark matter

The equation of motion for SFDM is the Klein-Gordon equation. For a homogeneous scalar field, it is written as

$$\frac{\hbar^2}{2mc^2}\ddot{\psi} + 3\frac{\hbar^2}{2mc^2}\frac{\dot{a}}{a}\dot{\psi} + \frac{1}{2}mc^2\psi + \lambda|\psi|^2\psi = 0, \tag{2.22}$$

in terms of the BEC wave function $\psi(t)$. It can be transformed into an equivalent form, namely, the energy conservation equation, in terms of the energy density $\rho_{\rm SFDM}$ and the corresponding pressure, $p_{\rm SFDM}$, as follows:

$$\dot{\rho}_{\rm SFDM} + 3\frac{\dot{a}}{a}(\rho_{\rm SFDM} + p_{\rm SFDM}) = 0. \tag{2.23}$$

The Klein-Gordon equation (2.22) can be rearranged into the following form,

$$\frac{\hbar^2}{2mc^2}\left(\frac{\mathrm{d}^2|\psi|^2}{\mathrm{d}t^2}-\frac{(\mathrm{d}|\psi|^2/\mathrm{d}t)^2}{2|\psi|^2}\right)+\frac{\hbar^2}{2mc^2}\frac{3\dot{a}}{a}\frac{\mathrm{d}|\psi|^2}{\mathrm{d}t}-\frac{\hbar^2}{mc^2}\frac{(\rho_{\mathrm{SFDM},0}/\hbar)^2}{a^6|\psi|^2}+mc^2|\psi|^2+2\lambda|\psi|^4=0, \tag{2.24}$$

where we have made use of Eq. (2.16), replacing $a^3|\psi|^2\dot{\theta}$ by $\rho_{\mathrm{SFDM},0}/\hbar$. In Eq. (2.24), the dependent variable is essentially $|\psi|^2$, rather than ψ. We will see later in §2.3.4.1 that it is this equation that we solve numerically to obtain the early phase of the evolution of SFDM.

2.2.3 Equation of motion: tensor perturbations

In the absence of anisotropic stresses,[9] the Einstein equation for tensor perturbations h_{ij} in a spatially flat FLRW universe with scale factor a reads

$$\partial_t^2 h_{ij}(\mathbf{x},t)+3\frac{\dot{a}(t)}{a(t)}\partial_t h_{ij}(\mathbf{x},t)-\frac{c^2}{a^2(t)}\nabla^2 h_{ij}(\mathbf{x},t)=0. \tag{2.25}$$

The equation above is essentially a cosmological wave equation, its corresponding solutions are thus gravitational waves. In fact, the wave nature can be more directly manifested by rewriting the equation of motion above, Eq. (2.25), in terms of Fourier mode functions $h_{\mathbf{k}}^P(t)$ (and their conjugate $(h_{\mathbf{k}}^P(t))^*$, see Eq. [B.6] for their definition),

$$\ddot{h}_{\mathbf{k}}^P(t)+3\frac{\dot{a}(t)}{a(t)}\dot{h}_{\mathbf{k}}^P(t)+\frac{k^2c^2}{a^2(t)}h_{\mathbf{k}}^P(t)=0. \tag{2.26}$$

The equation above manifestly shows that the equation of motion for tensor perturbations only involves the magnitude $k=|\mathbf{k}|$ of the wave vector, not its direction nor the polarization state $P=+$ or $\times$. Therefore, as long as the initial condition for tensor perturbations is

[9] Actually, the presence of free-streaming relativistic neutrinos has been shown by [132] to contribute anisotropic stress which modifies Eq. (2.25). The correction which results can be treated by a post-facto multiplicative factor which does not depend on wavenumber k, as described in [133].

isotropic and unpolarized, so will they always be at any time throughout their evolution. This completes our justification to treat $\Delta_h^2(k,t)$ only as a function of k at any time t. With no loss of generality, we can thereby assume $h_{\mathbf{k}}^{+}(t) = h_{\mathbf{k}}^{\times}(t) \equiv h_k(t)$ and henceforth treat $h_k(t)$ only.

If we neglect the cosmological expansion (i.e., set $\dot{a} = 0$) in Eq. (2.26), then its solutions are simply traveling plane waves with the dispersion relation $\omega_k = kc$. Therefore, on time scales much less than a Hubble time, tensor modes are plane waves propagating at the speed of light, just like the GWs detected recently by the Advanced LIGO experiment, sourced by binary black hole merger events [134]. GWs are also known as gravitational radiation, or radiative degrees of freedom [135].

It is convenient to express Eq. (2.26) with respect to the conformal time (length), $\tau = c\int dt/a(t)$, leading to an equation for $h_k(\tau)$,

$$h_k''(\tau) + 2\frac{a'(\tau)}{a(\tau)}h_k'(\tau) + k^2 h_k(\tau) = 0, \tag{2.27}$$

where the prime denotes the derivative with respect to conformal time $' \equiv d/d\tau$. We will discuss the evolution of gravitational waves, and some analytical solutions, in §2.3.2.

2.3 Evolution in the ΛSFDM universe

In Paper I, we considered a universe with the same cosmic inventory as the basic ΛCDM model except that CDM is replaced by SFDM, the ΛSFDM model, since the late-time evolution of the ΛSFDM universe is indistinguishable from that of standard ΛCDM after $z_{\rm eq}$, except for small-scale structure. We used the set of cosmological parameters from the Planck 2013 data release [7]. In this work, we will add to ΛSFDM the contribution due to

$\rho_{\rm GW}$, as it is currently constrained by upper bounds. Also, we use the updated 2015 Planck data to solve for the evolution of this homogeneous background universe [75]. A summary of the parameters we use can be found in Table 2.1. The fractional energy densities are defined via $\Omega_i(t) \equiv \rho_i(t)/\rho_{\rm crit}(t)$ with the critical energy density of the universe at time t,

$$\rho_{\rm crit}(t) = \frac{3H^2(t)c^2}{8\pi G}. \tag{2.28}$$

Hereafter in this paper, unless otherwise noted as fluctuations, all physical quantities in space will refer to their spatially homogeneous, isotropic part, i.e., only functions of time.

First, we discuss the evolution of each of the cosmic components separately in §2.3.1–§2.3.3, highlighting certain heuristic aspects. We then put them altogether in §2.3.4 to derive the expansion history of the entire background ΛSFDM universe. In Paper I, we took the point of view that, since the cosmological parameters are known at the present (e.g., from CMB measurements), our solutions of the coupled Klein-Gordon and Friedmann equations must match this late-time universe. In particular, the observed dark matter energy density at late times, when the SFDM is nonrelativistic (dust-like), sets the value of the conserved comoving charge density Q, which in turn sets the amplitude of the field $|\psi|$ at the present (see Eq. [2.17]). This field value combines with the observed Hubble constant and energy densities of the other components in Table 2.1 to make the boundary conditions for the coupled evolution equations. In Paper I, these B.C.'s were satisfied by integrating backward in time from the present. The results were checked against a forward time-integration. Here, however, unlike in Paper I, the evolution is affected by $\Omega_{\rm GW}$, too, which must be included self-consistently in a forward time-integration which starts from the end of inflation, whose energy scale is set by our choice of r. As a result, a more elaborate scheme is required than

in Paper I. In this paper, we only use backward integration to produce a guess for the initial conditions of the forward integration, and then converge on the final solution by an iterative scheme involving both forward and backward integrations. We present the details of the numerical method in §2.3.4.1 below.

h	0.6781	$\Omega_m h^2$	0.141
$\Omega_b h^2$	0.02226	$\Omega_r h^2$	4.184×10^{-5}
$\Omega_c h^2$	0.1186	$z_{\rm eq}$	3365
$T_{\rm CMB}$/K	2.7255	Ω_Λ	0.694
$10^9 A_s$	2.139	$r_{0.05}$	$< 0.07 \quad (95\%)$

Table 2.1: Cosmological parameters. All values except $r_{0.05}$ are quoted from the Planck 2015 results: central values of the 68% confidence intervals for the base ΛCDM model with TT+LowP+Lensing data, see Table 4 in [75]. The upper bound of $r_{0.05}$ at the pivot scale $k_* = 0.05$ Mpc^{-1} at 95% confidence is quoted from the latest result of the BICEP2/Keck Array CMB polarization experiment [114].

2.3.1 Evolution of SFDM

In our model, DM is entirely made up of SFDM, i.e. $\Omega_c h^2$ in Table 2.1 will be taken to refer to the present-day SFDM energy density, instead of CDM. The discussion in this subsection follows largely the one in Paper I, but since it is of central importance to our model, we want to repeat some of it here for the sake of the reader.

One basic behavior of a scalar field is that it oscillates over time, characterized by its changes in phase θ. The oscillation angular frequency is defined as $\omega \equiv \dot{\theta}$. SFDM behaves differently, depending on whether ω predominates over the expansion rate H or not (oscillation/spin vs roll). As a result, SFDM passes through certain limit cases as it

evolves, in which its EOS is simply barotropic, as we have shown in Paper I. At early times the expansion is much faster than the field oscillation ($\omega/H \ll 1$). Eventually, however, the expansion rate declines faster than the oscillation frequency and the inequality reverses ($\omega/H \gg 1$).

2.3.1.1 Scalar field oscillation faster than Hubble expansion ($\omega/H \gg 1$)

Once the expansion rate drops below the (angular) oscillation frequency of the field, the oscillation frequency can be derived as (see Paper I)

$$\omega = \frac{mc^2}{\hbar}\sqrt{1+\frac{2\lambda}{mc^2}|\psi|^2}. \tag{2.29}$$

In this regime, the exact calculation of the cosmological time evolution of the scalar field is numerically prohibitive, since the necessary time step is too small ($\propto 1/\omega$). Instead, it has been customary in the literature to follow the evolution of the time-averaged values of ρ and p over several oscillation cycles of the field. In this subsection §2.3.1, we omit the subscript "SFDM" in ρ and p for brevity. Multiplying the field equation (2.22) by ψ^* and then averaging over a time interval that is much longer than the field oscillation period, but much shorter than the Hubble time, results in (see also [61, 59])

$$\frac{\hbar^2}{2mc^2}\langle|\mathrm{d}\psi/\mathrm{d}t|^2\rangle \cong \frac{1}{2}mc^2\langle|\psi|^2\rangle + \lambda\langle|\psi|^4\rangle. \tag{2.30}$$

Combining this relation with the expressions for energy density (2.12) and pressure (2.13) yields,

$$\begin{aligned}\langle\rho\rangle &= mc^2\langle|\psi|^2\rangle + \frac{3}{2}\lambda\langle|\psi|^4\rangle \\ &\approx mc^2\langle|\psi|^2\rangle + \frac{3}{2}\lambda\langle|\psi|^2\rangle^2, \qquad (2.31)\\ \langle p\rangle &= \frac{1}{2}\lambda\langle|\psi|^4\rangle \approx \frac{1}{2}\lambda\langle|\psi|^2\rangle^2. \qquad (2.32)\end{aligned}$$

In this regime, we take $\rho = \langle\rho\rangle$ and $p = \langle p\rangle$. The equation of state is then approximately

$$p = \frac{m^2c^4}{18\lambda}\left(\sqrt{1+\frac{6\lambda\rho}{m^2c^4}}-1\right)^2, \tag{2.33}$$

or equivalently,

$$w \equiv \frac{p}{\rho} = \frac{1}{3}\left[\frac{1}{1+\frac{2mc^2}{3\lambda\langle|\psi|^2\rangle}}\right] \tag{2.34}$$

(see also [63, 62]). This is referred to as the fast-oscillation approximation in Paper I. We call this regime the *fast-oscillation regime*, and, henceforth, drop the $\langle\rangle$'s around ρ and p in what follows. It encompasses two evolutionary phases of SFDM, as follows:

(1) CDM-like (or "dust"-like) phase: non-relativistic ($w = 0$)

As the universe expands, the dark matter energy density will continuously decrease to the point when the rest-mass energy density dominates the total SFDM energy density, i.e., $\frac{3}{2}\lambda\langle|\psi|^2\rangle^2 \ll mc^2\langle|\psi|^2\rangle$. In this limit, equation (2.33) reduces to

$$p \approx \frac{\lambda}{2m^2c^4}\rho^2 \approx 0, \tag{2.35}$$

thus SFDM behaves like non-relativistic dust. Its self-interaction is weak, so that on large scales SFDM is virtually collisionless. Therefore, it evolves like CDM, following the familiar relation,

$$\rho \propto a^{-3}. \tag{2.36}$$

Then, the field amplitude decays as $|\psi| \propto a^{-3/2}$ and the scale factor goes as $a \sim t^{2/3}$.

(2) Radiationlike phase: relativistic ($w = 1/3$)

At some point early enough, SFDM will be so dense that the quartic term in the energy density (2.31), the self-interaction energy, dominates, i.e., $\frac{3}{2}\lambda\langle|\psi|^2\rangle^2 \gg mc^2\langle|\psi|^2\rangle$. In this limit, equation (2.33) reduces to

$$p \approx \frac{1}{3}\rho \approx \frac{1}{2}\lambda\langle|\psi|^2\rangle^2, \tag{2.37}$$

and SFDM behaves like radiation. The time evolution is accordingly

$$\rho \propto a^{-4}, \tag{2.38}$$

while the field amplitude decays as $|\psi| \propto a^{-2}$ with the scale factor $a \sim t^{1/2}$.

It is important to note that SFDM without self-interaction, i.e., when $\lambda = 0$, does *not* undergo this radiationlike phase.

2.3.1.2 Scalar field oscillation slower than Hubble expansion ($\omega/H \ll 1$)

At earlier times, the Hubble parameter *exceeded* the oscillation frequency. In this early regime, the fast oscillation approximation above is not valid, so there is no closed-form expression for the EOS. In this *slow-oscillation regime*, one has to solve the rearranged Klein-Gordon equation (2.24) exactly, coupled with the Friedmann equations (2.7). Nonetheless, one can still find a heuristic qualitative description, as follows:

(1) Stiff phase: relativistic limit ($w = 1$)

At sufficiently early times, the expansion rate is much greater than the oscillation frequency, $\omega/H \ll 1$. The energy density and pressure are both dominated by the

kinetic term of (2.12) and (2.13). Therefore,

$$p \approx \rho \approx \frac{\hbar^2}{2mc^2}|\partial_t \psi|^2. \tag{2.39}$$

This stiff EOS implies that the sound speed almost reaches the speed of light, the maximal possible value (this is formally analoguous to the incompressible fluid in Newtonian gas dynamics, where the sound speed is infinity). In this case,

$$\rho \propto a^{-6}, \tag{2.40}$$

and it can be shown that $\partial_t \psi \propto a^{-3}$, and hence $\psi \propto \log a$, where $a \sim t^{1/3}$. An important implication immediately follows from relation (2.40) that, as we go back in time approaching the Big Bang ($a \to 0$), the energy density of SFDM should dominate the total energy density of the universe, because it increases faster than that of radiation and of any other component. Therefore, we predict an early era of stiff-SFDM-domination in a ΛSFDM universe, which will be demonstrated in §2.3.4.

2.3.2 Tensor fluctuations from inflation and the SGWB

In this subsection, we describe the evolution and implementation of our calculation of the SGWB. To anticipate our full numerical treatment presented in §2.3.4, in which we solve the coupled equations for the SGWB, the SFDM, the standard cosmic components and the expansion rate of the background universe, it will be instructive to show some analytical results first, for the simpler case of constant w (the EOS parameter of the universe). For this purpose, we must derive the energy density contributed by the SGWB, for which we will first need to derive the evolution of the tensor metric perturbations, by solving their equation of motion presented in §2.2.3 along with the initial condition posed in §2.3.2.1 below. As

we shall see, there are two limits in which this evolution is simplified for a given mode of comoving wavenumber k, in terms of its wavelength ($\propto k^{-1}$) relative to the horizon. It will be sufficient to represent the evolution at all times by stitching these two limits together, in what is known as the *thin-horizon approximation*. With this solution, we will have both the spectrum of the primordial tensor perturbations and of their associated energy density as a function of time.

2.3.2.1 Primordial amplitude

The equation of motion for the tensor modes $h_k(\tau)$ in Eq. (2.27) requires an initial condition. For our purpose, the initial amplitude of $h_k(\tau)$ is given by the primordial tensor amplitude produced by inflation. During slow-roll inflation, in which the Hubble constant $H(a)$ is slowly varing, fluctuations are exponentially stretched in space, so that for many modes, their proper wavelengths, $2\pi a/k$, will become larger than the Hubble radius $c/H(a)$ (or the horizon). In other words, these modes exit the horizon during inflation. Once a mode is far outside the horizon, the amplitude (of its growing mode) is conserved ("frozen") throughout its superhorizon evolution [27], even after inflation ends. Therefore, we will begin our integration of Eq. (2.27) for a given mode k when it is far outside the horizon (i.e., $kc \ll aH(a)$) and its initial amplitude, $h_{k,\ \mathrm{init}}$, is given by this superhorizon value. Modes of interest are all far outside the horizon by the end of inflation at $a = a_{\mathrm{inf}}$, so $h_k(a_{\mathrm{inf}}) = h_{k,\ \mathrm{init}}$ for these modes.

These modes will later reenter the horizon at different cosmic times according to their wavelength, while the EOS of the background universe evolves through different cosmic eras. On the other hand, modes reentering during different eras do not know of each other, which

means that each mode inherits the memory of its own superhorizon amplitude $h_{k,\ \mathrm{init}}$ with which it started out, at its respective reentry point a_k.[10] Hereafter in this paper, unless otherwise noted, we will use a_k and $H_k \equiv H(a_k)$ to indicate those quantities at the horizon reentry for mode k, $kc = a_k H_k$. [11]

Note that this initial amplitude $h_{k,\ \mathrm{init}}$ is not unique, because of the stochastic nature of the primordial tensor fluctuations produced by inflation. However, this does not prevent us from evaluating $\rho_{\mathrm{GW}}(\tau)$, the mean energy density of the inflationary SGWB, in Eq. (2.20), because the stochasticity in h_k is fully accounted for by the tensor power spectrum $\Delta_h^2(k,\tau)$ defined in Eq. (2.19). In fact, we only need to know the primordial tensor power spectrum, $\Delta^2_{h,\ \mathrm{init}}(k) \equiv \Delta_h^2(k, a_{\mathrm{inf}})$, evaluated at a_{inf} for all modes of interest. The evolution of $\Delta_h^2(k,\tau)$, or equivalently, $h_k(\tau)$, at any time later is deterministic, separable from its stochastic initial condition. We can define the tensor transfer function $T_h(k,\tau)$, which encodes this deterministic evolution, as

$$T_h(k,\tau) \equiv \left| \frac{h_k(\tau)}{h_{k,\ \mathrm{init}}} \right|^2 = \frac{\Delta_h^2(k,\tau)}{\Delta^2_{h,\ \mathrm{init}}(k)}, \tag{2.41}$$

the solution of which we will show in §2.3.2.2.

The primordial power spectrum of tensor fluctuations generated during inflation, $\Delta^2_{h,\ \mathrm{init}}(k)$, is predicted to be nearly scale-invariant, if inflation is driven by a single slow-

[10] There are also modes at the low-k end, whose comoving wavelengths are even larger than the present-day horizon size. Hence, they will never reenter the horizon as the universe has already been in the Λ-dominated era. We do not study these modes in this paper.

[11] It is customary to describe a tensor mode of comoving wavenumber k as "reentering the horizon" when $k = aH/c$. We follow that convention here. However, this actually corresponds to the time when the comoving wavelength of the mode equals the comoving Hubble radius $c/a(t)H(t)$, not the particle horizon $c\int \mathrm{d}t/a(t)$. When the effective EOS of the universe is $w = -1$, for example, the comoving Hubble radius shrinks, while the particle horizon always grows.

rolling scalar field. It can be parametrized by a power law,

$$\Delta^2_{h,\ \mathrm{init}}(k) = A_t(k/k_*)^{n_t} \equiv rA_s(k/k_*)^{n_t}, \tag{2.42}$$

where A_t (A_s) is the tensor (scalar) amplitude, and the pivot scale $k_* = 0.05\ \mathrm{Mpc}^{-1}$, following the 2015 Planck data convention [75]. The value of A_s and the latest upper bound of $r = r_{0.05}$ is given in Table 2.1. The tensor spectral index n_t is related to the tensor-to-scalar ratio r by

$$n_t = -r/8, \tag{2.43}$$

which is known as the consistency relation. In this paper, we will presume that this relation is valid.

2.3.2.2 Analytical solutions for tensor metric perturbations in the subhorizon limit

Closed-form solutions of Eq. (2.27) for $h_k(\tau)$ exist, if a and the conformal time τ are related via a powerlaw,

$$\frac{a}{a_0} = \left(\frac{\tau}{\tau_0}\right)^{\alpha}, \tag{2.44}$$

where the exponent α depends on the EOS parameter w of the universe, according to

$$\alpha = \frac{2}{1+3w}. \tag{2.45}$$

In our case, however, w changes with time, so we cannot adopt Eq. (2.44) in general. Fortunately, when a mode is well outside the horizon, h_k is independent of time and of the change in w. Furthermore, as long as there are eras of the background expansion history in which w is relatively constant, i.e., in each of these eras Eq. (2.44) can be applied with a

respective constant α over a range of τ, we can insert this relation into Eq. (2.27), to obtain an analytical solution for the evolution of $h_k(\tau)$ during these eras.

Particularly, if a mode k reenters the horizon in such an era with a constant α, and later becomes deep within the horizon (i.e., $k \gg aH/c$, or $k\tau \gg \alpha$) while still in the same era, one can show that in this subhorizon limit the solution for $h_k(\tau)$, in the eras of interest to us, respectively reads as

- reheating and matter-dominated era: $w = 0, \alpha = 2$

$$h_{k,\ \mathrm{m}}(\tau) \simeq h_{k,\ \mathrm{init}} \Gamma\left(\frac{5}{2}\right) \frac{4}{\sqrt{\pi}} \frac{\cos(k\tau - \pi)}{(k\tau)^2} \quad \text{for } k\tau \gg 2, \tag{2.46}$$

- stiff-SFDM-dominated era: $w = 1, \alpha = \frac{1}{2}$

$$h_{k,\ \mathrm{stiff}}(\tau) \simeq h_{k,\ \mathrm{init}} \sqrt{\frac{2}{\pi}} \frac{\cos(k\tau - \pi/4)}{(k\tau)^{1/2}} \quad \text{for } k\tau \gg \frac{1}{2}, \tag{2.47}$$

- radiation-dominated era: $w = \frac{1}{3}, \alpha = 1$

$$h_{k,\ \mathrm{rad}}(\tau) \simeq h_{k,\ \mathrm{init}} \Gamma\left(\frac{3}{2}\right) \frac{4}{\sqrt{\pi}} \frac{\cos(k\tau - \pi/2)}{k\tau} \quad \text{for } k\tau \gg 1. \tag{2.48}$$

Thus, the initial (superhorizon) amplitude from inflation, $h_{k,\ \mathrm{init}}$, suffers decay upon horizon reentry, according to those expressions. In terms of the tensor transfer function $T_h(k, \tau)$ defined in Eq. (2.41), we can see that, in the respective eras considered above,

$$T_h^{\mathrm{m}}(k, \tau) = \Gamma^2\left(\frac{5}{2}\right) \frac{16}{\pi} \frac{\cos^2(k\tau - \pi)}{(k\tau)^4}, \tag{2.49}$$

$$T_h^{\mathrm{stiff}}(k, \tau) = \frac{2}{\pi} \frac{\cos^2(k\tau - \pi/4)}{k\tau}, \tag{2.50}$$

and

$$T_h^{\rm rad}(k,\tau) = \Gamma^2\left(\frac{3}{2}\right)\frac{16}{\pi}\frac{\cos^2(k\tau-\pi/2)}{(k\tau)^2}. \tag{2.51}$$

Indeed, it can be shown that the tensor transfer function in the subhorizon limit for general α reads as

$$\begin{aligned} T_h(k,\tau) &= \frac{\Gamma^2(\alpha_k+\frac{1}{2})}{\pi}\left(\frac{2}{k\tau}\right)^{2\alpha_k}\cos^2(k\tau-\alpha_k\pi/2) \\ &\simeq \frac{1}{2}\left(\frac{a_k}{a}\right)^2\frac{\Gamma^2(\alpha_k+\frac{1}{2})}{\pi}\left(\frac{2}{\alpha_k}\right)^{2\alpha_k} \end{aligned} \tag{2.52}$$

(compare also to [128]), where a_k is the scale factor at which the mode k reenters the horizon, $a_k = kc/H_k$, and we averaged over $\cos^2(..)$ to arrive at the second line. The era-dependent parameter $\alpha_k = 2/(1+3w(a_k))$ should be evaluated at horizon reentry for each mode k as well. We note that in the second line of Eq. (2.52), the explicit time variable is a rather than τ. Therefore, this expression for the tensor transfer function $T_h(k,a)$ as a function of a, can be applied at any later time in the subhorizon limit for a given k, regardless of any later change in the EOS parameter w of the background universe.

The factor $\frac{1}{2}(a_k/a)^2$ in Eq. (2.52) will simply lead to the well-known behavior that for a given k, $\mathrm{d}\rho_{\rm GW}/\mathrm{d}\ln k$ (see Eq. [2.21]) will decay like radiation ($\propto a^{-4}$) after the mode reenters the horizon (called "redshift-suppression" factor C_1 in [128]), while the remaining factors make sure that the correct subhorizon limit is retrieved when matching the solution at horizon crossing to the superhorizon limit (called "horizon-crossing" factor C_2 in [128]).

There is an additional multiplicative factor which takes account of the effects of anisotropy due to neutrino free streaming (as described in [132, 133]). When relativistic neutrinos are important during the radiation-dominated era, they can damp the tensor fluctuations $h_k(\tau)$ by a multiplicative factor $A \sim 0.8$. This multiplicative factor is *not* included

in the analytical solutions above (e.g., Eq. [2.52] for the tensor transfer function), but will be included later in our numerical solutions (this effect was called "anisotropy factor" C_3 in [128]).

2.3.2.3 Evaluating $\Omega_{\rm GW}$

The energy density fraction of the SGWB, $\Omega_{\rm GW}(a) \equiv 8\pi G\rho_{\rm GW}(a)/3H^2(a)c^2$, is calculated by integrating Eq. (2.21) over all modes of interest, divided by $\rho_{\rm crit}(a)$,

$$\begin{aligned}\Omega_{\rm GW}(k,a) \equiv \frac{{\rm d}\Omega_{\rm GW}(a)}{{\rm d}\ln k} &= \frac{1}{\rho_{\rm crit}(a)}\frac{{\rm d}\rho_{\rm GW}(a)}{{\rm d}\ln k} \\ &= \frac{\Delta_h^2(k,a)c^2}{24a^2H^2(a)}\left(\left|\frac{h_k'(a(\tau))}{h_k(a(\tau))}\right|^2 + k^2\right). \end{aligned} \tag{2.53}$$

This form is written in a way that makes apparent the contribution from superhorizon evolution, i.e., the second term in Eq. (2.53). In the subhorizon limit, the two terms are equal, as $|h_k'(a(\tau))|^2 \cong k^2|h_k(a(\tau))|^2$. This can be shown by neglecting the Hubble friction term ($\propto a'/a$) in the wave equation (2.27). In the superhorizon limit, on the other hand, only the second term remains, since $h_k'(a(\tau)) \cong 0$. There remains uncertainty in whether superhorizon modes physically contribute an average stress-energy that can affect the background metric of the universe. However, this contribution, should it exist, is negligible compared to subhorizon modes anyway, as we have confirmed in this work.

1. **Subhorizon limit:**
   In the subhorizon limit $k \gg aH/c$, the energy density spectrum of GWs, $\Omega_{\rm GW}(k,a)$, can be calculated by solving the linear evolution equation (2.27). For modes which reenter the horizon when the universe has a fixed EOS, $\Omega_{\rm GW}(k,a)$, defined above in Eq. (2.53), is related to the tensor transfer function defined in Eq. (2.41), as follows:

$$\begin{aligned}\Omega_{\rm GW}(k,a) &= \frac{\Delta_h^2(k,a)}{12}\left(\frac{kc}{aH}\right)^2 \\ &= \frac{\Delta_{h,\ {\rm init}}^2(k)}{12}\left(\frac{kc}{aH}\right)^2 T_h(k,a). \end{aligned} \tag{2.54}$$

The expressions for $\Omega_{\rm GW}(k, a(\tau))$ which correspond to the above analytical solutions in Eqs. (2.49-2.51), after averaging over $\cos^2(..)$, are given by

$$\Omega^{\rm m}_{\rm GW}(k,\tau) \simeq \frac{\Delta^2_{h,\ {\rm init}}(k)}{24} \cdot \frac{9}{4} \frac{1}{(k\tau)^2}, \tag{2.55}$$

$$\Omega^{\rm stiff}_{\rm GW}(k,\tau) \simeq \frac{\Delta^2_{h,\ {\rm init}}(k)}{24} \cdot \frac{8}{\pi} k\tau, \tag{2.56}$$

$$\Omega^{\rm rad}_{\rm GW}(k,\tau) \simeq \frac{\Delta^2_{h,\ {\rm init}}(k)}{24}. \tag{2.57}$$

For $\Delta^2_{h,\ {\rm init}}(k) \simeq k^0$, this yields the k-dependence of $\Omega_{\rm GW}(k,\tau)$ for a matter-, stiff-SFDM-, or radiation-dominated universe as follows: $\Omega^{\rm m}_{\rm GW}(k,\tau) \propto k^{-2}$, $\Omega^{\rm stiff}_{\rm GW}(k,\tau) \propto k$, and $\Omega^{\rm rad}_{\rm GW}(k,\tau) \propto k^0$, respectively. This dependence on k will be reflected in our prediction of the SGWB energy density spectrum at the present in §2.5.

We can now illustrate the effect of the amplification of the (differential) GW energy density of a certain mode with wavenumber k which reenters the horizon during the stiff phase, compared to that if the mode reenters the horizon during the radiation-dominated era, as in a standard ΛCDM universe. In fact, combining Eq. (2.42), Eq. (2.52) and Eq. (2.54) yields

$$\Omega_{\rm GW}(k,a) \simeq \frac{rA_s}{24} \left(\frac{ck}{aH}\right)^2 \left(\frac{a_k}{a}\right)^2, \tag{2.58}$$

where we have, for simplicity, neglected the dependence on n_t in Eq. (2.42) and ignored the factor $\frac{\Gamma^2(\alpha+\frac{1}{2})}{\pi} \left(\frac{2}{\alpha}\right)^{2\alpha}$ in Eq. (2.52). In this equation above, the scale factor a is at a late time when the expansion histories of the two scenarios, ΛSFDM vs. ΛCDM, converge, so that the Hubble parameter $H = H(a)$ is the same for both. Therefore, the

only uncommon factor in Eq. (2.58) is a_k for the two scenarios. In a ΛSFDM universe, suppose now that the stiff era ends and the universe becomes radiation-dominated at $a_{\rm rad}$. The Hubble constant $H_{\rm rad}$ at that time must be approximately the same as that in the ΛCDM scenario, since the evolution of the two universes from that point on up to the present must be the same. From the evolution of the homogenous background universe we have

$$\left(\frac{H_{k,\rm stiff}}{H_{\rm rad}}\right)^2 = \left(\frac{a_{k,\rm stiff}}{a_{\rm rad}}\right)^{-6}, \tag{2.59}$$

and

$$\left(\frac{H_{k,\rm rad}}{H_{\rm rad}}\right)^2 = \left(\frac{a_{k,\rm rad}}{a_{\rm rad}}\right)^{-4}, \tag{2.60}$$

where $a_{k,i}$ ($i = \rm stiff, rad$) is the scale factor at which the mode k reenters the horizon, for each scenario, and $H_{k,i}$ is the corresponding Hubble constant. Therefore,

$$\frac{H_{k,\rm stiff}}{H_{k,\rm rad}} = \frac{a_{k,\rm stiff}^{-3} a_{\rm rad}}{a_{k,\rm rad}^{-2}}. \tag{2.61}$$

Taking into account the fact that $ck = a_{k,\rm stiff} H_{k,\rm stiff} = a_{k,\rm rad} H_{k,\rm rad}$, we rearrange the equation above and obtain

$$a_{k,\rm rad} = \left(\frac{a_{k,\rm stiff}}{a_{\rm rad}}\right) a_{k,\rm stiff}. \tag{2.62}$$

Since $a_{k,\rm stiff}/a_{\rm rad} < 1$, from the equation above $a_{k,\rm stiff} > a_{k,\rm rad}$. The mode reenters the horizon later (i.e. at a larger scale factor) during the stiff phase than it would during a radiation-dominated universe. Thus, according to Eq. (2.58) we conclude that a mode that reenters the horizon during the stiff era will contribute a higher GW energy density at late times than it would in the standard scenario, when that mode reenters in the radiation-dominated era.

To view this effect from another perspective, there are two competing factors which combine to make the contribution of a given mode to the GW energy density of the universe bigger in the presence of the stiff phase, as follows. Whatever the initial GW energy density upon horizon reentry at a_k is, thereafter it dilutes like radiation, in proportion to $(a_k/a)^4$. Since $a_{k,\mathrm{stiff}} > a_{k,\mathrm{rad}}$, there is less dilution to a given late time for the ΛSFDM case with a stiff phase. On the other hand, the superhorizon tensor amplitude is the same in both cases, since we consider the same inflationary model. Therefore, the GW contribution of a mode expressed as a fraction of the critical density at horizon reentry (see Eq. [2.58]) is also the same. Since this critical density is proportional to $H_k^2 = c^2k^2/a_k^2$, it is, however, smaller in ΛSFDM than in ΛCDM. This effect makes the contribution to ρ_{GW} at horizon reentry smaller for ΛSFDM than for ΛCDM. To elucidate both of the effects, we can rewrite Eq. (2.58) in the following way:

$$\begin{aligned}\Omega_{\mathrm{GW}}(k,a) &= \frac{rA_s}{24}\frac{H_k^2}{H^2}\left(\frac{a_k}{a}\right)^4 \\ &= \left.\frac{\mathrm{d}\rho_{\mathrm{GW}}}{\mathrm{d}\ln k}\right|_{a=a_k}\left(\frac{a_k}{a}\right)^4\frac{1}{\rho_{\mathrm{crit}}(a)}.\end{aligned} \tag{2.63}$$

While a tensor mode reenters the horizon with a lower energy density when it reenters during the stiff phase of a ΛSFDM universe, since $H_{k,\mathrm{stiff}} < H_{k,\mathrm{rad}}$, however, according to Eq.(2.63), it reenters at a later scale factor. Hence, its radiationlike energy density does not thereafter dilute so much as in ΛCDM, since $(a_{k,\mathrm{stiff}}/a)^4 > (a_{k,\mathrm{rad}}/a)^4$. Overall, the latter effect wins, and, therefore, there is a boost in the GW energy density for a mode that reenters the horizon during the stiff-SFDM-dominated era (predicted in §2.3.1.2), relative to what it would have been in ΛCDM.

As we will see in §2.3.4, due to this amplification effect, at a later time, the total $\rho_{\mathrm{GW}}(a)$, integrated over all k but dominated by high-frequency modes which have reentered the horizon by the end of the stiff-SFDM-dominated era, will evolve nearly as radiation ($\propto a^{-4}$). Consequently, $\rho_{\mathrm{GW}}(a)$ will emerge as a significant contribution to the critical energy density of the ΛSFDM universe, as soon as the radiation-dominated

era begins.

2. **Superhorizon limit:**

   According to Eq. (2.53), the superhorizon ($k \ll aH/c$) GW energy density spectrum can be written as

   $$\Omega_{\rm GW}(k,a) = \frac{\Delta^2_{h,\ \rm init}(k)}{24}\left(\frac{kc}{aH}\right)^2 . \tag{2.64}$$

   Eq. (2.64) can be applied at all times during the superhorizon evolution of each mode k. Since $kc = a_k H_k$, this equation tells us that every mode reenters the horizon with almost the same fractional energy density ($\approx \Delta^2_{h,\ \rm init}(k)/24$).

3. **Thin-horizon approximation:**

   In the *thin-horizon approximation*, the horizon crossing of mode k is assumed to occur suddenly at $a = a_k$, and immediately follows the asymptotic behavior of the subhorizon evolution. We confirm that the assumption of thin-horizon crossing is a very good approximation for all eras of interest to us in the expansion history. As an example, we show in Appendix B.2 the exact solution for $h_k(\tau)$ and $\Omega_{\rm GW}(k,\tau)$, along with the asymptotic solutions for the latter in the sub- and superhorizon regime, for modes which reenter the horizon during reheating with a matter-like EOS ($w = 0$). One can see that the asymptotic solutions of $\Omega_{\rm GW}(k,\tau)$ not only perfectly trace the exact solution, in their regime of validity, but also that the range in $k\tau$ around horizon crossing is rather narrow, validating the thin-horizon approximation.

4. **Total GW energy density:**
   We apply the *thin-horizon approximation*, so that for each mode k, the superhorizon evolution of $\Omega_{\rm GW}(k,a)$ is given by Eq. (2.64) for all $a < a_k$, and the subhorizon evolution is given by Eq. (2.54) combined with Eq. (2.52) for all $a > a_k$ (or equivalently,

$\tau > \tau_k = \alpha/k$). We can then integrate the fraction of total SGWB energy density over all wavenumbers at any given time,

$$\begin{aligned}\Omega_{\rm GW}(a) &= \int_0^{k_{\rm hor}} \Omega_{\rm GW}(k,a)\mathrm{d}\ln k + \int_{k_{\rm hor}}^{k_{\rm inf}} \Omega_{\rm GW}(k,a)\mathrm{d}\ln k \\ &= \frac{rA_s}{24a^2H^2}\int_0^{k_{\rm hor}} c^2k^2\left(\frac{k}{k_*}\right)^{n_t}\mathrm{d}\ln k + \frac{rA_s}{12a^2H^2}\int_{k_{\rm hor}}^{k_{\rm inf}} c^2k^2\left(\frac{k}{k_*}\right)^{n_t} T_h(k,a)\mathrm{d}\ln k \\ &= \frac{rA_s}{24(2+n_t)}\left(\frac{k_{\rm hor}}{k_*}\right)^{n_t} + \frac{rA_s}{12a^2H^2}\int_{k_{\rm hor}}^{k_{\rm inf}} a_k^2H_k^2\left(\frac{k}{k_*}\right)^{n_t} T_h(k,a)\mathrm{d}\ln k, \end{aligned} \tag{2.65}$$

where $k_{\rm inf}$ is the wavenumber of the mode that just exits the horizon and then immediately reenters, when inflation ends at $a_{\rm inf}$, and we have used the relation $k_{\rm hor} = aH/c$ for the mode that fills the horizon at scale factor a, i.e., $a_{k_{\rm hor}} = a$. The integral in the above equation can be divided into two parts by $k_{\rm reheat}$, the wavenumber of the mode that fills the horizon at the end of reheating, when $T = T_{\rm reheat}$ and $a = a_{\rm reheat}$,

$$\begin{aligned}\int_{k_{\rm hor}}^{k_{\rm inf}} a_k^2H_k^2\left(\frac{k}{k_*}\right)^{n_t} T_h(k,a)\mathrm{d}\ln k =& \int_{k_{\rm reheat}}^{k_{\rm inf}} a_k^2H_k^2\left(\frac{k}{k_*}\right)^{n_t} T_h(k,a)\mathrm{d}\ln k \\ &+ \int_{k_{\rm hor}}^{k_{\rm reheat}} a_k^2H_k^2\left(\frac{k}{k_*}\right)^{n_t} T_h(k,a)\mathrm{d}\ln k. \end{aligned} \tag{2.66}$$

In the equation above, the contribution from reheating, assuming an EOS with $w = 0$, can be integrated analytically. The result is

$$\int_{k_{\rm reheat}}^{k_{\rm inf}} a_k^2H_k^2\left(\frac{k}{k_*}\right)^{n_t} T_h(k,a)\mathrm{d}\ln k = \frac{1}{2(2-n_t)}\frac{a_{\rm inf}^4H_{\rm inf}^2}{a^2}\left(\frac{a_{\rm reheat}}{a_{\rm inf}}\left(\frac{k_{\rm reheat}}{k_*}\right)^{n_t} - \left(\frac{k_{\rm inf}}{k_*}\right)^{n_t}\right). \tag{2.67}$$

2.3.3 Other cosmic components

Apart from SFDM and GWs, the other components are the same than in ΛCDM. In Table 2.1, $\Omega_r h^2$, calculated from the CMB temperature today $T_{\rm CMB}$, accounts for the ordinary radiation component, i.e. photons and neutrinos. For simplicity, the neutrinos are considered as *massless* (i.e. SM neutrinos), such that the total matter density fraction

today is $\Omega_m = \Omega_b + \Omega_c$, where Ω_b stands for the baryon density fraction at the present. The energy density of baryons (the "ordinary matter") always decays like non-relativistic "dust", $\rho_b(a) \propto a^{-3}$. While the radiation component decays asymptotically like $\rho_r(a) \propto a^{-4}$, photons do get extra heat during various processes in the early evolution. These effects are usually described via a quantity called g_* (or g factor), which reflects the change (decrease) of relativistic species over time. It amounts to calculating the thermal history exactly, i.e. the photon temperature T as a function of a during such periods. As in Paper I, we will again take into account the most notable of these changes, namely the time of electron-positron annihilation that occurs around 0.5 MeV. This effect will be reflected in our solutions as a little dip in the density fraction of radiation at that time. Finally, we assume a cosmological constant, $\rho_\Lambda = \text{const.}$, whose present-day density fraction is given by $\Omega_\Lambda = 1 - \Omega_m - \Omega_r$.

2.3.4 "Putting it together": homogeneous ΛSFDM universe

In this section, we couple the evolution of all cosmic components to obtain the expansion history of the homogeneous ΛSFDM universe. We will also introduce several cosmological observables, which we later use to constrain the ΛSFDM model. Inserting Eq. (2.14) and the relations mentioned in §2.3.3 into the post-reheating Friedmann equation (2.7) yields

$$\begin{aligned} H^2(a) &= H_0^2 \left(\frac{\Omega_r(a)}{a^4} + \frac{\Omega_b}{a^3} + \Omega_\Lambda \right) + H^2(a)\Omega_{\rm GW}(a) + \frac{8\pi G}{3c^2}\rho_{\rm SFDM} \\ &= H_0^2 \left(\frac{\Omega_r(a)}{a^4} + \frac{\Omega_b}{a^3} + \Omega_\Lambda \right) + H^2(a)\Omega_{\rm GW}(a) \\ &\quad + \frac{8\pi G}{3c^2}\left[\frac{\hbar^2}{2mc^2} \left(\frac{(\mathrm{d}|\psi|^2/\mathrm{d}t)^2}{4|\psi|^2} + \frac{(\rho_{\rm SFDM,0}/\hbar)^2}{a^6|\psi|^2} \right) + \frac{1}{2}mc^2|\psi|^2 + \frac{1}{2}\lambda|\psi|^4 \right], \end{aligned} \tag{2.68}$$

where Ω_b and Ω_Λ are given in Table 2.1, the parameter $\Omega_r(a)$ is different before and after the electron-positron annihilation[12], and $\Omega_{\rm GW}(a)$ is evaluated by Eqs. (2.65) – (2.67). Unlike the

[12]After the e^-e^+ annihilation, $\Omega_r(a)$ is equal to the present-day radiation energy density fraction given in Table 2.1. It is slightly smaller before the e^-e^+ annihilation because photons get heated as e^-e^+ pairs

standard ΛCDM universe in which the Friedmann equation can be solved separately from the equations of motion for each component, it is necessary in the case of SFDM, to solve Eq. (2.68) fully coupled to the Klein-Gordon equation (2.24), the equation of motion for the SFDM. Therefore, a numerical integration is required, which we will describe in §2.3.4.1.

To start the description of the evolution of the homogeneous universe, we first remind the reader that, ΛSFDM is embedded in the standard inflationary paradigm in a way similar to ΛCDM, that a ΛSFDM universe commences in a period of cosmic inflation which ends in reheating, as explained in §2.1.4. In the single-field slow-roll inflation picture, the energy scale of inflation, or equivalently, the Hubble constant at the end of inflation, $H_{\rm inf}$, can be determined by the value of the tensor-to-scalar ratio r,

$$H_{\rm inf} = \frac{\pi M_{\rm pl}}{\hbar}\sqrt{rA_s}, \tag{2.69}$$

where $M_{\rm pl}$ is the reduced Planck mass, $M_{\rm pl} \equiv \sqrt{\frac{\hbar c}{8\pi G}}$.

When inflation ends, the inflaton oscillates and decays, which results in particle production and reheating ($w = 0$). The end of reheating is considered as the emergence of SFDM as well as the SM particles, produced during reheating. Unlike in ΛCDM, in our ΛSFDM model reheating dumps most of the energy of the inflaton into SFDM, which quickly forms a Bose-Einstein condensate, as argued in §2.1.2. Meanwhile, a subdominant amount of energy is dumped into the SM particles, which was a radiation component at $T = T_{\rm reheat}$. In ΛSFDM, this is the moment when the cosmic expansion history starts to be distinguishable from ΛCDM.

annihilate into photons in thermal equilibrium. We take this into account in our evolution of the thermal history of the universe.

While the Hubble constant when inflation ends is fixed in ΛSFDM by Eq. (2.69), the value of H when reheating ends is set by the value of $a = a_{\rm reheat}$ when $T = T_{\rm reheat}$, which cannot be determined on its own without solving the holistic evolution that follows to match the observed universe at present in the presence of SFDM. This will be apparent if we preview the generic behavior of the expansion history in the full solutions we will calculate later in this section. Fig. 2.1 (based upon the calculation detailed later) shows a plot of the Hubble parameter for several ΛSFDM models with different parameters, as a function of scale factor, in which the varying EOS of the background universe is reflected in different slopes. Following the end of inflation at $a = a_{\rm inf}$, $H \propto a^{-3/2}$ during reheating until $a = a_{\rm reheat}$. At this point, the ΛSFDM universe is dominated by stiff SFDM, rather than radiation. We have described the relativistic nature of SFDM at early times in §2.3.1, that BEC SFDM starts as stiff matter ($w = 1$), and then transitions into a radiationlike ($w = 1/3$) component, before a final transition into dustlike CDM ($w = 0$). Therefore, we expect to see that, as the energy density of the dominant stiff SFDM decreases as $\rho_{\rm SFDM} \propto a^{-6}$ (faster than radiation), the initially stiff-SFDM-dominated universe ($H \propto a^{-3}$) will later experience a transition in its EOS to radiation-dominated, when SFDM and other relativistic species combine to make the critical energy density of the universe $\rho_{\rm crit} \propto a^{-4}$, so $H \propto a^{-2}$, until the SFDM transitions to CDM-like and once again dominates $\rho_{\rm crit}$, then $H \propto a^{-3/2}$.

It can be inferred from above that, during the stiff and radiationlike phase of SFDM, the expansion rate of the background ΛSFDM universe in its early stage is increased, compared to that in ΛCDM (see Fig. 2.1). Hence, in the ΛSFDM model, SFDM will contribute to the effective number of relativistic species, also known as effective number of neutrino species, $N_{\rm eff}$. In ΛCDM, where there are only three SM neutrinos, $N_{\rm eff} = N_{\rm eff,standard} = 3.046$. In

ΛSFDM, an increased expansion rate can be translated into an increased $N_{\rm eff}$, or vice versa. Thus, measurements of the value of $N_{\rm eff}$ at a certain time will constrain the expansion rate of the ΛSFDM universe at that time.

In fact, BBN is such an epoch during which the value of $N_{\rm eff}$ can be measured, by determining primordial light element (He, D, etc.) abundances from observations. Standard BBN proceeds in a period between the freeze-out of the neutron-proton ratio when the photon temperature $T \simeq T_{\rm n/p} \equiv 1.293$ MeV (the difference between the neutron and the proton mass) and the epoch of nuclei production when $T \simeq T_{\rm nuc} \approx 0.07$ MeV. We denote the respective scale factors as $a_{\rm n/p}$ and $a_{\rm nuc}$. A detailed analysis on how the value of $N_{\rm eff}$ during BBN constrains the expansion rate of ΛSFDM, and thereby the SFDM particle parameters, will be carried out in §2.4.2.

Later in the expansion history of ΛSFDM, the universe undergoes another transition from radiation-dominated (RD) to matter-dominated (MD). The division of these two eras is described by the epoch of matter-radiation equality, the redshift at which is denoted as $z_{\rm eq}$. Note that in ΛSFDM, matter-radiation equality refers to the equality between the energy density of the matter component (SFDM plus baryons) and the radiation component (including GWs). After $z_{\rm eq}$, the overdensities in the matter-dominated universe start to grow in proportion to the scale factor, which become seeds for forming cosmic structures. Since we consider SFDM as a variant of CDM, which retains the cosmic structure on large enough scales as predicted by standard CDM (see §2.1.1), we should expect that the expansion history of the background ΛSFDM universe be nearly identical to that in ΛCDM, after the same $z_{\rm eq}$. Besides LSS, $z_{\rm eq}$ is a cosmological observable well determined by CMB anisotropy measurements independently. Therefore, ΛSFDM must respect the value of $z_{\rm eq}$ measured

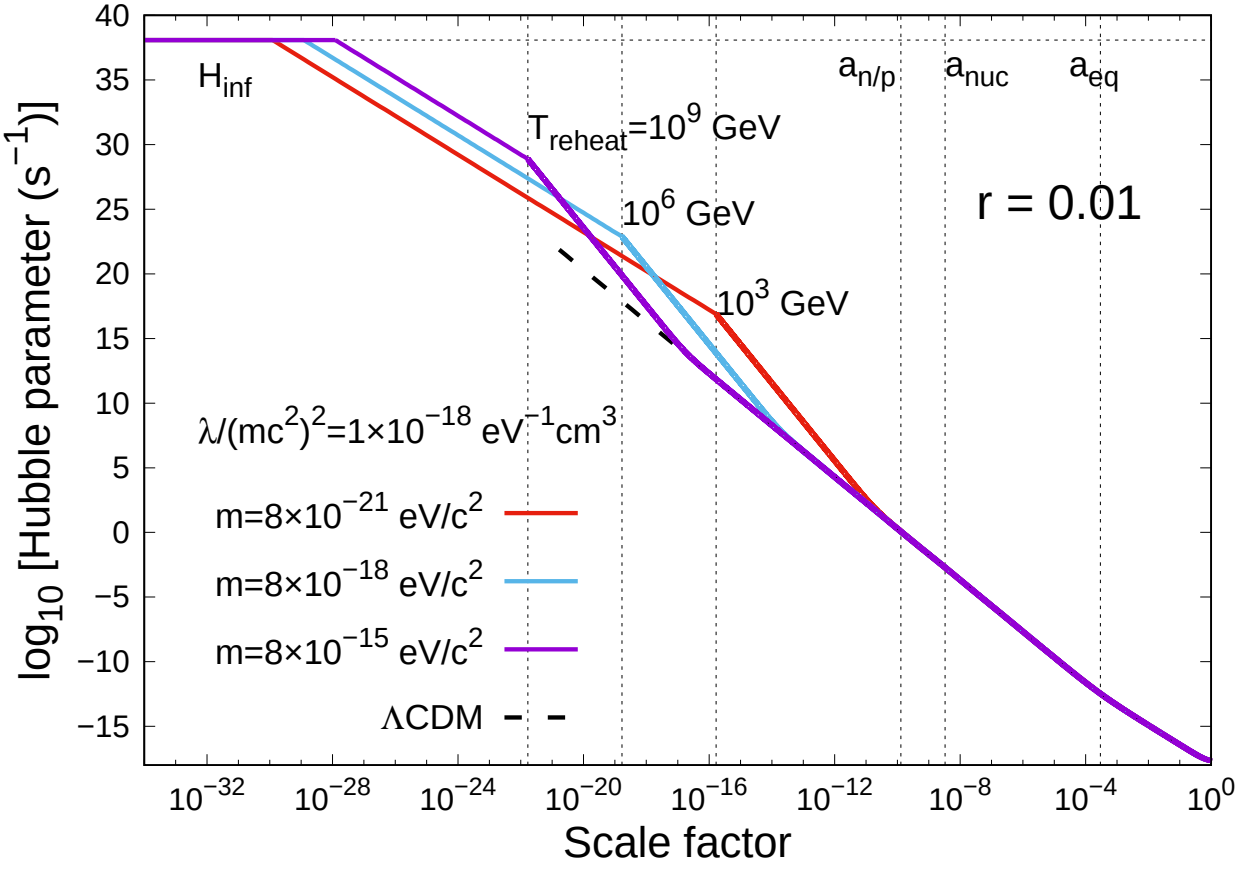

Figure 2.1: Expansion history of 3 example ΛSFDM models in the standard inflation paradigm including an epoch of standard reheating ($w = 0$).

by the CMB. In other words, $z_{\rm eq}$ puts constraints on ΛSFDM, too, which we will discuss in §2.4.1.

The combination of these constraints will allow us to determine allowed ranges of SFDM particle parameters. Allowed regions will correspond to those SFDM models which comply to all the current measurements of the background evolution. The results will be summarized in §2.4.3.

2.3.4.1 Numerical method

In Paper I, we presented many details of how the evolution of SFDM is numerically calculated, so we refer the reader to that paper for more technical details. We emphasize that, as in Paper I, there are basically two different calculational regimes, as follows. When $\omega/H \gg 1$, the fast-oscillation approximation applies, as described in §2.3.1.1. As long as the oscillation is much faster than the rate at which the scale factor changes, the exact SFDM energy density and pressure should be well approximated by the corresponding time-averaged quantities, and we confirmed in Paper I that this is indeed the case.

At earlier times, ω/H decreases and the fast-oscillation approximation becomes invalid. Then, we have to work in the slow-oscillation regime as described in §2.3.1.2, and the evolution of SFDM has to be calculated exactly, with no reference to an averaging procedure.

The presence of $\rho_{\rm GW}$, which is dependent on the expansion history and, in turn, affects that history, requires us to generalize the method of Paper I. In addition, we have improved the accuracy of our numerical solutions.

(1) Nondimensionalized equations

We have rewritten the coupled Klein-Gordon and Friedmann equations in a nondimensionalized form which takes advantage of the characteristic scales of the dimensional quantities expected during the early, slow-oscillation regime, to improve the accuracy of our numerical solutions.

In the early-time slow-oscillation regime, we solve the Klein-Gordon equation (2.24) directly in terms of the field amplitude square $|\psi|^2$ as the dependent variable, coupled

with the Friedmann equation (2.68). The hydrodynamical variables $\rho_{\rm SFDM}$ and $p_{\rm SFDM}$ are then related to $|\psi|^2$ by Eqs. (2.14) and (2.15).

In particular, we have nondimensionalized this set of ordinary differential equations (ODEs) by expressing variables in terms of their values at the matching point at $a = a_M$, between the slow-oscillation regime and the late-time fast-oscillation regime. We define the dimensionless dependent variable for our numerical integration as follows:

$$y \equiv \frac{|\psi|^2}{|\psi_M|^2}, \tag{2.70}$$

where ψ_M is the value of the scalar field at the matching point. The independent variable, cosmic time t is nondimensionalized as:

$$x \equiv \omega_M t, \tag{2.71}$$

where ω_M is the oscillation frequency of the scalar field at the matching point. Likewise the dimensionless Hubble parameter is defined as:

$$\mathscr{H} \equiv H/\omega_M. \tag{2.72}$$

We note that according to the definition of the Hubble parameter,

$$\dot{a} = \mathscr{H} a, \tag{2.73}$$

where the upper dot denotes the derivative with respect to the dimensionless time variable x, *throughout this subsection*.

Given these variables, the dimensionless equivalent of the Klein-Gordon equation (2.24) can be written as

$$\ddot{y} = -3\mathscr{H}\dot{y} + \frac{\dot{y}^2}{2y} + \frac{2F_1}{a^6 y} - 2F_2 y - 4F_3 y^2, \tag{2.74}$$

in which dimensionless constants F_1, F_2 and F_3 are defined as

$$F_1 \equiv \frac{(\rho_{\rm SFDM,0}/\hbar)^2}{\omega_M^2|\psi_M|^4}, \tag{2.75}$$

$$F_2 \equiv \frac{(mc^2)^2}{(\hbar\omega_M)^2} \tag{2.76}$$

$$F_3 \equiv \frac{\lambda mc^2|\psi_M|^2}{(\hbar\omega_M)^2}. \tag{2.77}$$

For the dimensionless version of the Friedmann equation, combining Eq. (2.68) with the expressions of the dimensionless variables and constants above yields

$$\begin{aligned}\mathscr{H}^2 = \mathscr{H}_0^2\left(\frac{\Omega_r(a)}{a^4}+\frac{\Omega_b}{a^3}+\Omega_\Lambda\right)+\mathscr{H}^2\Omega_{GW}(a)\\ +\frac{\dot{y}^2}{24y}+\frac{F_1}{6a^6y}+\frac{F_2y}{6}+\frac{F_3y^2}{6},\end{aligned} \tag{2.78}$$

where $\mathscr{H}_0 = H_0/\omega_P$ apparently.

The ODEs (2.73), (2.74) and (2.78) will be coupled to solve the holistic evolution of ΛSFDM, provided we are able to evaluate $\Omega_{\rm GW}(a)$ at any scale factor self-consistently.

(2) Integration and iteration scheme

We use a publicly-available ODE solver, *DVODE* [136], which can solve stiff systems in double precision, for all our numerical integrations. In Paper I, we integrated the evolution backward in time, using cosmological parameters at the present as the initial condition, given by the Planck 2013 results [7] . This was necessary in Paper I because otherwise we would have needed to know the initial value of the scalar field and its time derivative, in the early universe, as well as the (conserved) comoving charge density Q, in order to integrate forward in time, but only Q is known in advance (see Eq. [2.17]).

However, it is difficult for the backward calculation to take into account the SGWB produced by inflation self-consistently. Therefore, in this paper, we must evolve the

ODEs forward in time, and iterate. We use a backward integration to make a first guess for the starting values to use in the next forward integration, and subsequently iterate by a sequence of backward-forward integrations designed to converge. Convergence in this case means that the end result of a *forward* integration reaches the values of the present-day cosmological parameters in Table 2.1 at $a = 1$ with sufficient accuracy, as described below.

For each forward integration, we need to guess the starting values to use for the scalar field and its time derivative at $a = a_{\rm reheat}$. For this, we depend upon a backward integration from the known values of the cosmological parameters at $a = 1$. Unfortunately, the contribution to the total energy density from $\rho_{\rm GW}$ depends upon the accumulation of tensor modes over time as they reenter the horizon, which can only be determined self-consistently by a *forward* integration. Hence, backward integrations, too, must incorporate some guess, for the evolution of $\rho_{\rm GW}(a)$.

For the very first iteration, we integrate backward, neglecting $\rho_{\rm GW}$. A forward integration is then performed from $a = a_{\rm reheat}$ to $a = 1$ and the outcome compared with the cosmological parameters in Table 2.1 used to start the backward integration. In particular, we see how close the ending of $\rho_{\rm SFDM}$ is from $\rho_{\rm SFDM,0}$. For $\Delta \equiv \rho_{\rm SFDM}/\rho_{\rm SFDM,0} - 1$, if $\Delta \leq 0.001$, the iteration is deemed to have converged. If, however, $\Delta > 0.001$, then we guess the evolution of $\rho_{\rm GW}(a)$ based upon that first forward integration and insert it in a new backward integration, to find better starting values for the next forward integration. There is a simplification that makes a good $\rho_{\rm GW}(a)$ guess possible, based upon the generic behavior of solutions that are cosmologically allowed. While $\rho_{\rm GW}(a)$ increases over time during reheating and the stiff-SFDM-dominated era, as more and

more modes reenter the horizon, this increase peaks when the stiff era ends. Thereafter, for most cases of interest, with a substantial stiff era, $\rho_{\rm GW}(a)$ evolves like radiation, i.e., $\rho_{\rm GW}(a) \simeq \rho_{\rm GW}(a=1)/a^4$. As a result, we can use this assumed behavior, along with the final value of $\rho_{\rm GW}$ at $a = 1$ from the last forward integration. This can be extrapolated safely back to $a_{\rm reheat}$ in the following backward integration, since $\rho_{\rm GW}$ does not affect the expansion history at earlier times when the energy density of the universe is dominated by the SFDM in the stiff phase. In cases in which the stiff era is too limited in duration to boost $\rho_{\rm GW}$ significantly above the value in ΛCDM, $\rho_{\rm GW}$ is so small that there is no back-reaction on the expansion rate, so this radiationlike extrapolation from $a = 1$ backward in time is fine, as well, since it makes no difference.

In general, each new forward integration in this iteration scheme yields a new, improved $\rho_{\rm GW}(a)$ guess to use in the next backward integration. These iterations are continued until the threshold for convergence is achieved ($\Delta \leq 0.001$) for a forward integration. For example, in the case in which successive iterations cause an increase in Δ, we discard the current iteration and examine carefully the last iteration, to improve the $\rho_{\rm GW}(a)$ guess for the next iteration, by a bisection of the guesses in two previous iterations. There are details for safely converging, which we leave aside.

For the backward integration, we follow the same numerical method as in Paper I. We apply the *fast-oscillation approximation* from the present up to the matching point at $a = a_M$, where that approximation is still valid. We refer to the solution obtained in this regime as the "late-time solution". Then, starting from the matching point, we calculate the *exact* evolution (without any approximation), all the way back to the point at $a_{\rm reheat}$, i.e. the point at which SFDM comes into existence. We refer to this

part as the "early-time solution".

When we integrate forward in time, starting from $a_{\rm reheat}$ with the initial condition provided by the backward integration, we obtain the early-time solution first. We have to solve the coupled ODEs (2.73), (2.74) and (2.78) exactly, since we are in the slow-oscillation regime. This recipe is carried out up to the matching point, after which we can apply the fast-oscillation approximation again. Then we combine Eqs. (2.68), (2.23) and (2.33) to calculate the late-time solution.

The contribution from the SGWB is accounted for *self-consistently* in the forward integration, by the following treatment of $\Omega_{\rm GW}(a)$ which appears in the dimensionless Friedmann equation (2.78). As shown in Eq. (2.65), $\Omega_{\rm GW}(a)$ is integrated over all wavenumbers k. At each time step, we add to the integral the contribution from the mode that reenters the horizon at the current time step. In fact, using Eqs. (2.65) – (2.67),

$$\begin{aligned}
\Omega_{\rm GW}(a) &= \left(\int_{k_{\rm reheat}}^{k_{\rm inf}} \Omega_{\rm GW}(k,a)\mathrm{d}\ln k + \int_{k_{\rm hor}+\Delta k}^{k_{\rm reheat}} \Omega_{\rm GW}(k,a)\mathrm{d}\ln k + \Omega_{\rm GW}(k,a)\Delta\ln k\right) \\
&\quad + \int_0^{k_{\rm hor}} \Omega_{\rm GW}(k,a)\mathrm{d}\ln k \\
&= \frac{rA_s}{24(2-n_t)}\frac{a_{\rm inf}^4 H_{\rm inf}^2}{a^4H^2}\left(\frac{a_{\rm reheat}}{a_{\rm inf}}\left(\frac{k_{\rm reheat}}{k_*}\right)^{n_t} - \left(\frac{k_{\rm inf}}{k_*}\right)^{n_t}\right) \\
&\quad + \frac{rA_s}{12a^2H^2}\int_{k_{\rm hor}+\Delta k}^{k_{\rm reheat}} a_k^2 H_k^2 T_h(k,a)\left(\frac{k}{k_*}\right)^{n_t}\mathrm{d}\ln k \\
&\quad + \frac{rA_s}{12}T_h(k_{\rm hor},a)\left(\frac{k_{\rm hor}}{k_*}\right)^{n_t}\Delta\ln k + \frac{rA_s}{24(2+n_t)}\left(\frac{k_{\rm hor}}{k_*}\right)^{n_t},
\end{aligned} \tag{2.79}$$

where $k_{\rm hor} = aH/c$ is the wavenumber of the mode that fills the horizon at the current time step and Δk is the difference between such a wavenumber at the current time step and the previous one, $\Delta\ln k \equiv \Delta k/k$. The equation above demonstrates how we account for $\Omega_{\rm GW}(a)$ in the coupled ODEs, for both the early-time and late-time solution.

The tensor transfer function $T_h(k,a)$ that we use in Eq. (2.79) is the one in Eq. (2.52) in which α_k is evaluated with the corresponding $w(a_k) = p(a_k)/\rho(a_k)$ of the background universe, multiplied by a factor A^2 mentioned at the end of §2.3.2.2, which accounts for the damping of tensor modes from free-streaming neutrinos, which is nontrivial during the radiation-dominated era. It was first pointed out by [132] that, since a free-streaming relativistic component contributes an anisotropic stress-energy tensor π_{ij} on the right-hand side of the tensor wave equation (2.27), the growth of h_k will be damped, once it reenters the horizon, compared with the solution without anisotropic inertia (see §2.3.2.2). This effect amounts to a multiplicative factor A as a function of the fraction of the free streaming species, calculated by [133]. In cosmology, the only important case is the free streaming neutrinos during the radiation-dominated era, when their fraction $\Omega_\nu(a)$ is not negligible. Therefore, $A = A(\Omega_\nu(a))$ should be applied to modes which reenter the horizon during the radiation-dominated era. In this paper, we will only quote the result of $A(\Omega_\nu(a))$ from [133], and incorporate it into Eq. (2.79), which yields

$$\begin{aligned}\Omega_{\rm GW}(a) = &\frac{rA_s}{24(2-n_t)}\frac{a_{\rm inf}^4 H_{\rm inf}^2}{a^4H^2}\left(\frac{a_{\rm reheat}}{a_{\rm inf}}\left(\frac{k_{\rm reheat}}{k_*}\right)^{n_t} - \left(\frac{k_{\rm inf}}{k_*}\right)^{n_t}\right)\\ &+ \frac{rA_s}{12a^2H^2}\int_{k_{\rm hor}+\Delta k}^{k_{\rm reheat}} a_k^2H_k^2T_h(k,a)\left(\frac{k}{k_*}\right)^{n_t}A^2(\Omega_\nu(a))\mathrm{d}\ln k\\ &+ \frac{rA_s}{12}T_h(k_{\rm hor},a)\left(\frac{k_{\rm hor}}{k_*}\right)^{n_t}A^2(\Omega_\nu(a))\Delta\ln k + \frac{rA_s}{24(2+n_t)}\left(\frac{k_{\rm hor}}{k_*}\right)^{n_t}\end{aligned} \quad (2.80)$$

This equation (2.80) is the final version of $\Omega_{\rm GW}(a)$ which we insert into the dimensionless Friedmann equation (2.78) for our numerical calculation. We are hereby able to treat the back reaction of GWs unto the expansion history of the background ΛSFDM universe, an effect that has not been self-consistently taken into account in previous literature. In this paper, we provide the first example of a holistic numerical evolution of the homogenous universe, which correctly accounts for the back reaction from GWs, while including all contributions to the total energy density of the universe.

2.3.4.2 Results: example ΛSFDM models

We will now show the evolutionary aspects of ΛSFDM by presenting results for some example models obtained from our numerical calculation in detail.[13] As we sill see in §2.4, these models are chosen to fulfill the constraints from the observables described there and in §2.3.4, while still being in the range of parameters of interest for solving the small-scale structure problems of CDM.

Again, we refer the reader to Fig. 2.1, the evolution of the Hubble parameter of several example ΛSFDM models with different parameters, as a function of scale factor. As in Paper I, we find it convenient to work with the ratio $\lambda/(mc^2)^2$, rather than λ, because many observables constrain the former, rather than the latter. For all these example models, the value of $\lambda/(mc^2)^2$ is chosen to be

$$\lambda/(mc^2)^2 = 1 \times 10^{-18}\ \mathrm{eV}^{-1}\ \mathrm{cm}^3. \tag{2.81}$$

The value of $\lambda/(mc^2)^2$ corresponds, for example, to the minimum size of a virialized halo in SFDM models with significant self-interaction, in the Thomas-Fermi regime (see §2.1.3), i.e. choosing a fixed value for $\lambda/(mc^2)^2$ amounts to fixing the minimum clustering scale below which structure formation is suppressed. Since observations suggest a scale of order kpc, we adopt the above value, corresponding to a scale of 0.8 kpc (which is smaller than that of the fiducial model in Paper I).

Also, the value of the tensor-to-scalar ratio is fixed, $r = 0.01$, for all three models in Fig 2.1. It satisfies the latest upper bound given in Table 2.1, $r < 0.07$, from CMB

[13]The fiducial model in Paper I was $m = 3 \times 10^{-21}$ eV/c^2, $\lambda/(mc^2)^2 = 2 \times 10^{-18}$ eV^{-1}cm^3, see Fig. 1,2,3 in [1].

polarization experiments. The other input parameters, the SFDM particle mass m and the reheat temperature $T_{\rm reheat}$, are varied among the three models, as illustrated by the plot labels. We have chosen three values for the reheat temperature, $T_{\rm reheat} = 10^3,\ 10^6$ and 10^9 GeV, which span a wide range of possible $T_{\rm reheat}$ in ΛSFDM (the energy density at $T_{\rm reheat}$ should not exceed the inflationary energy scale). We vary the SFDM particle mass m accordingly with these choices of $T_{\rm reheat}$, so as to satisfy the constraints described in §2.4.

As shown in Fig 2.1, the Hubble parameter of the universe drops from the initial plateau, $H_{\rm inf}$, when inflation ends, at different scale factors $a_{\rm inf}$ for different example models. The duration of the prolonged $w = 0$ reheating, in which $H(a) \propto a^{-3/2}$, is also different among these models. In accordance with the definition of $T_{\rm reheat}$, the higher it is, the shorter the duration of reheating. The end of reheating marks the emergence of BEC SFDM and all the SM particles. To describe the homogeneous evolution of the ΛSFDM universe hereafter, we will focus on one of the example models, in which $T_{\rm reheat} = 10^3$ GeV, and

$$m = 8 \times 10^{-21}\ {\rm eV/c^2}. \tag{2.82}$$

For this model, the evolution of the Hubble parameter as a function of scale factor is plotted in Fig. 2.2, and the evolution of the energy density fractions of all its components can be found in the left-hand plot of Fig 2.3. We can see that SFDM dominates in the universe twice: first, from the time of the onset of the stiff phase —which follows the epoch of reheating at $a_{\rm reheat}$, to shortly before the time of neutron-proton freeze-out $a_{n/p}$, and then after the time of matter-radiation equality at $a_{\rm eq}$ to shortly before the present, which is Λ-dominated. At present, Ω_i of all the components, as well as the Hubble constant H_0, match the cosmological parameters measured by Planck in Table 2.1.

The intermediate radiation-dominated era of ΛSFDM also has a different expansion history from that of ΛCDM. There are two extra radiation components besides the standard radiation (photons plus neutrinos), namely radiationlike SFDM and primordial GWs amplified by the stiff era. As shown in the left-hand plot of Fig. 2.3, $\Omega_{\rm SFDM}$ is constant during its radiationlike phase, as a "plateau" (see Paper I for a more detailed description). In the same era, this model allows for another plateau contributed by the energy density fraction of the SGWB from inflation, $\Omega_{\rm GW}$. As predicted in §2.3.2.3, it is possible that $\rho_{\rm GW}$ can emerge as a significant contribution to the total energy density of the universe during the RD era (indicated by the plateau of $\Omega_{\rm GW}$ in the left-hand plot of Fig. 2.3), resulting from the amplification of subhorizon GWs during the stiff-SFDM-dominated era. For all the example models shown here, the boost effect is significant, due to the considerable number of e-foldings during the stiff era. For tensor modes that reenter the horizon after the stiff-SFDM-domination ends, of lower frequencies than those that reentered before, their energy density is not boosted relative to that of the background universe, so they add little to the total energy density of the SGWB, or its fraction $\Omega_{\rm GW}(a)$ given by Eq. (2.65), throughout their subhorizon evolution. Hence, for ΛSFDM models like these, $\Omega_{\rm GW}(a)$ will always be dominated by modes which have reentered the horizon by the end of the stiff-SFDM-dominated era. From that moment on, the relative contributions to the total $\rho_{\rm GW}(a)$ are fixed for all modes that contribute significantly, and, as subhorizon modes, they evolve thereafter like radiation, $\mathrm{d}\rho_{\rm GW}/\mathrm{d}\ln k \propto a^{-4}$, thus, so must $\rho_{\rm GW}(a) \propto a^{-4}$ approximately. Therefore, $\Omega_{\rm GW}(a)$, only beginning to emerge at the end of the stiff-SFDM-dominated era, soon stops growing and becomes a plateau when the stiff-to-radiation transition finishes.

The evolution of the SFDM, itself, is shown in Fig. 2.4, from our numerical calcula-

tion. The respective phases of stiff, radiationlike, and CDM-like evolution are indicated in the left-hand plot. They follow the behavior derived heuristically in §2.3.1. The right-hand plot shows the evolution of the EOS parameter of the SFDM $w = p_{\rm SFDM}/\rho_{\rm SFDM}$, respectively. The wiggles in this figure reflect the oscillatory nature of the scalar field ψ, which generally appear in exact solutions of all types of DM modeled by a scalar field (see, e.g., [137]). This oscillation feature stops at $a = a_M$ when we change the calculational method, between the slow- and the fast-oscillation regime (see and §2.3.1 and §2.3.4.1). Note that there are no wiggles in the left-hand plot of Fig 2.4, indicating that the oscillations are not manifest in $\rho_{\rm SFDM}$, only in $p_{\rm SFDM}$. This guarantees that the expansion history of the background universe, which only depends on the mean energy density of SFDM, is not affected by these oscillations.

For fixed r and $T_{\rm reheat}$, the transition of the SFDM EOS between the radiationlike ($w = 1/3$) and CDM-like (matter-like, $w = 0$) phase is determined solely by the parameter $\lambda/(mc^2)^2$. The larger $\lambda/(mc^2)^2$ is, the later the transition. In contrast, the transition between the stiff ($w = 1$) and radiationlike phase is determined by both SFDM particle parameters, m and $\lambda/(mc^2)^2$. In other words, while the beginning of the stiff phase is set by $T_{\rm reheat}$, its end is determined by both m and $\lambda/(mc^2)^2$. For fixed $\lambda/(mc^2)^2$, the larger the mass m, the earlier the stiff phase ends. For fixed m, the larger $\lambda/(mc^2)^2$ is, the earlier the stiff phase ends, as well. In the limit of small $\lambda/(mc^2)^2$, the end of the stiff phase is determined primarily by m alone. Hence, the duration of each phase can be tuned by SFDM particle parameters. It was also shown in Paper I how changing these parameters affects the evolution of SFDM.

We highlight again that SFDM in its early stiff phase dominates the energy density of the background universe, which gives rise to several interesting implications on cosmological

observables as mentioned above in §2.3.4. For example, both SFDM and GWs contribute to $N_{\rm eff}$ during BBN (from $a_{\rm n/p}$ to $a_{\rm nuc}$), increasing the expansion rate of the background universe. The evolution of $N_{\rm eff}$ during BBN is illustrated in the right-hand plot of Fig 2.3. For the example model, the contribution from the SGWB from inflation is noticeable. When SFDM transitions from radiationlike to CDM-like, it will no longer contribute to $N_{\rm eff}$. However, the SGWB contribution will always remain, which could affect other cosmological observables at later times, such as $z_{\rm eq}$. Therefore, such observables will be capable of constraining ΛSFDM parameters, via the relic SGWB from inflation. We will carry out the analyses and show results from these constraints in the next section.

2.4 Results: new constraints on SFDM particle parameters from cosmological observables

2.4.1 Constraint from matter-radiation equality $z_{\rm eq}$

As briefly mentioned in §2.3.4, a ΛSFDM model has to preserve the redshift of matter-radiation equality, $z_{\rm eq}$, according to the measurement from CMB. The constraint on the value of $z_{\rm eq}$ from the Planck 2015 results reads

$$z_{\rm eq} = 3365 \pm 44, \quad (68\% \text{ confidence limit}). \tag{2.83}$$

This requires that SFDM should be well into its CDM-like phase (i.e. be fully non-relativistic) at $z_{\rm eq}$. As a result, it sets a constraint on the transition point between the radiation-like and CDM-like phases of SFDM, which is a function of $\lambda/(mc^2)^2$, as described in §2.3.4.2 and in Paper I. As long as SFDM has completed this transition well before $z_{\rm eq}$, one can derive from the definition of $z_{\rm eq}$ that

$$1 + z_{\rm eq} \equiv \frac{1}{a_{\rm eq}} = \frac{\Omega_b h^2 + \Omega_c h^2}{\Omega_r h^2 + \Omega_{\rm GW} h^2}, \tag{2.84}$$

where $a_{\rm eq}$ is the scale factor at matter-radiation equality, and $\Omega_i h^2$ $(i = b, c, r)$ is given in Table 2.1. In particular, $\rho_{\rm SFDM}$ after the transition evolves as matter all along until today and matches the present-day value determined by $\Omega_c h^2$. We first ignore the term $\Omega_{\rm GW} h^2$ in Eq. (2.84) for a moment, as in Paper I. Then the value of $z_{\rm eq}$ calculated by Eq. (2.84) must exactly agree with the constraint in Eq. (2.83). Therefore, without GWs, the only aspect through which SFDM is constrained is its radiation- to CDM-like transition point, governed by $\lambda/(mc^2)^2$. We have shown this constraint on $\lambda/(mc^2)^2$ in Paper I. Here we update it with the latest constraint on $z_{\rm eq}$ in Eq. (2.83), but use the same threshold value of $w = p/\rho = 0.001$ (neglecting the subscript SFDM here), a tiny deviation from zero, to indicate the point after which SFDM can be considered as fully non-relativistic (i.e., $w < 0.001$ for $a > a_{w=0.001}$). The requirement of $a_{w=0.001} \leq a_{\rm eq}$ can be translated into the following constraint on $\lambda/(mc^2)^2$:

$$\frac{\lambda}{(mc^2)^2} \leq 4.3 \times 10^{-17}\ {\rm eV}^{-1}\ {\rm cm}^3. \tag{2.85}$$

The choice of this threshold $w = 0.001$ is artificial. If we relaxed it to higher values of w, the corresponding constraint on $\lambda/(mc^2)^2$ would become less tight, allowing a broader range of values. A more precise threshold would require a recalculation of the CMB power spectrum for different SFDM particle parameters, to solve for the best-fitting ΛSFDM parameters, which is well-beyond the scope of this paper.

Now we add the contribution from the amplified inflationary SGWB. From Eq. (2.84), we see that not only should SFDM be fully non-relativistic by $z_{\rm eq}$, but the amount of $\Omega_{\rm GW}$, amplified by the stiff era, is also subject to the constraint. Since for fixed r and $T_{\rm reheat}$, $\Omega_{\rm GW}(a)$ is determined by SFDM particle parameters, m and $\lambda/(mc^2)^2$, *both* these parameters will be constrained further. By matter-radiation equality, $\Omega_{\rm GW}(a)$ has already evolved

through the "plateau" described in §2.3.4.2, the height of which is determined by the duration of the stiff-SFDM-dominated era. The later the stiff era ends, the more modes get amplified and thus the higher the plateau of $\Omega_{\rm GW}(a)$ is, which will result in a later $z_{\rm eq}$ as inferred from Eq. (2.84). Therefore, to keep it in agreement with the measured value of $z_{\rm eq}$, it is required that the stiff phase of SFDM ends early enough. We adopt the -1σ confidence limit in Eq. (2.83) as the minimum allowed value for $z_{\rm eq}$. Thus, for fixed r and $T_{\rm reheat}$, there will be a lower limit on the mass m for each allowed value of $\lambda/(mc^2)^2$. With the inclusion of GWs, the allowed range of $(\lambda/(mc^2)^2,\ m)$ due to the $z_{\rm eq}$ constraint will be more stringent than the half-plane given by Eq. (2.85) for the case without GWs. This is illustrated in the SFDM particle parameter space, shown in Figs. 2.5 and 2.6. A detailed description of the allowed ranges from the $z_{\rm eq}$ constraint, parametrized by r and $T_{\rm reheat}$, will be given in §2.4.3.

2.4.2 Constraint from $N_{\rm eff}$ during Big Bang nucleosynthesis

The effective number of neutrino species, $N_{\rm eff}$, is introduced in §2.3.4 as a measure of relativistic degrees of freedom of the universe. It affects the expansion rate in the early universe, at all times before the matter-dominated era, which encompasses the important epoch of Big Bang nucleosynthesis. The abundances of primordial light elements produced by BBN are very sensitive to the expansion rate then. As a result, measurements of these abundances through astronomical observations of metal-poor systems set a constraint on $N_{\rm eff,BBN}$ during BBN [138, 139, 140]. BBN is not an instantaneous event; it undergoes two important stages which we explained in §2.3.4, first, neutron-to-proton freeze-out occurs at $a_{\rm n/p}$ and then, light nuclei production occurs at $a_{\rm nuc}$ [141], where $a_{\rm nuc}/a_{\rm n/p} \simeq T_{\rm n/p}/T_{\rm nuc} \approx 20$. Therefore, BBN actually cares about the evolution of $N_{\rm eff,BBN}(a)$ throughout this window

$(a_{\rm n/p},\ a_{\rm nuc})$. Nevertheless, it is often the case that only a single value of $N_{\rm eff,BBN}$ is reported from observations, in which the expansion history is modeled by a constant $N_{\rm eff,BBN}$ at all times, since it is the simplest model to fit. In this paper, we use the following measurement result [139] to constrain the SFDM model,

$$N_{\rm eff,BBN} = 3.56 \pm 0.23, \quad (68\% \text{ confidence limit}). \tag{2.86}$$

We comment that this value is not required to be consistent with the $N_{\rm eff,CMB}$ measured by CMB anisotropies, because $N_{\rm eff}(a)$ can in principle evolve over time as in our ΛSFDM model (see Fig. 2.3), and $N_{\rm eff,CMB}$ is only affected by its values later at around recombination. In other words, $N_{\rm eff,BBN}$ and $N_{\rm eff,CMB}$ indicate relativistic degrees of freedom at *different* epochs of the expansion history. As a matter of fact, current measurements mildly suggest that $N_{\rm eff,BBN}$ be greater than $N_{\rm eff,CMB}$ by $\sim 1\sigma$ [138, 139, 140, 75].

In ΛCDM, where there are only three SM neutrino species all the time, $N_{\rm eff,BBN}(a) = N_{\rm eff,standard} = 3.046$. In contrast, in ΛSFDM, SFDM has an EOS which evolves over time, affecting the expansion rate during BBN if SFDM is relativistic then, and will hence contribute to $N_{\rm eff,BBN}(a) \equiv N_{\rm eff,standard} + \Delta N_{\rm eff,BBN}(a)$ as an extra relativistic component, as we pointed out in §2.3.4 and in Paper I. In addition, the inflationary SGWB which we have included self-consistently, amplified by the earlier stiff-SFDM-dominated era, also adds to $\Delta N_{\rm eff,BBN}(a)$, so it must be taken into account as well. In fact, in a ΛSFDM model with the SGWB, we infer $N_{\rm eff,BBN}(a)$ between $a_{\rm n/p}$ and $a_{\rm nuc}$, from the energy density fractions of relativistic SFDM, $\Omega_{\rm SFDM}$, and the GWs, $\Omega_{\rm GW}$. Both are sources to $\Delta N_{\rm eff,BBN}(a)$,

$$\frac{\Delta N_{\rm eff,BBN}(a)}{N_{\rm eff,standard}} = \frac{\Omega_{\rm SFDM}(a) + \Omega_{\rm GW}(a)}{\Omega_{\nu}(a)}, \tag{2.87}$$

where $\Omega_\nu(a)$ denotes the energy density fraction of the SM neutrinos. The evolution of $N_{\mathrm{eff,BBN}}(a)$ for one example ΛSFDM model has been shown in the right-hand plot of Fig. 2.3.

We compare the $N_{\mathrm{eff,BBN}}(a)$ obtained this way to the measured value given by Eq. (2.86), and impose on it a conservative threshold that throughout BBN (from $a_{\mathrm{n/p}}$ to a_{nuc}), it shall be within the 1σ confidence interval of the measured value. In Eq. (2.87), both values of $\Omega_{\mathrm{SFDM}}(a)$ and $\Omega_{\mathrm{GW}}(a)$ are controlled by the properties of SFDM, i.e., its particle parameters m and $\lambda/(mc^2)^2$, once the values of r and T_{reheat} are fixed, as described in §2.3.4.2. Therefore, the constraint on $N_{\mathrm{eff,BBN}}(a)$ will again translate as a constraint on the SFDM particle parameter pair $(\lambda/(mc^2)^2,\ m)$.

Eq. (2.87) shows that, for fixed r and T_{reheat}, if the stiff phase of SFDM ends too late into the BBN epoch, the considerable amount of $\Omega_{\mathrm{SFDM}}(a)$ can lead to too large an $N_{\mathrm{eff,BBN}}(a)$ which violates its measured value given by Eq. (2.86). In addition, the later the stiff-to-radiationlike transition of SFDM is, the larger the amplified $\Omega_{\mathrm{GW}}(a)$ is, increasing the value of $N_{\mathrm{eff,BBN}}(a)$ as well. Therefore, any change in the stiff-to-radiationlike transition point affects both $\Omega_{\mathrm{SFDM}}(a)$ and $\Omega_{\mathrm{GW}}(a)$ in the same direction. In order for this transition to finish early enough that the sum of $\Omega_{\mathrm{SFDM}}(a)$ and $\Omega_{\mathrm{GW}}(a)$ should observe the $+1\sigma$ confidence limit of $N_{\mathrm{eff,BBN}}$, there must be a lower bound on m, for any allowed value of $\lambda/(mc^2)^2$.

The radiationlike "plateau" of SFDM (see §2.3.4), as well as its stiff-to-radiationlike transition, is subject to the BBN constraint. If the plateau overlaps BBN, i.e., SFDM is well into its radiationlike phase by a_{nuc}, then $\Omega_{\mathrm{SFDM}}(\mathrm{plateau})$ during the plateau, as a function of $\lambda/(mc^2)^2$, must comply with the constraint on $N_{\mathrm{eff,BBN}}(a)$ according to Eq. (2.87). In particular, for large enough m, the stiff phase of SFDM ends so early that not

only the radiationlike phase of SFDM would enclose BBN, but also the amplification of the inflationary SGWB be insignificant, which leads to $\Omega_{\rm GW}(a) \simeq 0$. In this limit, the constraint from BBN amounts to a constraint on the value of $\Omega_{\rm SFDM}$(plateau), and hence on $\lambda/(mc^2)^2$ alone. The BBN constraint can thereby be analyzed the same way as in Paper I, for the case without GWs. We will not repeat that analysis here but just write down the result as follows:

$$2.3 \times 10^{-18}\ {\rm eV}^{-1}\ {\rm cm}^3 \leq \frac{\lambda}{({\rm mc}^2)^2} \leq 4.1 \times 10^{-17}\ {\rm eV}^{-1}\ {\rm cm}^3, \tag{2.88}$$

for ΛSFDM models in which the SGWB from inflation is negligible, and the radiationlike phase of SFDM overlaps BBN. The lower and upper bounds on $\lambda/(mc^2)^2$ in the equation above correspond to the -1σ and $+1\sigma$ confidence limits of the measured value of $N_{\rm eff,BBN}$ given by Eq. (2.86), respectively. The difference between Eq. (2.88) and the equivalent bounds in Paper I only reflects our update on the measured value of $N_{\rm eff,BBN}$.

If $\lambda/(mc^2)^2$ is less than the lower bound in Eq. (2.88), the SFDM plateau alone cannot make up a $\Delta N_{\rm eff,BBN}(a)$ which meets the -1σ confidence limit of its measured value. Therefore, for any of these smaller values of $\lambda/(mc^2)^2$, there must be an upper bound on m, which sets a constraint on how early the stiff phase can end, so that the sum of $\Omega_{\rm SFDM}(a)$ and $\Omega_{\rm GW}(a)$ can be substantial enough to reach the -1σ limit of $N_{\rm eff,BBN}$.

These constraints from $N_{\rm eff,BBN}$ on the allowed ranges of $(\lambda/(mc^2)^2,\ m)$ can also be illustrated in the SFDM particle parameter space plots, Figs. 2.5 and 2.6, for a wide range of r and $T_{\rm reheat}$. In the upper plot of Fig. 2.5, we show the result for the case without GWs (i.e., setting $\Omega_{\rm GW}(a) = 0$ in Eq. [2.87]), which can be compared to our previous result on the corresponding allowed region in Paper I. The bounds given by Eq. (2.88) are also reflected in Figs. 2.5 and 2.6, as described in §2.4.3. There we will discuss in more details

the allowed region due to the $N_{\rm eff,BBN}$ constraint in the SFDM particle parameter space and its dependence on the values of r and $T_{\rm reheat}$.

2.4.3 Results: allowed SFDM particle parameter space

Combining the constraints from the two cosmological observables described above, we can confine the allowed values of the SFDM particle parameters, $(\lambda/(mc^2)^2, m)$, in the two-dimensional parameter space, for various choices of r and $T_{\rm reheat}$ (see Figs. 2.5 and 2.6 for the parameter space plots).

In both figures, the constraints from $z_{\rm eq}$ and $N_{\rm eff,BBN}$ are expressed by curves of critical parameter values that marginally satisfy the respective constraints. Specifically, in each plot, the constraint from $z_{\rm eq}$ is indicated by the dash-dotted curve, and the region above this curve is allowed by the -1σ confidence limit of the measured value of $z_{\rm eq}$, given by Eq. (2.83). The solid curve refers to the constraint from the $+1\sigma$ confidence limit of $N_{\rm eff,BBN}$ at $a_{\rm n/p}$, and the dashed curve to the constraint from the -1σ confidence limit of $N_{\rm eff,BBN}$ at $a_{\rm nuc}$, given by BBN measurements (see Eq. [2.86]). The region below the solid curve and above the dashed curve is consistent with the 1σ confidence interval of the measured value of $N_{\rm eff,BBN}$ throughout BBN (see the right-hand plot of Fig. 2.3 for reference). The arrows in each plot indicate the directions in which the values of the SFDM particle parameters can satisfy the respective constraints, which result in the shaded region that denotes the overall allowed range of the SFDM particle parameters, satisfying all cosmological constraints.

Fig. 2.5 is a blow-up of Fig. 2.6. It shows the comparison between the case which does not include GWs in the evolution of ΛSFDM (the upper plot) so the values of r and $T_{\rm reheat}$ are not important, as studied in Paper I, and the case in which the SGWB from inflation is

self-consistently included (the lower plot), which we study in this paper. In the upper plot, the constraint from $z_{\rm eq}$ is given by the upper bound on $\lambda/(mc^2)^2$ in Eq. (2.85), indicated by the vertical dash-dotted line: the half-plane on its left side is allowed. In the lower plot, the corresponding critical curve takes the same vertical line but pivots at a minimum value of m and provides a lower bound on m for every value of $\lambda/(mc^2)^2$ below its upper bound. This change is due to the inclusion of the inflationary SGWB, which contributes a radiation component at $z_{\rm eq}$, as explained in §2.4.1. In both the upper and lower plots of Fig. 2.5, it is easily seen that for large enough m, the parameter values ($\lambda/(mc^2)^2$, m) allowed by the $N_{\rm eff,BBN}$ constraint indeed correspond to models in which the radiationlike phase of SFDM overlaps BBN and the effect from the SGWB is negligible, so that the value of $\lambda/(mc^2)^2$ must be bounded between the asymptotic vertical solid and dashed lines given by Eq. (2.88), as explained in §2.4.2. In this limit, the allowed region in the lower plot becomes indistinguishable from the one in the upper plot, since the SGWB makes no difference to the background evolution of the universe.

Multiple cases are plotted in Fig. 2.6, with different choices for r and $T_{\rm reheat}$. In every panel, the overall allowed region for the SFDM particle parameters is given by combining all the cosmological constraints, leaving the shaded area. In the above and middle panels, i.e., the four cases with $r = 0.01$ or either 0.1, and $T_{\rm reheat} = 1$ GeV or either 100 GeV, the shaded regions are nearly indistinguishable from one case to another. This reflects the fact that if the reheat temperature is too low, the stiff era is then too short to boost the inflationary SGWB to a considerable degree. In this situation, the allowed range of SFDM particle parameters simply reduces to that in the "no GWs" case as shown in Fig. 2.5. Reheat temperatures $T_{\rm reheat} \gtrsim 10^3$ GeV start to make differences to the allowed regions, as

shown in the bottom two panels of Fig. 2.6, where the allowed regions for $T_{\rm reheat} = 10^3,\ 10^6$ and 10^9 GeV are plotted together and overlap. In these cases, they are significantly affected by the SGWB from inflation. The larger the energy density of the SGWB amplified by the stiff era, resulting from an increase in either the value of r or $T_{\rm reheat}$, the more stringent the constraints on the SFDM particle parameters, as one should expect. In fact, for fixed $T_{\rm reheat}$, the allowed region contracts slightly when the value of r increases from $r = 0.01$ to 0.1. Its dependence on the value of r is found to be relatively weak. On the other hand, however, for fixed r, the allowed region shrinks significantly every time $T_{\rm reheat}$ increases by a factor of 1000. We find that, for given values of r, for $T_{\rm reheat} \gtrsim 10^3$ GeV, the minimum value of the SFDM particle mass, $m_{\rm min}$, among the models which satisfy all the cosmological constraints, is proportional to $T_{\rm reheat}$. For $r \gtrsim 0.01$, the dependence of $m_{\rm min}$ on both r and $T_{\rm reheat}$ can be empirically expressed as

$$m_{\rm min} \simeq (5 \times 10^{-21}\ {\rm eV}/c^2) \times \begin{cases} \dfrac{T_{\rm reheat}}{10^3\ {\rm GeV}}\sqrt{\dfrac{r}{0.01}}, & T_{\rm reheat} \gtrsim 10^3\ {\rm GeV}, \quad (2.89) \\ 1, & T_{\rm reheat} < 10^3\ {\rm GeV}. \quad (2.90) \end{cases}$$

2.5 Results: present-day SGWB energy density spectrum and its detectability by LIGO

In the ΛSFDM model, the integrated inflationary SGWB energy density predicted in §2.3 contributes only a small fraction of the total energy density today, $\Omega_{\rm GW}(a = 1) \sim 10^{-8} - 10^{-7}$. As such, its effect on the universe today is negligible. Remarkably enough, however, in its spectrum at high frequencies where amplification by the stiff-SFDM-dominated era was greatest, which can overlap the range of GW laser interferometer experiments, the amplitude can be significant enough to be detectable. We demonstrate this here, in light of

the SGWB energy density spectrum predicted in §2.3 and the cosmological constraints on the SFDM particle parameters derived in §2.4, by analyzing the detectability of the amplified inflationary SGWB at the present by current and future laser interferometer experiments, as a unique signature of the ΛSFDM model.

The expansion history of the ΛSFDM universe described in §2.3.4 is imprinted in the present-day energy density spectrum of the SGWB from inflation, $\Omega_{\rm GW}(f)$, defined as follows:

$$\Omega_{\rm GW}(f) \equiv \Omega_{\rm GW}(k = 2\pi f/c, a = 1). \tag{2.91}$$

For each mode whose (comoving) frequency is f, there corresponds an epoch of horizon reentry at $a_f \equiv a_{k=2\pi f/c}$, which determines the outcome of the cosmic evolution of its $\Omega_{\rm GW}(f)$ to the present-day, as described in §2.3.2. For different SFDM model parameters and values of $T_{\rm reheat}$ and r, there is a different mapping between f and a_f. This is illustrated in Fig. 2.7. In general, as long as the Hubble radius increases with time, as it does from the end of inflation to the end of matter-domination when the cosmological constant begins to dominate afterward, a_f increases as f decreases. For $a_f > a_{\rm eq}$ (or $f < f_{\rm eq} \sim 10^{-17}$ Hz, the dependence of a_f on f is universal, since the expansion history of ΛSFDM is the same as that of ΛCDM. The maximum a_f in all example models corresponds to the moment when modes begin to exit, instead of reentering the horizon, once $w = -1/3$ for the EOS of the background universe. From this moment on, all modes that are still outside the horizon will never reenter the horizon, as the cosmological-constant-dominated era begins. On the other hand, toward the high-frequency end, manifest distinctions arise for a_f earlier than the end of the stiff-SFDM-dominated era, among the three example ΛSFDM models. We note that, since the dependence of f on a_f is different in ΛSFDM from its dependence in ΛCDM, for $a_f < a_{\rm eq}$,

so will the dependence of f on the photon temperature $T(a)$ at $a = a_f$ be different. For ΛCDM, we can write $f \approx 10^{-4}\text{Hz}\frac{\text{T}(\text{a}_\text{f})}{10^3\text{GeV}}$, for $a_{\rm reheat} < a_f < a_{\rm eq}$ [120], while this is not true for ΛSFDM. For example, as seen in Fig. 2.7, for the example model in which $T_{\rm reheat} = 2 \times 10^4$ GeV, $f \approx 40$ Hz at $T(a_f) = T_{\rm reheat}$.

We begin by presenting the present-day SGWB energy density spectra, $\Omega_{\rm GW}(f)$, for three example ΛSFDM models, to guide our discussion. In §2.5.1 below, we will use these models to explain the generic features of the inflationary SGWB spectra in relation to that in ΛCDM and in relation to the current and future GW detection experiments. In §2.5.2, we will revisit these illustrative models as we quantify the detectability of the SGWB in ΛSFDM as a function of the SFDM particle parameters, for given values of r and $T_{\rm reheat}$. In the upper plots of Figs. 2.8 – 2.10, we show the present-day SGWB energy density spectra of the same example ΛSFDM models shown in Fig. 2.7. For all three models shown in this section, the values of $\lambda/(mc^2)^2$ are fixed according to Eq. (2.81) such that the corresponding core size of an SFDM halo is ~ 0.8 kpc due to the repulsive self-interaction of SFDM. We also hold the value of $r = 0.01$ fixed for all these models, for the purpose of comparison. For $T_{\rm reheat}$, in contrast to the choices in §2.3.4, we here choose $T_{\rm reheat} = 10^3,\ 2\times10^4$, and 10^6 GeV, such that the span of corresponding $f_{\rm reheat}$, the frequency of the mode that reenters the horizon at the end of reheating at $a_{\rm reheat}$, is nearly centered on the LIGO sensitive frequency band ($20 - 86$ Hz) [142]. [14] The SFDM particle mass m is different for each value of $T_{\rm reheat}$, as labeled. The particular choice of m values will be described below in §2.5.2; all ΛSFDM models shown in

[14]This LIGO sensitive band is defined as the range which includes 99% of the signal for a *flat* spectrum. This range is dependent on the assumed shape of the SGWB spectrum, however. For power-law spectra $\Omega_{\rm GW}(f) \propto f^\beta$, the range is different for different values of β. For $\beta = 2/3$ (or 3), for example, this range shifts to $20 - 98$ (or 305) Hz, respectively.

Figs. 2.8 – 2.10 satisfy all of the cosmological constraints described above in §2.4. We will first describe the shape of $\Omega_{\rm GW}(f)$ for the example models and the respective detectabilities of their SGWBs, with special emphasis on the Advanced LIGO/Virgo experiment.

2.5.1 Generic features of the present-day energy density spectrum $\Omega_{\rm GW}(f)$ of the inflationary SGWB and its detectability

As derived in §2.3.2.3, the generic energy density spectrum $\Omega_{\rm GW}(f)$ of the primordial SGWB from inflation, predicted by ΛSFDM models, must be approximately piece-wise power laws, the power indices of which are determined by the EOS parameters $w = p/\rho$ of the universe throughout all eras in the expansion history. In particular, if we neglect the very weak dependence on the primordial tensor index n_t (i.e. set $n_t = 0$), then $\Omega_{\rm GW}(f) \propto f^{-2}$ for modes which reenter the horizon during the matter-dominated era, after $z_{\rm eq}$. For modes which reenter the horizon earlier than $z_{\rm eq}$, during the radiation-dominated era, $\Omega_{\rm GW}(f) \propto f^0$. These two power laws actually apply to the $\Omega_{\rm GW}(f)$ predicted by ΛCDM, as well, as indicated by the green curve in the upper plot of, e.g., Fig. 2.8. There, $\Omega_{\rm GW}(f)$ exhibits a long plateau ($\propto f^0$) over a frequency range which covers the bands of most GW experiments at the present, e.g., aLIGO/Virgo and the LISA mission. The amplitude of this plateau depends on the value of r alone, independent of f (see, e.g., [143]). For $r = 0.01$ shown here, this amplitude is $\sim 10^{-16}$, more than six orders of magnitude below the sensitivities of current GW detectors, which is the main reason why the SGWB from inflation (in ΛCDM) was not expected to be detectable by current major GW detection experiments listed in §2.1.4.

However, we will now show that the SGWB from inflation, predicted by the ΛSFDM model, has the potential to be detectable by current GW experiments like aLIGO/Virgo, i.e.,

can reach their detection sensitivities for a wide range of model parameters, due to the amplification of the SGWB during the stiff-SFDM-dominated era. Its present-day energy density spectra $\Omega_{\rm GW}(f)$ are indicated by purple curves in Figs. 2.8 – 2.10. These show that the SGWB spectrum for ΛSFDM departs dramatically at high frequencies from that of standard ΛCDM: $\Omega_{\rm GW}(f) \propto f^1$ for modes reentering the horizon during the stiff-SFDM-dominated era, while $\Omega_{\rm GW}(f) \propto f^{-2}$ for modes reentering even earlier, during the reheating era (corresponding to even higher frequencies). Therefore, $\Omega_{\rm GW}(f)$ in ΛSFDM models, amplified by the stiff era, has a characteristic triangle-shaped feature at high frequencies, peaked at $f_{\rm reheat}$. [15] The baseline of this triangle sits on the plateau which corresponds to modes that reenter the horizon during RD, and highly overlaps the long plateau for the ΛCDM model mentioned above, as shown in Figs. 2.8 – 2.10.

In Figs. 2.8 – 2.10, we display a comprehensive collection of previous constraints on the cosmological SGWB, from various types of observations. Specifically, ranging from lowest to highest frequencies, they are from the BICEP2/Keck Array CMB polarization experiment [114], pulsar timing array (PTA) experiments (NANOGrav [121], PPTA [122], EPTA [123]), and the (initial, pre-2015) LIGO experiment [144, 145]. All three example models shown here satisfy all these constraints on the SGWB. In fact, these constraints are weaker than the ones from $z_{\rm eq}$ and BBN discussed in §2.4. Therefore, we do not utilize them to constrain the SFDM particle parameters. However, the frontier laser interferometer experiments, aLIGO/Virgo [119, 142], in operation today, and LISA [120] (currently in its Pathfinder stage) in the future, are capable of placing much better and more useful constraints on the inflationary

[15] In Figs. 2.8 – 2.10, the discontinuity in $\Omega_{\rm GW}(f)$ at $f_{\rm reheat}$ is due to the fact that we assume an instantaneous change of the EOS at the end of reheating, from $w = 0$ to $w = 1$, in our ΛSFDM model. We will adopt a more realistic model for reheating in the future, in which w changes smoothly.

SGWB, or quite possibly even *detecting* it. In fact, as we shall show below, the new data from the O1 run of aLIGO, recently reported in [142], should already be sensitive enough to detect the strongest possible signals predicted by our ΛSFDM model for a limited range of model parameters. This will allow us here to place the first meaningful constraints on the model which are based upon this new observable. With regard to the future, the curve in Figs. 2.8 – 2.10 labeled "eLISA" is the expected strain noise function of eLISA in [146] and may be revised in the final design of the upcoming LISA mission. If $\Omega_{\rm GW}(f)$ is higher than (i.e., intersects) this noise sensitivity curve, it is possible for LISA to detect this SGWB.

In this paper, we concentrate mostly on the detectability of the SGWB from inflation by the ongoing aLIGO/Virgo experiment, whose O1 run has so far detected several GW signals from binary black hole merger events, as reported in [134]. This same experiment can also detect a stochastic background (i.e. either of diffuse origin or from unresolved sources), but that requires a different strategy for analyzing the data, by considering the correlation of the strains measured by different detectors. That is one of the major, additional goals of the experiment [119], in fact. As mentioned above, the first results of analyzing the O1 data run to search for the SGWB were presented just recently in [142]. Although the present-day SGWB, were it detected by aLIGO/Virgo, could have a variety of origins other than the primordial SGWB from inflation, such as unresolved black hole mergers [119], we will only consider the inflationary SGWB in this paper, which has a unique spectral shape in $\Omega_{\rm GW}(f)$ as predicted by ΛSFDM, and probe its detectability characterized by the SNR.

As shown by [147], the SNR of any fixed SGWB today, for a certain laser interferometer experiment, is proportional to the square root of the accumulated observation time. Therefore, we can in principle enhance the detectability of a reasonably-motivated SGWB

to a required level of significance, provided enough observation time. The solid and dashed curves in the upper plots of Figs. 2.8 – 2.10, labeled by "aLIGO/Virgo", indicate the "integrated 1σ sensitivity curves" for detecting the inflationary SGWB predicted by ΛSFDM, for the two observing runs O1 (with data now analyzed) and O5 (theoretical forecast), respectively. The calculation of these curves is described in Appendix B.4, based upon a modification of the "power-law integrated (PI) sensitivity curves" developed by [148] as a handy tool for visualizing the sensitivity of GW detectors for $\Omega_{\rm GW}(f)$ spectra which are assumed to be pure power-laws (for which we are grateful to Joseph Romano for letting us modify his code). The latter, for example, includes the case thought to describe the background from unresolved binary black hole mergers (i.e. power-law index 2/3, up to a turn-over frequency). The power-law assumption underlying the PI curves is an approximation that reflects the fact that the frequency band of greatest sensitivity of aLIGO/Virgo is narrow. However, in our case, the strong triangle feature of the spectrum is not amenable to approximation as a single power-law, so we have used the actual non-power-law shape of the SGWB for our ΛSFDM model in producing the curves in Figs. 2.8 – 2.10, instead. In our case, the way to interpret the integrated sensitivity curves is the following: if the predicted $\Omega_{\rm GW}(f)$ for the inflationary SGWB from a given set of ΛSFDM model parameters touches the curve for the O1(O5) run at any f, this SGWB will be detected with 1σ significance (SNR = 1) by the O1(O5) run, respectively. [16] The dashed curve (O5) is much lower than

[16] We note that this interpretation of the integrated sensitivity curves differs from that used to interpret the PI curves for pure power-law spectra. For the latter spectra, the interpretation is as follows: for each point on the PI sensitivity curve, a spectrum which is tangent to the curve at that point (for which the power-law index is given by the slope of the tangent to the curve at that point) would be detected at 1σ significance (SNR = 1), or a confidence level of 68%. Hence, a single sensitivity curve encodes the detectability for a range of spectral indices at once.

the solid curve (O1) (i.e. can detect a smaller $\Omega_{\rm GW}(f)$), which reflects the fact that the design sensitivity of O5 is higher and the integration time is longer than those of O1. These curves are calculated by integrating $\Omega_{\rm GW}(f)$ over frequency, convolved with the LIGO strain sensitivity, which is concentrated in the $20-86$ Hz band (see footnote 13, page 33).

For the SGWB from standard inflation, which is enhanced in ΛSFDM, its predicted $\Omega_{\rm GW}(f)$ has a triangle-shaped feature as described above, by which $\Omega_{\rm GW}(f)$ can possibly reach the aLIGO/Virgo sensitivity curves, an impossible task for the corresponding inflationary SGWB in ΛCDM (see Figs. 2.8 – 2.10 and [143]). To see this in more detail, there are three cases for our predicted $\Omega_{\rm GW}(f)$, with regard to the position of the peak of the triangle in $\Omega_{\rm GW}(f)$, at $f_{\rm reheat}$, relative to the narrow frequency band of peak sensitivity of aLIGO/Virgo, $20-86$ Hz. These cases can be expressed as:

Case 1. $f_{\rm reheat} < 20$ Hz,

Case 2. 20 Hz $< f_{\rm reheat} < 86$ Hz,

Case 3. $f_{\rm reheat} > 86$ Hz.

We choose the values of $T_{\rm reheat} = 10^3,\ 2\times10^4,\ 10^6$ GeV, in the three example models shown here, such that each of them fits one of the above three cases, respectively. Intuitively, one should expect that among these three models, for which the peak amplitudes $\Omega_{\rm GW}(f_{\rm reheat})$ are all approximately equal, the maximally detectable model, i.e., the one with the highest SNR for a given observation time, must be the one with $T_{\rm reheat} = 2\times10^4$ GeV that fits Case 2, where $f_{\rm reheat}$ lies inside the peak sensitivity band of LIGO. Indeed, this is shown to be true by the SNR plots of Figs. 2.8 – 2.10, for the SNR from the SGWB predicted by

ΛSFDM vs. the accumulated observation time of aLIGO/Virgo. [Note: These plots can be compared to the right panel of Fig. 1 in [119], except that the latter are based upon assuming a spectrum appropriate for a model of the background from unresolved binary black hole mergers and the SNR there is based upon the theoretical forecast for all observing runs O1 through O5, while in Figs. 2.8 – 2.10 we use the noise characteristics of the actual O1 data, as we describe in Appendix B.4, and only use the theoretical forecast for O2 through O5.] From Fig. 2.9 we see that if $T_{\rm reheat} = 2 \times 10^4$ GeV and $r = 0.01$, the expected SNR should already have achieved a value greater than 10, by the end of the recent O1 run, for this SFDM parameter choice $(\lambda/(mc^2)^2,\ m) = (10^{-18}\ \mathrm{eV}^{-1}\mathrm{cm}^3,\ 1.6 \times 10^{-19}\ \mathrm{eV}/c^2)$. Consequently, a nondetection of the SGWB by aLIGO O1 would rule out this example case. On the other hand, consider the case in Fig. 2.10, instead, where the values of r and $\lambda/(mc^2)^2$ are the same but $T_{\rm reheat} = 10^6$ GeV and $m = 8 \times 10^{-18}\ \mathrm{eV}/c^2$. While its expected SNR is less than 1 for O1, even this case will reach an SNR ~ 30 by the end of O5 in 2022. Apparently, a wider range of SFDM parameters and reheat temperatures than that to which aLIGO O1 is sensitive will be accessible by the end of the aLIGO/Virgo O5 run.

This shows that the ΛSFDM model promises to be detectable via its predicted SGWB from inflation, or else will be seriously constrained with regard to its particle parameters, over the course of the ongoing aLIGO/Virgo experiment. We will quantify this in more detail below in §2.5.2. There, we shall go beyond the three example cases above, by considering the expected SNR for a range of cases and include an analysis of the data accumulated in the O1 run to determine which of these cases are either consistent with the data or else already excluded by it.

2.5.2 Implications from ΛSFDM models marginally satisfying cosmological constraints

The total $\Omega_{\rm GW}(a = 1)$ at the present, integrated over all frequencies, is equal to the total area underneath the spectrum curve $\Omega_{\rm GW}(f)$. As we confirm, this total area is dominated by the area of the triangle for a wide range of ΛSFDM model parameters, including all three example models shown here. For these models, r and $\lambda/(mc^2)^2$ are fixed as described at the beginning of §2.5, but $T_{\rm reheat}$ is different in each model, and for each $T_{\rm reheat}$, the SFDM particle mass m is adjusted to be the marginal value such that all the example models satisfy the current cosmological constraints derived in §2.4. For other given values of r and $\lambda/(mc^2)^2$, the marginally-allowed ΛSFDM models can be defined similarly, as follows. For fixed values of r and $\lambda/(mc^2)^2$, there is a family of marginally-allowed cases for different values of $T_{\rm reheat}$. For each value of $T_{\rm reheat}$, the value of m is adjusted to match the lower bound of the vertical shaded region of allowed mass values in Fig. 2.6. This value of m serves to maximum the predicted value of $\Omega_{\rm GW}(f)$ amongst the allowed cases for which the other parameters are the same. In this subsection, we will study the detectability of these marginal ΛSFDM models.

First, among all ΛSFDM models which satisfy the cosmological constraints, these marginal ones have the highest detectability. This can be shown by decreasing m but fixing all other parameters in an allowed model, until m reaches its lower bound. During this procedure, SFDM ends its stiff phase later, while the beginning of the stiff phase does not change for fixed $T_{\rm reheat}$, so the duration of the stiff-SFDM-dominated era becomes prolonged. As a result, the SGWB experiences more boost, and $\Omega_{\rm GW}(f)$ has higher amplitudes in the triangle, i.e., for modes which reenter the horizon by the end of the stiff era. This leads

to a larger SNR of $\Omega_{\rm GW}(f)$ measured by aLIGO/Virgo. Therefore, the marginally-allowed ΛSFDM models, which includes the three example models here, are motivated by the fact that they maximize the detectability of the predicted SGWB today and, hence, are the best starting point for comparison with the data.

In the upper plots of Figs. 2.8 – 2.10 for these models, as $T_{\rm reheat}$ changes from 10^3 GeV to 10^6 GeV, the peak frequency of the spectrum at $f_{\rm reheat}$ shifts from low to high, passing through the $20-86$ Hz sensitive band of aLIGO/Virgo, whereas the peak amplitude $\Omega_{\rm GW}(f_{\rm reheat})$, and thus the area of the triangle in $\Omega_{\rm GW}(f)$, remains almost the same. This is not surprising, because for these marginally-allowed models with the same values of r and $\lambda/(mc^2)^2$, they must produce approximately the same amount of $\rho_{\rm GW}$ of the SGWB, at epochs which correspond to the cosmological constraints. Therefore, the corresponding total $\Omega_{\rm GW}$ at the present is nearly the same for all marginal models, dominated by the area of the triangle in $\Omega_{\rm GW}(f)$, as mentioned above. Interestingly, we find that $f_{\rm reheat}$ is nearly proportional to $T_{\rm reheat}$ among these marginally-allowed models. We provide an analytical explanation for this relation in Appendix B.3.

Although the total present-day $\Omega_{\rm GW}$ is almost constant for all marginal models, the detectability of their predicted SGWB, by aLIGO/Virgo, is highly distinguishable from one model to another (see lower plots of Figs. 2.8 – 2.10). As we discussed in §2.5.1, this is apparently due to the narrowness of the LIGO sensitive frequency band and the strong dependence on $f_{\rm reheat}$ of the overlap between this band and the peak of the SGWB spectrum. The maximally detectable case, with the largest expected SNR, is when $f_{\rm reheat}$ lies inside this window. Therefore, among the marginally-allowed ΛSFDM models with fixed r and $\lambda/(mc^2)^2$, we can maximize the predicted SGWB signal by tuning $T_{\rm reheat}$ (and with it, the

corresponding marginally-allowed value of m) so as to center $f_{\rm reheat}$ on the LIGO sensitive band. Among the three example models, the most detectable is that with $T_{\rm reheat} = 2 \times 10^4$ GeV. We can plot the dependence of the expected SNR on $T_{\rm reheat}$ for a given family of marginally-allowed ΛSFDM models with constant r and $\lambda/(mc^2)^2$, and locate the value of $T_{\rm reheat}$ which corresponds to the maximally detectable model. For illustrative purposes, we choose one set of values, $r = 0.01$ and $\lambda/(mc^2)^2 = 1 \times 10^{-18}$ eV^{-1}cm^3, and plot this dependence of the SNR on $T_{\rm reheat}$ in Fig. 2.11.

As seen in Fig. 2.11, for both the aLIGO/Virgo O1 and O5 runs, the expected SNR has a peak between $T_{\rm reheat} = 10^4$ GeV and 10^5 GeV, which corresponds to the most sensitive (lowest strain noise) frequency range of the experiment. For $r = 0.01$, which is still 7 times below the current upper bound from CMB polarization measurements, the maximally detectable ΛSFDM model has an expected SNR > 10 even for the completed O1 run. After 2 years of the future O5 run, the same model can reach an SNR greater than 1000. These SNRs would increase or decrease if we assumed values of r which are larger or smaller than this, respectively. This establishes, however, that the ΛSFDM model is capable of producing a detectable signal for the SGWB for some range of model parameters.

Now that the O1 run is finished, we can use the data to compare with these predictions. As of yet, no detection of the SGWB has been reported for the O1 run [142]. The significance of a null detection depends upon the assumed spectrum of $\Omega_{\rm GW}(f)$, so the confidence level (C.L.) of this null detection is model-dependent. [142] has analyzed the data for power-law spectra, $\Omega_{\rm GW}(f) = \Omega_\beta (f/f_{\rm ref})^\beta$, where $f_{\rm ref} = 25$ Hz, and reported 95% C.L. upper limits for Ω_β as a function of β. In their Table 1, for example, they report this upper limit for $\beta = 0$ as $\Omega_\beta \leq 1.7 \times 10^{-7}$. The analysis in [142] did not extend to models like

ours in which the spectrum is not a pure power-law, but is rather a broken power-law which defines the triangle feature we have described above, which peaks at a frequency determined by the value of $T_{\rm reheat}$. However, as shown in Fig. 2.11, when the value of $T_{\rm reheat}$ is chosen so that $f_{\rm reheat}$ is outside the range of the LIGO sensitive band (i.e. Case 1 when $f_{\rm reheat} < 20$ Hz, Case 3 when $f_{\rm reheat} > 86$ Hz), the SNR is roughly the same as it would be for the power-law spectrum with the same slope as the corresponding side of the triangle feature (i.e. $\beta = -2$ or 1 for Cases 1 and 3, respectively). These spectral indices for Cases 1 and 3 are within the range of the spectral indices for which the analysis in [142] reports a null detection. This indicates that if the data were analyzed for our predicted spectrum in Cases 1 and 3, a null detection would also be reported.

This fact allows us to place a meaningful constraint on a range of ΛSFDM model parameters. For the illustrative cases shown in Fig. 2.11, for example, the signal predicted by those marginally-allowed model parameters can be so strong that some of those model parameters can already be excluded at some C.L. by the null detection reported in [142]. As shown by the horizontal lines drawn across the SNR plot in Fig. 2.11 for the O1 run, each corresponding to a different constant value of SNR, there are two points on each horizontal line which intersect the curve of SNR vs. $T_{\rm reheat}$, one on each side of the peak SNR. For all values of $T_{\rm reheat}$ between these two points, the SNR is larger than it is at the two points. A null detection that implies a 95% C.L. upper limit (SNR = 2) means that the ΛSFDM model parameters for the marginally-allowed cases with those values of $T_{\rm reheat}$ and all the points in between are inconsistent with the data at the 95% C.L. For the illustrative cases plotted in Fig. 2.11, the marginally-allowed ΛSFDM models for which $r = 0.01$ and $T_{\rm reheat}$ ranges between about 8.75×10^3 and 1.7×10^5 GeV (for which the corresponding masses are in the

range between 7×10^{-20} and 1.36×10^{-18} eV/c^2), are excluded at the 95% C.L., based upon the O1 data. **This provides a new kind of cosmological constraint on the ΛSFDM model.**

On the other hand, as aLIGO/Virgo improves its sensitivity and accumulates more data over time from O1 to O5, the expected SNR of the SGWB predicted by any given ΛSFDM model will also increase. As a result, by the end of the final observing run O5, ΛSFDM models with a wider range of parameters, which were not yet detectable by the O1 run, will become accessible. In particular, the marginally-allowed models with $r = 0.01$ and $\lambda/(mc^2)^2 = 1 \times 10^{-18}$ eV^{-1}cm^3 predict an inflationary SGWB signal with an SNR > 3, by the end of O5, for those in which $T_{\rm reheat}$ lies approximately inside (6×10^2 GeV, 10^7 GeV), and the corresponding SFDM mass range is about (5×10^{-21} eV/c^2, 8×10^{-17} eV/c^2), as shown in Fig. 2.11. Table 2.2 summarizes the results for the ranges of $T_{\rm reheat}$ and the corresponding m for these marginally-allowed ΛSFDM models which are detectable by aLIGO/Virgo at 2σ or 3σ confidence levels by the end of its O1 and O5 runs, respectively. **These results demonstrate that, in the future, the ΛSFDM model has the great potential of having its signature imprint on the primordial SGWB from inflation detected by the Advanced LIGO/Virgo experiment.**

In conclusion, the ΛSFDM model shows a great prospect of detectability by the Advanced LIGO/Virgo experiment, thanks to its unique prediction of the present-day energy density spectrum of the primordial SGWB from inflation.

LIGO run	Epoch	$T_{\rm reheat}$/GeV (SNR >2)	$m/({\rm eV/c^2})$ (SNR >2)	$T_{\rm reheat}$/GeV (SNR >3)	$m/({\rm eV/c^2})$ (SNR >3)
O1	2015-2016	$(8.75\times10^3,\ 1.7\times10^5)$	$(7\times10^{-20},\ 1.36\times10^{-18})$	$(1.05\times10^4,\ 1.125\times10^5)$	$(8.4\times10^{-20},\ 9\times10^{-19})$
O5	2020-2022	$(5\times10^2,\ 1.5\times10^7)$	$(4\times10^{-21},\ 10^{-16})$	$(6\times10^2,\ 10^7)$	$(5\times10^{-21},\ 8\times10^{-17})$

Table 2.2: LIGO-detectable parameter ranges of $T_{\rm reheat}$ and m for ΛSFDM models with $r=0.01$ and $\lambda/(mc^2)^2 = 1\times10^{-18}$ eV^{-1}cm^3 that marginally satisfy the cosmological constraints, by the end of the O1 and O5 observing runs of aLIGO/Virgo, respectively. The detectable ranges for this illustrative family of models correspond to 2σ and 3σ detections, respectively. We note that the O1 run is now completed with a null detection, so the ranges for O1 can be interpreted as excluded at 95% and 99% confidence, respectively.

2.6 Discussion

2.6.1 What happens to ΛSFDM if $N_{\rm eff,BBN} \approx N_{\rm eff,standard}$?

In §2.4, we apply the cosmological observables, $z_{\rm eq}$ and $N_{\rm eff,BBN}$, to constrain the SFDM particle parameters, through constraining the background expansion history of the ΛSFDM universe. These constraints result in the allowed range of the parameters $(\lambda/(mc^2)^2, m)$, expressed as shaded region in the two-dimensional parameter space, as a function of the tensor-to-scalar ratio r and the reheat temperature $T_{\rm reheat}$, (see Figs. 2.5 and 2.6). We adopt conservative thresholds, the 1σ confidence intervals from measurements, for both the $z_{\rm eq}$ and $N_{\rm eff,BBN}$ constraints. These thresholds lead to the shapes of the allowed regions as thin stripes, for all cases. In particular, since the -1σ confidence limit of the measured value of $N_{\rm eff,BBN}$ in Eq. (2.86) is greater than the standard value, $N_{\rm eff,standard} = 3.046$, all of the allowed ΛSFDM models can explain a higher value of $N_{\rm eff}$ at BBN than at recombination, as mildly suggested by current measurements, mentioned in §2.4.2.

However, if we adopt a more relaxed threshold, e.g., the 2σ confidence interval, particularly for the $N_{\rm eff,BBN}$ constraint, we will allow a much broader range of ΛSFDM models which satisfy these cosmological constraints. In fact, the 2σ confidence interval of the mea-

sured value of $N_{\rm eff,BBN}$ contains the standard value $N_{\rm eff,standard}$ (see [139]). Therefore, there would be then no lower bound from the BBN constraint on the value of $\Delta N_{\rm eff,BBN}$ predicted by the ΛSFDM model. Only an upper bound on $\Delta N_{\rm eff,BBN}$ would be left, translated to a lower bound on m for any allowed value of $\lambda/(mc^2)^2$. As a result, the allowed ranges of $(\lambda/(mc^2)^2, m)$ illustrated in Figs. 2.5 and 2.6 would amount to the whole "quadrants" above the solid and dashed-dotted curves (for the $z_{\rm eq}$ constraint), free from the dashed curves. The quadrant regions, as opposed to the stripe-shaped shaded regions in Figs. 2.5 and 2.6, allow the $\lambda \to 0$ limit, in which SFDM is (nearly) non-self-interacting. This implies that while the non-self-interacting SFDM model is mildly disfavored by the 1σ confidence interval from current measurements of $N_{\rm eff,BBN}$, it is consistent with the 2σ limits.

Furthermore, should the measured value of $N_{\rm eff,BBN}$ decrease in the future to the extent of strongly favoring $N_{\rm eff,standard}$, the allowed ranges of SFDM particle parameters can be adjusted accordingly. In that case, the allowed regions in the parameter space would be like the quadrants described above.

2.6.2 SGWB from inflation versus that from unresolved binary black hole mergers?

Since LIGO has a narrow sensitive frequency band ($20 - 86$ Hz), for any potential SGWB signal, it is conventional to assume a power law for its present-day energy density spectrum, $\Omega_{\rm GW}(f)$, inside this band, and convolve this power-law spectrum with observational data to test this potential signal or to put an upper bound on it. This assumption is applicable to the SGWB from unresolved binary black hole mergers, since theoretical modeling suggests a power-law spectrum for such a signal, $\Omega_{\rm GW}(f) \propto f^{2/3}$, within the LIGO

band [119, 142]. However, the $\Omega_{\rm GW}(f)$ of the inflationary SGWB predicted by the ΛSFDM model has a unique triangle-like spectral shape as described in §2.5, for which the power-law based detection analysis may be invalid. In addition, by tuning the model parameters, the inflationary SGWB in ΛSFDM can achieve an amplitude within the LIGO band which is comparable to or much greater than that from known astrophysical sources. In Fig. 2.12, for example, we compare the current predictions for the SGWB from unresolved binary black hole mergers with the inflationary SGWB predictions of the ΛSFDM model for the three illustrative, marginally-allowed cases in Figs. 2.8 – 2.10. The SNR of the SGWB from unresolved binary black hole mergers is currently predicted to be less than 10 at 90% C.L. by the end of O5 (in 2022) [119], while in ΛSFDM, if, for example, we assume values of $r = 0.01$ and $\lambda/(mc^2)^2 = 1\times10^{-18}$ eV^{-1}cm^3, the expected SNR of the inflationary SGWB for the family of marginally-allowed cases ranges from ~ 3 to > 1000 by then, for $6\times10^2 < T_{\rm reheat}$ (GeV) $< 10^7$ (see Fig. 2.11 and Table 2.2). Therefore, it will be important for aLIGO/Virgo and future GW detection experiments to consider the SGWB from inflation predicted by the ΛSFDM model and develop a means of distinguishing this potential SGWB signal from that sourced by binary black hole mergers, e.g., via their different spectral shapes. For that reason, it will be interesting to consider the possibility of simultaneous detection of the SGWB in different frequency bands, as should be possible in the future with, for example, the LISA space-based mission, as we shall discuss below.

2.6.3 Future detectability of the SGWB from inflation in ΛSFDM with LISA?

We have briefly mentioned the prospective constraints on the present-day SGWB from the space laser interferometer mission LISA, currently in its Pathfinder stage, in §2.5.1. LISA

can potentially probe SGWB signals from various cosmological and astrophysical sources, in the milli-Hertz frequency range. According to our examples in Figs. 2.8 – 2.10, the SGWB from inflation in the ΛSFDM model is predicted to lie above the LISA design sensitivity curve for Case 1 values of $T_{\rm reheat}$. Therefore, the synergy between LISA and LIGO will prospectively provide crucial information about the spectral shape of $\Omega_{\rm GW}(f)$ over frequencies which span the bands of these two experiments, and thus the strongest constraint on the inflationary SGWB predicted by ΛSFDM, in terms of its triangle-shaped $\Omega_{\rm GW}(f)$ at high frequencies. In other words, if this signal is detected by both experiments and consistent with a ΛSFDM model, it will be a "smoking-gun" for SFDM and will determine its particle parameters as well as $T_{\rm reheat}$ to a good accuracy. On the contrary, if both experiments suggest null detection of any SGWB signal, it would place stringent constraints on the SFDM particle parameters and $T_{\rm reheat}$, in the context of the ΛSFDM model.

2.7 Summary and conclusion

We extended our analysis in Paper I of the cosmological evolution of a universe in which dark matter is comprised of ultralight self-interacting bosonic particles which form a Bose-Einstein condensate, described by a classical complex scalar field (SFDM) with a global $U(1)$ symmetry. In this case, the comoving particle density, or charge density, conserved after particle production during reheating, is large enough to account for all the dark matter, a form of asymmetric dark matter. Here we connect the evolution of the SFDM to its origin in the context of standard inflation, including the tensor modes and their associated stochastic gravitational-wave background (SGWB), and self-consistently account for the effect of the evolution of the background universe and the SGWB on each other.

Unlike standard CDM, which is always non-relativistic once it decouples from the thermal bath, SFDM has an evolving equation of state (EOS). As we had shown previously, there are four eras in the evolution of a homogeneous ΛSFDM universe: the familiar radiation-dominated, matter-dominated and Λ-dominated eras common to standard ΛCDM as well, but also an earlier era dominated by SFDM with a stiff equation of state. In this paper, we embedded this model self-consistently into the standard inflationary paradigm by postulating that inflation is followed by an extended epoch of reheating (with matter-like EOS), from which SFDM emerges, as well as the particles of the Standard Model. We assumed that most of the energy density of the inflaton field goes into the creation of the DM bosons, which quickly condense into their ground state, thereafter giving rise to SFDM in its stiff phase. The subdominant energy density of standard model particles constitutes the radiation component. We adopted an instant transition, where the end of reheating at $T = T_{\rm reheat}$ is followed by the stiff-SFDM-dominated era of ΛSFDM.

Standard inflation predicts a stochastic background of gravitational waves, mainly encoded in a finite value of the tensor-to-scalar ratio r, which is related to the energy scale of inflation. We have shown that this SGWB is amplified during the stiff-SFDM-dominated epoch compared with what it would be in a ΛCDM universe. SFDM in its relativistic phases (first stiff, then radiation-like EOS) and this amplified SGWB from inflation both add to the number of relativistic degrees of freedom, $N_{\rm eff}$, in the early universe before and around Big Bang nucleosynthesis (BBN), and possibly up to the time of matter-radiation equality at $z_{\rm eq}$. It is necessary to ensure that the stiff-SFDM-dominated era ends no later than when BBN begins. Moreover, since the combined energy density of SFDM plus the amplified SGWB must preserve $z_{\rm eq}$ from CMB measurements, SFDM should be nonrelativistic by the time of

$z_{\rm eq}$. The constraints derived in Paper I on the SFDM particle parameters, boson mass m and two-particle self-interaction $\lambda > 0$, required to make the SFDM compatible with these observables had to be modified here to account for the presence of the SGWB. Since many cosmological observables are dependent upon the ratio $\lambda/(mc^2)^2$, rather than λ, we express our results for the constraints on SFDM in terms of the parameter pair $(\lambda/(mc^2)^2,\ m)$.

We considered two values for r, $r = 0.01$ and $r = 0.1$, focusing on the former in particular, which is still seven times below current upper bounds from CMB measurements. We chose several values of the reheat temperatures, spanning a wide range from 1 to 10^9 GeV, to probe the range of impacts of SFDM on the inflationary SGWB. To this end, we solved the fully-coupled Klein-Gordon and Einstein field equations for the time-dependence of different ΛSFDM models, self-consistently accounting for their amplification of the SGWB from inflation. We studied the back-reaction of the energy density of the enhanced SGWB on the expansion history of the universe, which in turn affected the SGWB, requiring us to develop an elaborate numerical methodology. We incorporated important additional effects, like the effect of electron-positron annihilation on the thermal history, as well as the damping of tensor modes due to the free streaming of neutrinos.

The amplification of the SGWB from inflation in ΛSFDM makes possible the prospective detection of the latter, using current and upcoming gravitational wave observatories. In fact, we calculated the present-day gravitational wave energy spectra, $\Omega_{\rm GW}(f)$, and found that detection of the SGWB at high frequencies is within reach of the Advanced LIGO/Virgo experiment and possibly LISA in the future. We have shown that, for SFDM particle parameters that satisfy the above cosmological constraints, the amplified SGWB is currently detectable by aLIGO for a broad range of reheat temperatures, for values of the tensor-to-

scalar ratio currently allowed by CMB polarization measurements. Using the actual noise characteristics of the aLIGO O1 run (kindly provided us by the LIGO Scientific Collaboration), we determined the expected SNR for the inflationary SGWB in ΛSFDM for a range of model parameters. The null detection of the SGWB by the aLIGO O1 run, recently reported by [142], has already provided a new kind of cosmological constraint on SFDM as illustrated by the case in Fig. 2.10 and the middle panel of Fig. 2.12, with an excluded range of cases shown in Fig. 2.11. A wider range of SFDM parameters and reheat temperatures will be accessible to the aLIGO O5 run, potentially detecting this unique signature of the SFDM model.

• **Cosmological constraints on SFDM particle parameters**

In §2.4, we described in detail how observational constraints on $N_{\rm eff,BBN}$ and $z_{\rm eq}$ constrain the allowed range of SFDM particle parameters $(\lambda/(mc^2)^2,\ m)$ for given values of r and $T_{\rm reheat}$. Details aside, a rough summary of those results can be described as follows. For $\lambda/(mc^2)^2$, we found

$$10^{-18}\ {\rm eV}^{-1}\ {\rm cm}^3 \lesssim \frac{\lambda}{({\rm mc}^2)^2} \lesssim 4\times 10^{-17}\ {\rm eV}^{-1}\ {\rm cm}^3, \tag{2.92}$$

For m, we found

$$m \gtrsim 5\times 10^{-21}\times \frac{T_{\rm reheat}}{10^3\ {\rm GeV}}\sqrt{\frac{r}{0.01}}\ {\rm eV}/c^2, \tag{2.93}$$

for $r \gtrsim 0.01$ and $T_{\rm reheat} \gtrsim 10^3$ GeV, and $m \gtrsim 5\times 10^{-21}$ eV$/c^2$ for $r \gtrsim 0.01$ and $T_{\rm reheat} < 10^3$ GeV. As discussed in §2.6.1, if we relax the $N_{\rm eff,BBN}$ constraint, such that $\Delta N_{\rm eff,BBN} = 0$ is allowed, then the lower limit in Eq. (2.92) goes away, and even $\lambda \to 0$ is allowed.

• **Detectability of the SGWB from inflation in ΛSFDM**

As described in §2.5, the detectability of the SGWB $\Omega_{\rm GW}(f)$ amplified in ΛSFDM depends upon the SFDM particle parameters, $T_{\rm reheat}$, and r. For fixed r and $T_{\rm reheat}$, the maximum predicted signal corresponds to the pairs of $(\lambda/(mc^2)^2,\ m)$ which marginally satisfy the cosmological constraints and maximize the duration of the stiff era. For each of the allowed value of $\lambda/(mc^2)^2$, the minimum allowed value of m maximizes this duration. For LIGO, the overall maximum predicted signal (at fixed r) corresponds to this maximum when $T_{\rm reheat}$ is chosen so that $f_{\rm reheat}$ lies inside the LIGO sensitive frequency band. For $r = 0.01$, this corresponds to $T_{\rm reheat} \simeq 2 \times 10^4$ GeV, for which we predict an SNR ~ 10 for the recent aLIGO/Virgo O1 run. The null detection in the O1 data recently reported [142], therefore, excludes this particular maximally-detectable case.

In the future, we will be able to compare the ΛSFDM model predictions to this O1 data for the *full* range of model parameters allowed by the cosmological constraints described in §2.4 to determine what subset of these allowed parameters also satisfy this *new* cosmological constraint from direct measurement of the SGWB today. While that is beyond the scope of the present paper, we have, however, made such a determination for a representative family of marginally-allowed cases, for $r = 0.01$ and $\lambda/(mc^2)^2 = 10^{-18}$ eV^{-1} cm^3, as follows. Null detection by the O1 run now excludes at 95% confidence. the range $8.75 \times 10^3 \lesssim T_{\rm reheat}$ (GeV) $\lesssim 1.7 \times 10^5$, for which the corresponding masses are in the range $7 \times 10^{-20} \lesssim m$ (eV/c^2) $\lesssim 1.36 \times 10^{-18}$.

A wider range of ΛSFDM model parameters will be accessible to aLIGO/Virgo as time goes on. For $r = 0.01$ and $\lambda/(mc^2)^2 = 10^{-18}$ eV^{-1} cm^3, for example, a 3σ detection of the inflationary SGWB is predicted for the O5 run if $6 \times 10^2 \lesssim T_{\rm reheat}$ (GeV) $\lesssim 10^7$. For these $T_{\rm reheat}$ ranges, the ranges of particle masses in the marginally-allowed models correspond to

$5 \times 10^{-21} \lesssim m\ (\mathrm{eV/c^2}) \lesssim 8 \times 10^{-17}$ (O5).

For parameters in these ranges, our predicted SNR for aLIGO/Virgo for the SGWB from inflation in ΛSFDM can exceed current predictions of the background from unresolved binary black hole mergers in [142], as shown in Fig. 2.12. It will be important, therefore, to consider this inflationary SGWB in ΛSFDM in interpreting the current and future GW detection results.

We have also shown here that, for a range of values of T_{reheat} and allowed values of r, the inflationary SGWB in ΛSFDM may also be detectable by LISA. In that case, the difference in spectral shape between the primordial and black-hole merger GW backgrounds may allow them to be distinguished.

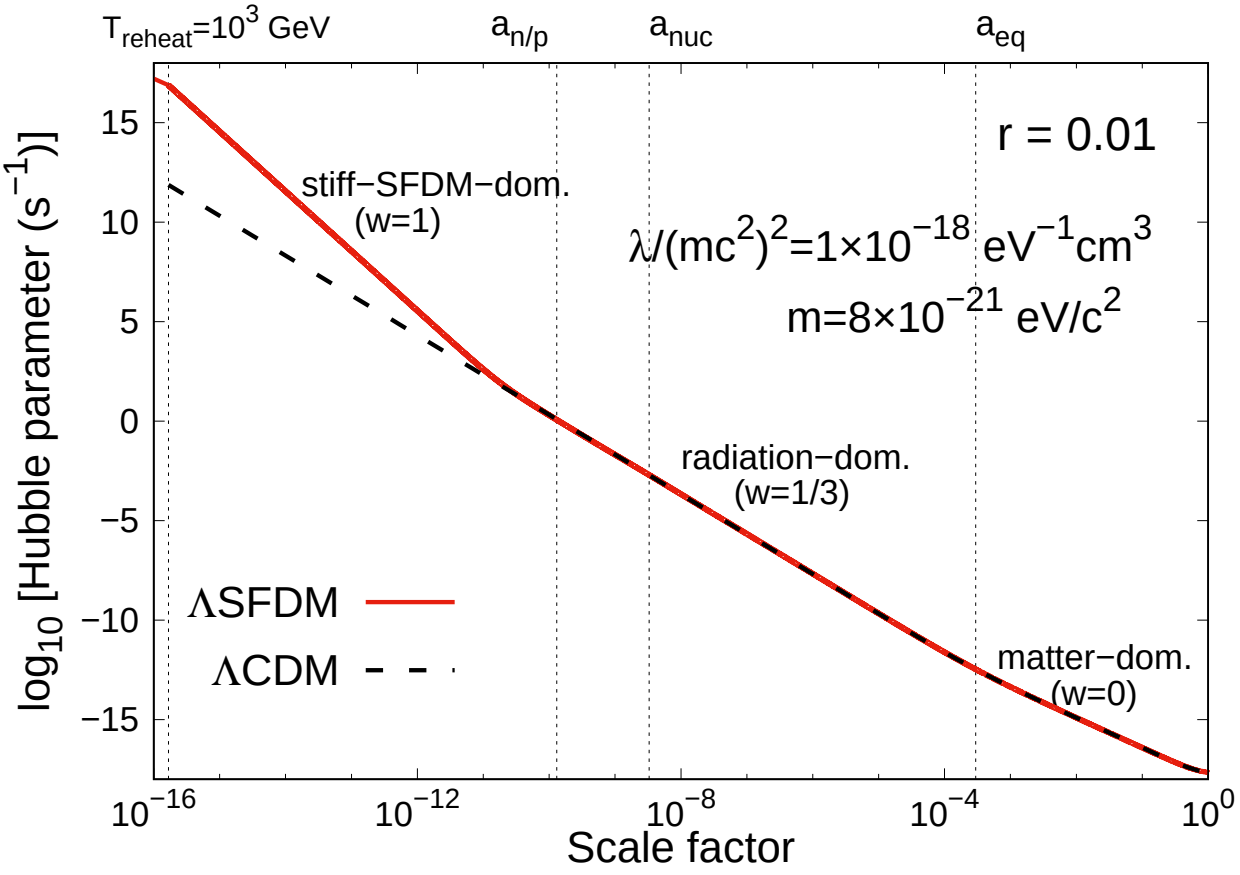

Figure 2.2: Expansion history of a ΛSFDM model, of which the particle parameters are $\lambda/(mc^2)^2 = 1 \times 10^{-18}$ eV^{-1} cm^3 and $m = 8 \times 10^{-21}$ eV/c^2. This is one of the example models in Fig. 2.1.

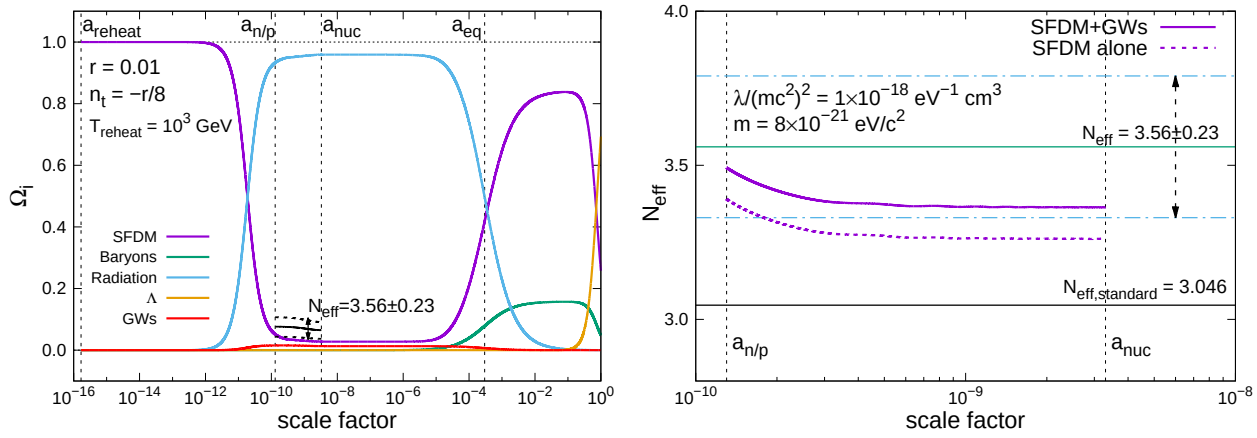

Figure 2.3: *left-hand plot:* Post-inflationary evolution of energy density fractions of all cosmic components, Ω_i *vs.* a, for an example ΛSFDM model. *right-hand plot:* Evolution of $N_{\rm eff,BBN}$ *vs.* a, for the same model during BBN. The solid purple curve accounts for all contributions to $N_{\rm eff,BBN}$, including SFDM and the SGWB from inflation.

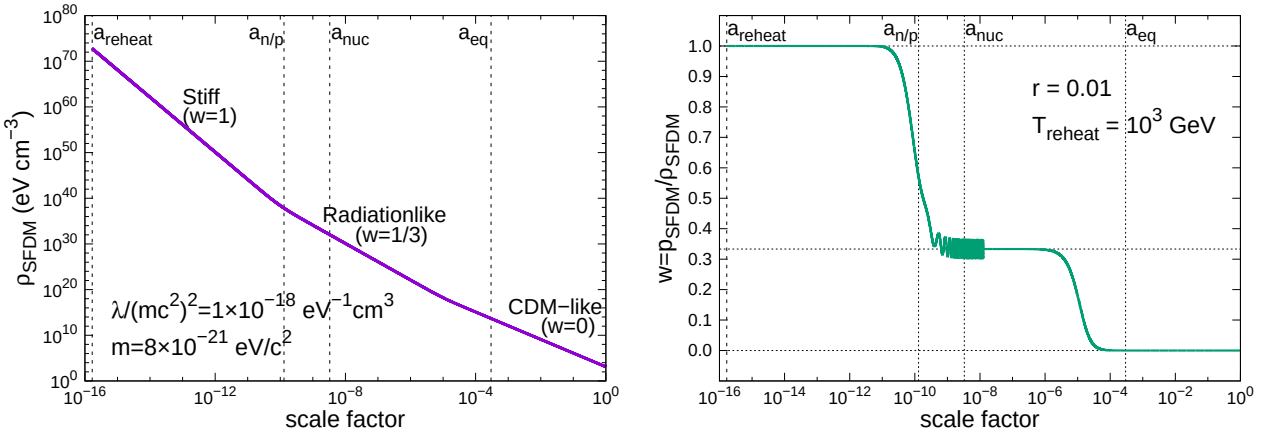

Figure 2.4: *left-hand plot:* Evolution of the energy density of SFDM. *right-hand plot:* Evolution of equation of state of SFDM. Oscillations are shown explicitly for $a < a_M$, which are manifest in the EOS plot, but only the smooth average is plotted for $a > a_M$.

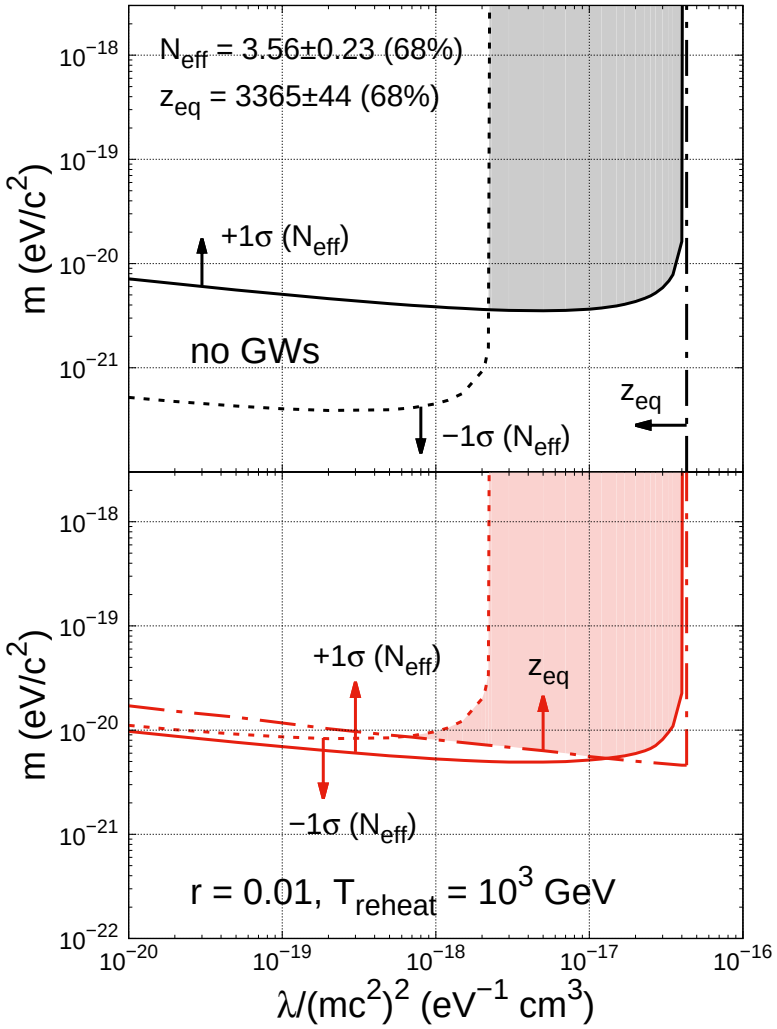

Figure 2.5: Cosmological constraints expressed in the SFDM parameter space for values $(\lambda/(mc^2)^2, m)$. *Upper plot:* for the case which does not include GWs, as in Paper I. *Lower plot:* for the case which self-consistently includes GWs, in which $r = 0.01$ and $T_{\rm reheat} = 10^3$ GeV. In both plots, the solid curve corresponds to the constraint from the $+1\sigma$ confidence limit of $N_{\rm eff,BBN}$ at $a_{\rm n/p}$, the dashed curve corresponds to the constraint from the -1σ confidence limit of $N_{\rm eff,BBN}$ at $a_{\rm nuc}$, and the dash-dotted curve indicates the constraint from $z_{\rm eq}$. The arrows indicate the directions in which the SFDM particle parameters satisfy the respective cosmological constraints. In each plot, the shaded region denotes the overall allowed range of the SFDM particle parameters, for the respective case.

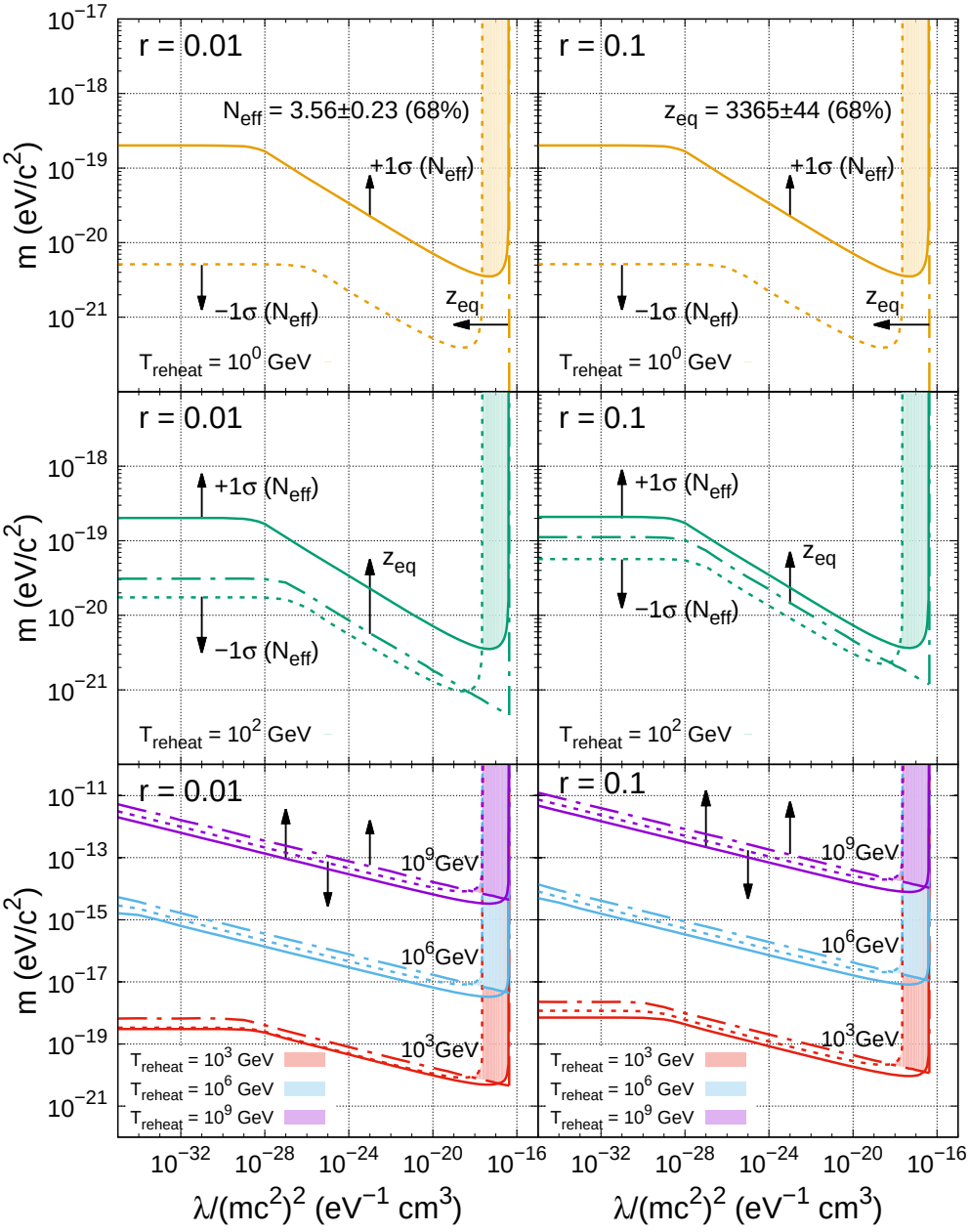

Figure 2.6: Cosmological constraints expressed in the SFDM parameter space for values $(\lambda/(mc^2)^2, m)$, for multiple choices of $T_{\rm reheat}$ and r. In each panel, the shaded region indicates the values of the SFDM particle parameters which are allowed by the cosmological constraints, and the arrows indicate the directions of these constraints, the same as in Fig. 2.5. In the bottom two panels, the allowed regions of the SFDM particle parameters, for multiple choices of $T_{\rm reheat}$, are plotted together; all of them actually extend and overlap in the direction of larger-mass, exceeding the plot range, same as in the upper and middle panels.

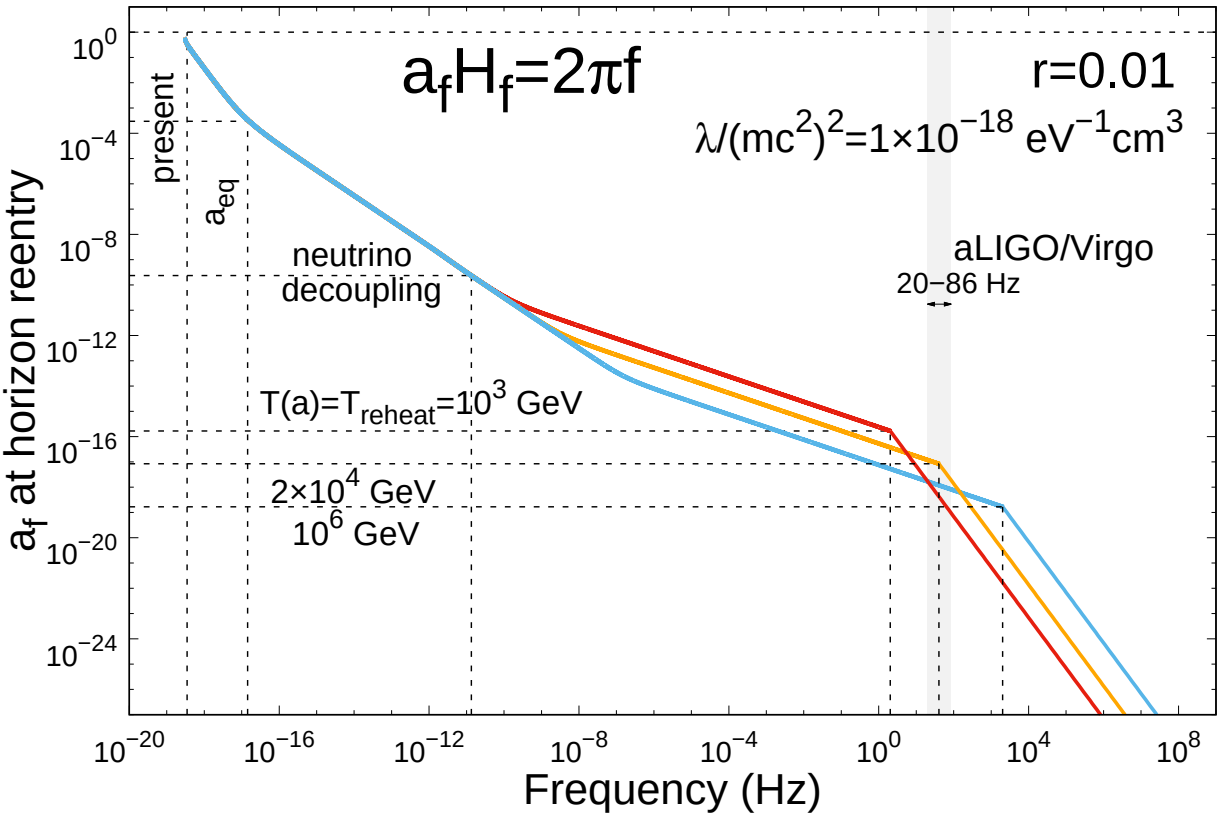

Figure 2.7: Scale factor a_f at horizon reentry ($a_f H_f = 2\pi f$) vs. the comoving frequency f for each mode, plotted for three example ΛSFDM models with different $T_{\rm reheat}$. $T(a)$ refers to the photon temperature at this scale factor.

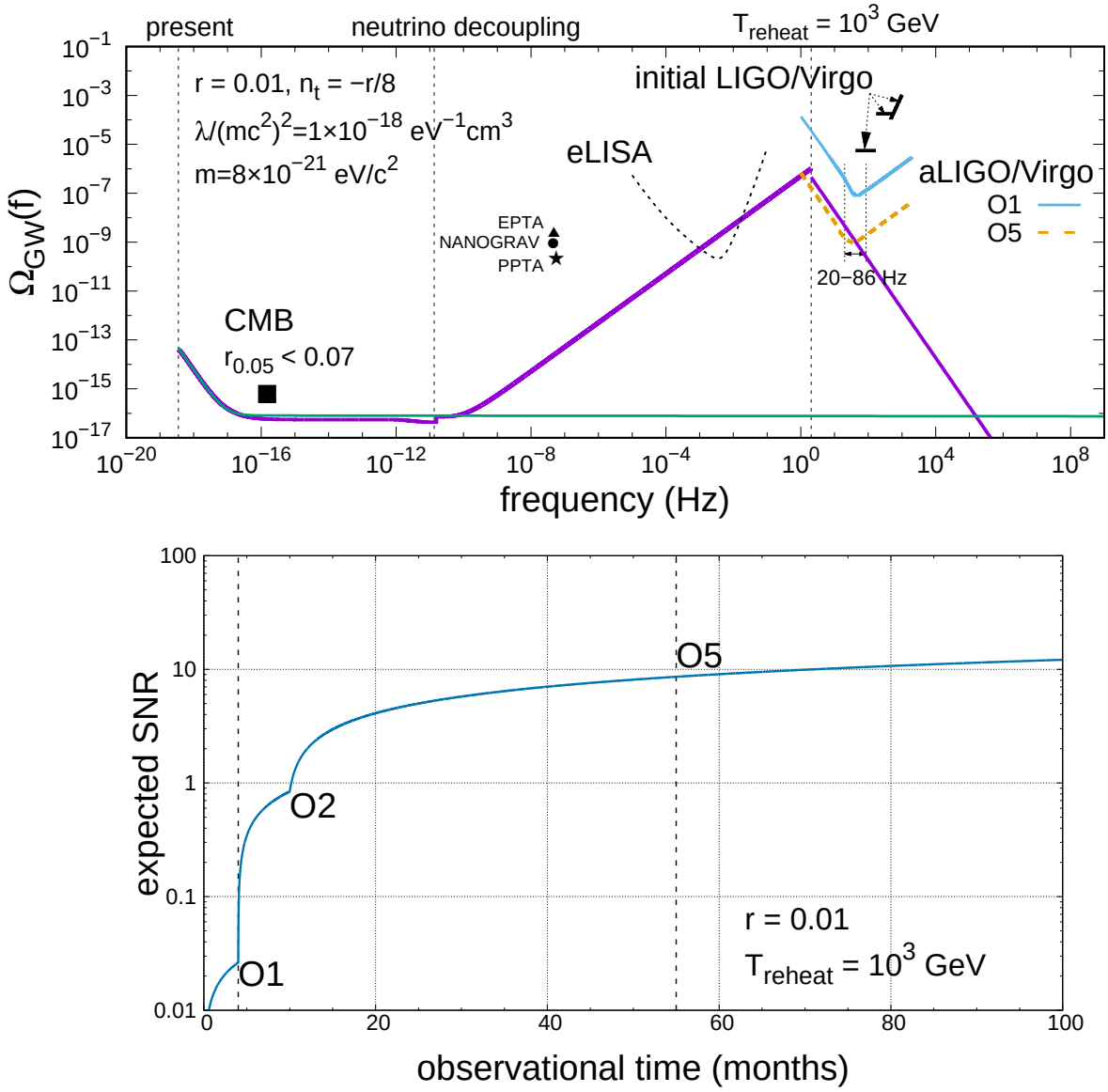

Figure 2.8: *Upper plot:* Present-day energy density spectrum of the SGWB from inflation. The purple curve shows the prediction from one example ΛSFDM model in which reheating ends at $T_{\rm reheat} = 10^3$ GeV. The green curve shows the prediction of the standard ΛCDM model. $r = 0.01$ for both cases. [Note: the $e^- e^+$ annihilation results in the little kink of the purple curve right before neutrino decoupling. This effect had not been taken into account in the green ΛCDM curve.] The blue solid curve and the yellow dashed curve indicate the 1σ-sensitivity curves of aLIGO/Virgo for the two observing runs O1 (with data now analyzed) and O5 (theoretical forecast for 2-year run), respectively, integrated over frequency for the inflationary SGWB energy density spectra in ΛSFDM. Upper limits from various experiments are shown, including the joint CMB analysis, PTA experiments and the (initial) LIGO/Virgo, all at 95% confidence. (The current upper limit from the aLIGO O1 run is shown in Fig. 2.12.) The LISA sensitivity curve is the predicted strain noise function of eLISA in [146] and may be revised in the final design of the upcoming LISA mission. *Lower plot:* The expected SNR of the inflationary SGWB predicted by the same ΛSFDM model *vs.* the cumulative observation time of aLIGO/Virgo. The dashed vertical lines indicate the observation time by the end of O1 and O5 runs, respectively.

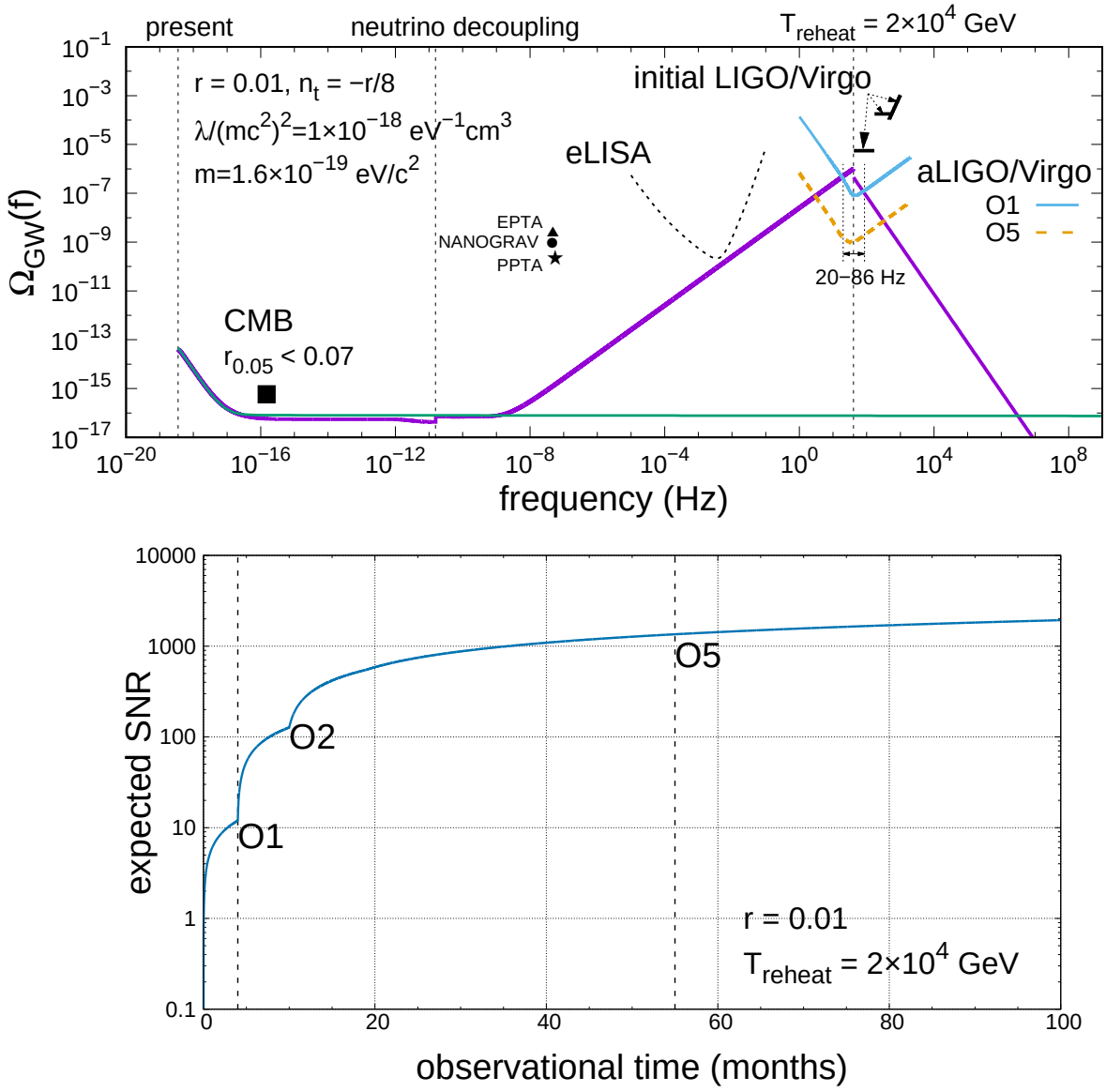

Figure 2.9: Caption same as in Fig. 2.8, except for a ΛSFDM model with $T_{\rm reheat} = 2 \times 10^4$ GeV.

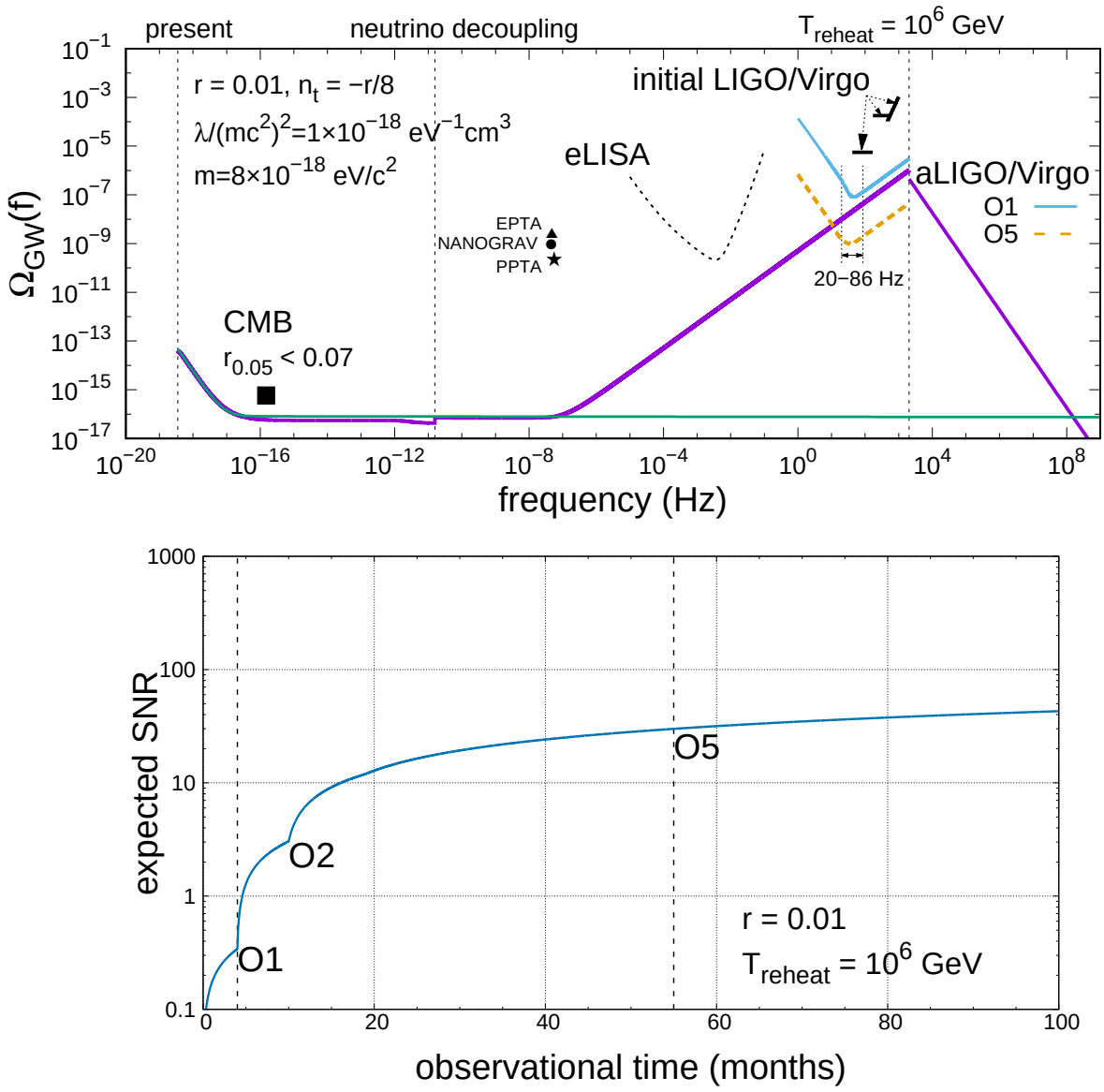

Figure 2.10: Caption same as in Fig. 2.8, except for a ΛSFDM model with $T_{\rm reheat} = 10^6$ GeV.

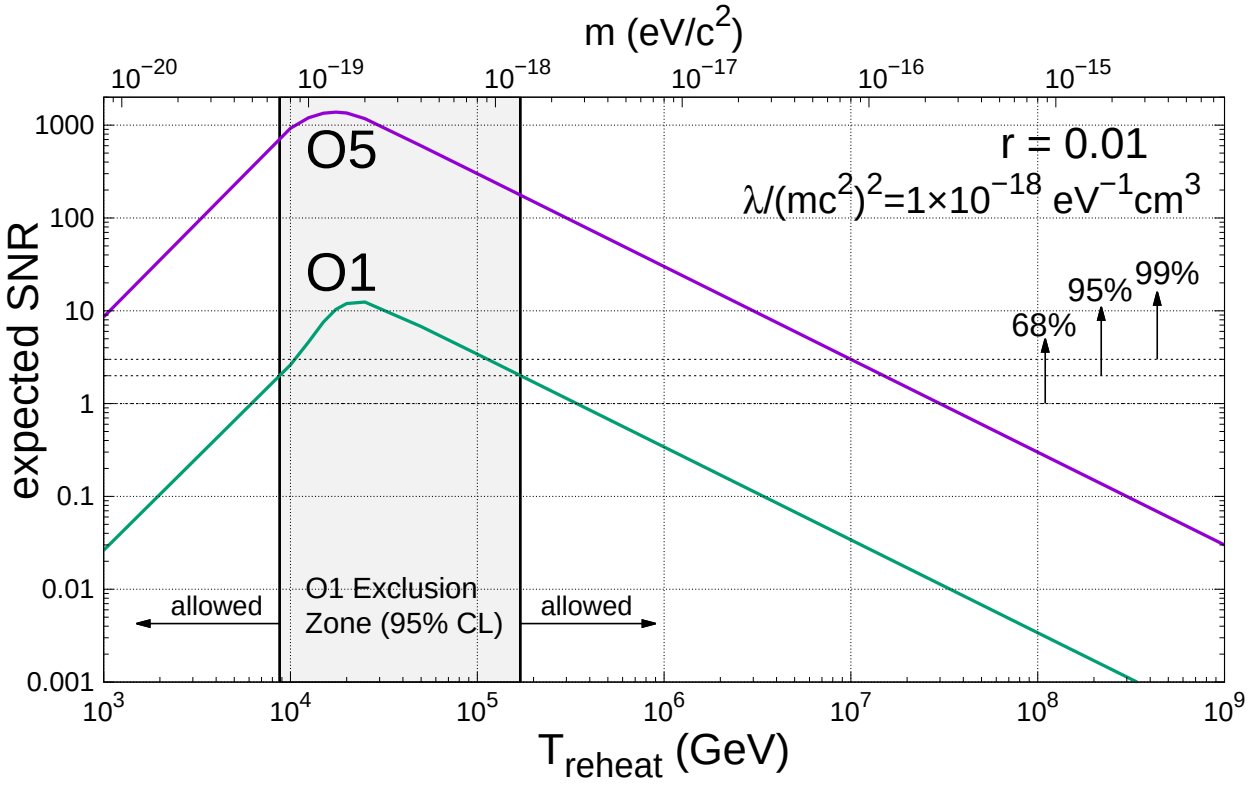

Figure 2.11: Dependence of the expected SNR on $T_{\rm reheat}$, for the inflationary SGWB measured by aLIGO/Virgo by the end of the O1 and O5 runs, respectively. Both curves are predictions of ΛSFDM models which assume $r = 0.01$ and $\lambda/(mc^2)^2 = 1 \times 10^{-18}$ eV^{-1}cm^3, and, for each value of $T_{\rm reheat}$, the particle mass m has the value which marginally satisfies current cosmological constraints for that case. The maximally detectable model corresponds to a value of $T_{\rm reheat}$ between 10^4 and 10^5 GeV.

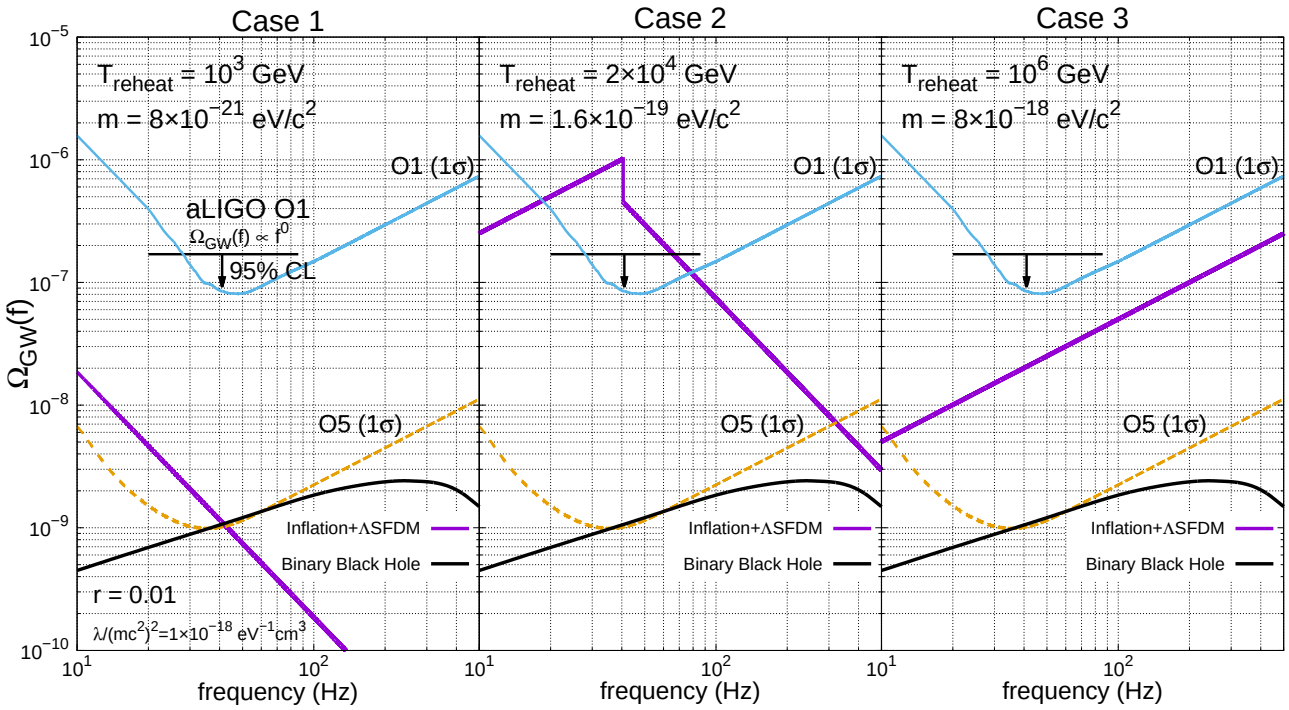

Figure 2.12: Present-day energy density spectra of the SGWB from inflation (purple curves) for the same illustrative ΛSFDM models as in Figs. 2.8 – 2.10 but zoomed in around the LIGO sensitive frequency band ($20 - 86$ Hz), compared with the predicted energy spectrum of the SGWB from unresolved binary black hole merger events (black curves), for which the merger rate is constrained by data from the completed aLIGO O1 run [142]. All the three ΛSFDM cases marginally satisfy the cosmological constraints described in §2.4, for which $r = 0.01$ and $\lambda/(mc^2)^2 = 1 \times 10^{-18}$ eV^{-1}cm^3, but the values of $T_{\rm reheat}$ and m vary. The new 95% C.L. upper limit for an SGWB with a flat power spectrum, from the recent O1 run data [142], is also shown here.

Appendices

Appendix A

SFDM Cosmology Appendix

A.1 Basic equations in a perturbed Friedmann-Robertson-Walker metric

The general perturbed Friedmann-Robertson-Walker (FRW) metric in the comoving frame has the form

$$\mathrm{d}s^2 = (1+2\Psi/c^2)c^2\mathrm{d}t^2 - 2a(t)w_i c\mathrm{d}t\mathrm{d}x^i - \\ -a^2(t)[(1-2\Phi/c^2)\delta_{ij} + H_{ij}]\mathrm{d}x^i\mathrm{d}x^j, \tag{A.1}$$

where the perturbed quantities $|\Psi|/c^2, |\Phi|/c^2, |w_i|$, and $|H_{ij}|$ are all $\ll 1$.

A.1.1 Conformal Newtonian gauge

We can apply the conformal Newtonian Gauge if only scalar perturbations are permitted, where the metric reduces to [149]

$$\mathrm{d}s^2 = (1+2\Psi/c^2)c^2\mathrm{d}t^2 - a^2(t)(1-2\Phi/c^2)\delta_{ij}\mathrm{d}x^i\mathrm{d}x^j, \tag{A.2}$$

or

$$g_{00} = 1 + 2\frac{\Psi}{c^2},\ g_{ij} = -a^2(t)\left(1 - 2\frac{\Phi}{c^2}\right)\delta_{ij},$$
$$g^{00} = 1 - 2\frac{\Psi}{c^2},\ g^{ij} = -\frac{1}{a^2(t)}\left(1 + 2\frac{\Phi}{c^2}\right)\delta_{ij}$$

The corresponding Christoffel symbols are [141]

$$\Gamma^0{}_{00} = \frac{1}{c^3}\partial_t\Psi,\ \Gamma^0{}_{i0} = \frac{1}{c^2}\partial_i\Psi,\ \Gamma^i{}_{00} = \frac{1}{c^2a^2}\partial_i\Psi,$$

$$\Gamma^i{}_{j0} = \left(-\frac{1}{c^3}\partial_t\Phi + \frac{\mathrm{d}a/\mathrm{d}t}{ca}\right)\delta_{ij},$$

$$\Gamma^0{}_{jk} = \left(-\frac{a^2}{c^3}\partial_t\Phi + \frac{a\mathrm{d}a/\mathrm{d}t}{c}(1 - 2\frac{\Psi}{c^2} - 2\frac{\Phi}{c^2})\right)\delta_{jk},$$

$$\Gamma^i{}_{jk} = -\frac{1}{c^2}\left(\partial_k\Phi\delta_{ij} + \partial_j\Phi\delta_{ik} - \partial_i\Phi\delta_{jk}\right). \tag{A.3}$$

A.1.2 Klein-Gordon equation

The variation of the action

$$\mathscr{S} = \int \mathrm{d}^4x\sqrt{-g}\mathscr{L}(\psi, \psi^*, \partial_\mu\psi, \partial_\mu\psi^*), \tag{A.4}$$

with $g = \det(g_{\mu\nu})$, yields

$$\begin{aligned}\delta\mathscr{S} &= \int \mathrm{d}^4x\sqrt{-g}\ \times \\ &\times\left(\frac{\partial\mathscr{L}}{\partial(\partial_\mu\psi)}\partial_\mu\delta\psi + \frac{\partial\mathscr{L}}{\partial\psi}\delta\psi + \frac{\partial\mathscr{L}}{\partial(\partial_\mu\psi^*)}\partial_\mu\delta\psi^* + \frac{\partial\mathscr{L}}{\partial\psi^*}\delta\psi^*\right) \\ &= \int \mathrm{d}^4x\Bigg[\left(-\partial_\mu\left(\sqrt{-g}\frac{\partial\mathscr{L}}{\partial(\partial_\mu\psi)}\right) + \sqrt{-g}\frac{\partial\mathscr{L}}{\partial\psi}\right)\delta\psi + \\ &\quad + \left(-\partial_\mu\left(\sqrt{-g}\frac{\partial\mathscr{L}}{\partial(\partial_\mu\psi^*)}\right) + \sqrt{-g}\frac{\partial\mathscr{L}}{\partial\psi^*}\right)\delta\psi^*\Bigg].\end{aligned} \tag{A.5}$$

For arbitrary $\delta\psi$ and $\delta\psi^*$, $\delta\mathscr{S} = 0$ only when both integrands in the expression above are constantly zero, which yields the Euler-Lagrangian equation

$$\frac{1}{\sqrt{-g}}\partial_\mu\left(\sqrt{-g}\frac{\partial\mathscr{L}}{\partial(\partial_\mu\psi)}\right) - \frac{\partial\mathscr{L}}{\partial\psi} = 0. \tag{A.6}$$

Upon inserting the Lagrangian (1.4), one recovers (1.7).

A.1.3 Einstein field equations and curvature tensor

The Einstein-Hilbert action is defined as

$$\mathscr{S}_H = \int \mathrm{d}^4x\sqrt{-g}\left(\frac{R}{16\pi G c^{-4}} + \mathscr{L}\right). \tag{A.7}$$

The Einstein field equations can be derived from the principle of least action with variation in $g^{\mu\nu}$:

$$\begin{aligned} 0 &= \delta\mathscr{S}_H \\ &= \int d^4x\left(\frac{\delta(\sqrt{-g}R)}{16\pi G c^{-4}} + \delta(\sqrt{-g}\mathscr{L})\right) \\ &= \int d^4x\bigg(-\frac{\sqrt{-g}}{16\pi G c^{-4}}(R_{\mu\nu} - \frac{1}{2}g_{\mu\nu}R) + \frac{\delta(\sqrt{-g}\mathscr{L})}{\delta g^{\mu\nu}}\bigg)\delta g^{\mu\nu}. \end{aligned} \tag{A.8}$$

Defining the energy-momentum tensor as

$$T_{\mu\nu} \equiv \frac{2}{\sqrt{-g}}\frac{\delta\left(\sqrt{-g}\mathscr{L}(g^{\mu\nu}, \partial^\rho g^{\mu\nu})\right)}{\delta g^{\mu\nu}} = 2\frac{\delta\mathscr{L}}{\delta g^{\mu\nu}} - g_{\mu\nu}\mathscr{L}, \tag{A.9}$$

the field equations are thus

$$R_{\mu\nu} - \frac{1}{2}g_{\mu\nu}R = \frac{8\pi G}{c^4}T_{\mu\nu}. \tag{A.10}$$

The Riemann curvature tensor is defined as

$$R^\rho{}_{\sigma\mu\nu} = \partial_\mu\Gamma^\rho{}_{\sigma\nu} - \partial_\nu\Gamma^\rho{}_{\sigma\mu} + \Gamma^\rho{}_{\mu\alpha}\Gamma^\alpha{}_{\sigma\nu} - \Gamma^\rho{}_{\nu\alpha}\Gamma^\alpha{}_{\sigma\mu}. \tag{A.11}$$

With the Christoffel symbols (A.3) we can calculate the diagonal Ricci tensors to first order in $|\Psi|/c^2,\ |\Phi|/c^2$,

$$\begin{aligned} R_{\mu\nu} &\equiv R^\rho{}_{\mu\rho\nu}, \\ R_{00} &= -\frac{3}{c^2}\frac{\mathrm{d}^2a/\mathrm{d}t^2}{a} + \frac{1}{c^2a^2}\nabla^2\Psi + \frac{3}{c^4}\partial_t^2\Phi + \\ &\quad + \frac{3\mathrm{d}a/\mathrm{d}t}{c^4a}(\partial_t\Psi + 2\partial_t\Phi), \end{aligned}$$

$$R_{ii} = \frac{a\mathrm{d}^2a/\mathrm{d}t^2 + 2(\mathrm{d}a/\mathrm{d}t)^2}{c^2}\left(1 - 2\frac{\Psi}{c^2} - 2\frac{\Phi}{c^2}\right) -$$
$$-\frac{a\mathrm{d}a/\mathrm{d}t}{c^4}(6\partial_t\Phi + \partial_t\Psi) - \frac{a^2}{c^4}\partial_t^2\Phi + \frac{1}{c^2}\nabla^2\Phi - \frac{1}{c^2}\partial_i^2(\Psi - \Phi).$$

Consequently the Ricci scalar is

$$\begin{aligned} R \equiv g^{\mu\nu}R_{\mu\nu} = &-\frac{6}{c^2}\left(\frac{\mathrm{d}^2a/\mathrm{d}t^2}{a} + \frac{(\mathrm{d}a/\mathrm{d}t)^2}{a^2}\right) + \\ &+\frac{2}{c^2a^2}\nabla^2(\Psi - \Phi) - \frac{2}{c^2a^2}\nabla^2\Phi + \frac{6\partial_t^2\Phi}{c^4} + \\ &+\frac{6\mathrm{d}a/\mathrm{d}t}{c^4a}(\partial_t\Psi + 4\partial_t\Phi) + \frac{12}{c^4}\left(\frac{\mathrm{d}^2a/\mathrm{d}t^2}{a} + \frac{(\mathrm{d}a/\mathrm{d}t)^2}{a^2}\right)\Psi. \end{aligned} \tag{A.12}$$

A.2 Oscillation and charge of the complex scalar field in an homogeneous Friedmann-Robertson-Walker metric

Let us write the equation of motion with homogeneous FRW metric (1.19), again,

$$\frac{\hbar^2}{2mc^2}\partial_t^2\psi + \frac{\hbar^2}{2mc^2}\frac{3\mathrm{d}a/\mathrm{d}t}{a}\partial_t\psi + \frac{1}{2}mc^2\psi + \lambda|\psi|^2\psi = 0. \tag{A.13}$$

Now, we will decompose the complex scalar field as

$$\psi = |\psi|e^{i\theta}, \tag{A.14}$$

where $|\psi|$ is the amplitude of the scalar field and θ is its phase. They are both real functions. Inserting this decomposition into the equation of motion above yields

$$\frac{\hbar^2}{2mc^2}\left(\partial_t^2|\psi| - |\psi|(\partial_t\theta)^2\right) + \frac{\hbar^2}{2mc^2}\frac{3\mathrm{d}a/\mathrm{d}t}{a}\partial_t|\psi| + \frac{1}{2}mc^2|\psi| + \lambda|\psi|^3 = 0, \tag{A.15}$$

$$\frac{\hbar^2}{2mc^2}\left(2\partial_t|\psi|\partial_t\theta + |\psi|\partial_t^2\theta\right) + \frac{\hbar^2}{2mc^2}\frac{3\mathrm{d}a/\mathrm{d}t}{a}|\psi|\partial_t\theta = 0. \tag{A.16}$$

We first look at equation (A.15). It is the phase that carries the major oscillation behavior for a complex scalar field, while the time dependence of the amplitude is smooth. In

the fast oscillation regime, in which the Hubble expansion rate $H = \frac{\mathrm{d}a/\mathrm{d}t}{a}$ is minute compared with $\partial_t\theta$, we also assume that $\partial_t|\psi|/|\psi| \ll \partial_t\theta$ (which is not always the case). We can then neglect the terms involving $\partial_t|\psi|$ and H in equation (A.15) and obtain

$$-\frac{\hbar^2}{2mc^2}|\psi|(\partial_t\theta)^2 + \frac{1}{2}mc^2|\psi| + \lambda|\psi|^3 = 0. \tag{A.17}$$

We define the angular oscillation frequency as $\omega \equiv \partial_t\theta$. Rearranging the equation above yields

$$\omega = \frac{mc^2}{\hbar}\sqrt{1 + \frac{2\lambda}{mc^2}|\psi|^2}, \tag{A.18}$$

which can be also viewed as the dispersion relation in the zero-momentum case of our complex scalar field. We should bear in mind that the relation (A.18) is only valid when $\omega \gg H$. In the case of a free field ($\lambda = 0$), the frequency reduces to the particle mass, $\omega = mc^2/\hbar$, as one may expect.

Let us turn to equation (A.16). It can be exactly integrated once [150], giving

$$\partial_t(a^3|\psi|^2\partial_t\theta) = 0.$$

Therefore, we can see that $a^3|\psi|^2\partial_t\theta$ is conserved over cosmic time. In fact, it is proportional to the conserved charge density Q, defined in Section 1.1.2,

$$a^3|\psi|^2\partial_t\theta = Q\frac{mc^2}{\hbar}. \tag{A.19}$$

In the case of a complete BEC, anti-bosons are nearly annihilated away so that the charge basically equals the total number of condensed bosons (see Refs. [35, 108, 109]). The conservation of the charge, or equivalently, the conservation of the charge density Q results from the global U(1) symmetry of the Lagrangian density (1.4). This is a distinct feature in contrast to a real scalar field. Since a real field does not possess phase information θ, there is

no global U(1) symmetry and no non-trivial charge. In fact, the boson is its own anti-boson for a real scalar field.

A.3 Matching conditions of the early-time and late-time solution

The integration of the equations for the early-time solution is performed backwards in time from the matching point with the late-time solution, at $\omega/H = 200$. This matching condition requires that the starting values of $\bar{p}$, $\bar{\rho}$ and the scale factor a for the early-time solution are given by $\langle\bar{p}\rangle$, $\langle\bar{\rho}\rangle$ and a at the matching point in the late-time solution, with the value of B there set as follows (we omit the subscript SFDM in this appendix). The starting value of B should be determined, in principle, by the following equation. Summing equations (1.17) and (1.18) yields

$$\begin{aligned}
\bar{\rho}+\bar{p} &= \frac{\hbar^2}{mc^2}|\partial_t\psi|^2 \\
&= \frac{\hbar^2}{mc^2}\left((\partial_t|\psi|)^2+|\psi|^2(\partial_t\theta)^2\right) \\
&= \frac{\hbar^2}{mc^2}\left(\frac{(\partial_t|\psi|^2)^2}{4|\psi|^2}+\frac{(|\psi|^2\partial_t\theta)^2}{|\psi|^2}\right) \\
&= \frac{\hbar^2}{mc^2|\psi|^2}\left(\frac{1}{4}\left(\frac{B}{mc^2}\right)^2+\frac{(Qmc^2/\hbar)^2}{a^6}\right) \\
&= \frac{\hbar^2}{2(\bar{\rho}-\bar{p})}\left(\sqrt{1+\frac{4\lambda(\bar{\rho}-\bar{p})}{(mc^2)^2}}+1\right)\times\left(\frac{1}{4}\left(\frac{B}{mc^2}\right)^2+\frac{(Qmc^2/\hbar)^2}{a^6}\right). \qquad \text{(A.20)}
\end{aligned}$$

Therefore, if we know the conserved charge density Q precisely, we should be able to calculate the exact value of B. Unfortunately, this is not practical, for Q is so huge (for a BEC) that the last term on the right-hand side of equation (A.20) is greater than the term involving B by many orders of magnitude. As a matter of fact, in the fast oscillation regime, the term involving B is always subdominant to the term involving Q for a BEC, justifying our assumption that $\partial_t|\psi|/|\psi| \ll \partial_t\theta$ (in the slow oscillation regime it is the converse). Thus, though we know that $Q \approx \bar{\rho}_{\rm dm}(t_0)/(mc^2)$, even a tiny error in Q will lead to a big variation in the value of B, making it impossible to use equation (A.20) to determine B.

Nevertheless, we have confirmed by testing different starting values of B that, changing B does not affect the time-average values of the SFDM energy density $\bar{\rho}$ and pressure $\bar{p}$, only causing different oscillation amplitudes of $\bar{p}$. Recall that the evolution of $\bar{\rho}$ is always smooth (see Section 1.3.3.1). The expansion history of the homogeneous background universe is thus unaffected despite the uncertainty in B, since the Friedmann equation (1.14) only concerns $\bar{\rho}$, and hence we are free to choose the starting value of B, within the range derived from equation (A.20), which corresponds to the range of uncertainty in the exact value of Q. Here is another remarkable feature of the complex scalar field: although the SFDM pressure shows oscillation generically, the amplitude of this oscillation is always a small fraction of the mean value for subdominant B values, as oscillations mainly manifest in the phase. This is distinct from the real field case again, as for a real scalar field, $\bar{w} = \bar{p}/\bar{\rho}$ oscillates between -1 and 1 (see Ref. [44]).

In this work, we choose the starting value of B for the early-time solution in a way that makes the early-time solution smoothly match onto the late-time solution, particularly in $\bar{p}$, with zero oscillation amplitude. To see that, subtracting equation (1.18) from equation (1.17) yields

$$B = mc^2\partial_t|\psi|^2 = \frac{mc^2\partial_t(\bar{\rho}-\bar{p})}{mc^2+2\lambda|\psi|^2} = \frac{\partial_t(\bar{\rho}-\bar{p})}{\sqrt{1+4\lambda(\bar{\rho}-\bar{p})/(mc^2)^2}}. \tag{A.21}$$

The starting value of B is then taken as

$$\begin{aligned} B_{\rm match} &= \frac{\partial_t(\langle\bar{\rho}\rangle - \langle\bar{p}\rangle)}{\sqrt{1+4\lambda(\langle\bar{\rho}\rangle - \langle\bar{p}\rangle)/(mc^2)^2}} \\ &= \frac{\partial_t\langle\bar{\rho}\rangle(1-\partial\langle\bar{p}\rangle/\partial\langle\bar{\rho}\rangle)}{\sqrt{1+4\lambda(\langle\bar{\rho}\rangle - \langle\bar{p}\rangle)/(mc^2)^2}} \\ &= -\frac{{\rm d}a/{\rm d}t}{a}\frac{(\langle\bar{\rho}\rangle + \langle\bar{p}\rangle)}{\sqrt{1+4\lambda(\langle\bar{\rho}\rangle - \langle\bar{p}\rangle)/(mc^2)^2}} \times \left(2+\frac{1}{\sqrt{1+6\lambda\langle\bar{\rho}\rangle/(mc^2)^2}}\right) \end{aligned} \tag{A.22}$$

where we assume that the matching point lies within the radiationlike phase of SFDM. With such starting value of B, the derived evolution of $\bar{w} = \bar{p}/\bar{\rho}$ from the integration of the exact

equations connects smoothly to that of the late-time solution for $\langle\bar{p}\rangle/\langle\bar{\rho}\rangle$, with no oscillation, as shown in the right-hand plot of Figure 1.1.

Appendix B

Inflationary SGWB in ΛSFDM Appendix

B.1 Gravitational Waves in a FLRW universe

B.1.1 Effective stress-energy tensor of gravitational waves

It is instructive to show how it is that tensor perturbations associated with gravitational waves also contribute an effective mean stress-energy to the background curvature of the universe, which is spatially homogeneous on large scales.

For a FLRW universe of which the metric is defined in Eq. (2.2), only allowing tensor perturbations, let us evaluate the left-hand side of the Einstein field equations (2.4),

$$R^{\mu}_{\ \nu} - \frac{1}{2}R = \left(R^{\mu}_{\ \nu}{}^{(0)} - \frac{1}{2}R^{(0)}\right) + \left(R^{\mu}_{\ \nu}{}^{(2)} - \frac{1}{2}R^{(2)}\right), \tag{B.1}$$

where we have expanded the left-hand side in perturbations h_{ij}, up to the second order. On the right-hand side of the expansion above, the zeroth-order term contributed by the unperturbed FLRW metric $\bar{g}_{\mu\nu}$ is familiar, of which the nonzero components are

$$R^{0}_{\ 0}{}^{(0)} - \frac{1}{2}R^{(0)} = \frac{3\dot{a}^2}{c^2a^2}, \tag{B.2}$$

$$R^{i}_{\ i}{}^{(0)} - \frac{1}{2}R^{(0)} = \frac{-a\ddot{a} + \dot{a}^2}{c^2a^2}. \tag{B.3}$$

The first-order term in the expansion vanishes. The second-order term (of the order $O(h^2)$) due to tensor perturbations, can be moved to the right-hand side of the Einstein field equations (2.4), and hence viewed as an effective contribution to the total stress-energy tensor

$T^{\mu}_{\ \nu}$. That is to say, $T_{\mu\nu,\ \mathrm{GW}}$ purely results from the spatial metric perturbations, rather than the stress-energy tensor of an intrinsic cosmic component.

The stress-energy carried by GWs can not be localized within a wavelength [131]. Instead, it is only meaningful to interpret the effective $T_{\mu\nu,\ \mathrm{GW}}$ as a macroscopic average over several wavelengths. With this understanding, we see that the stress-energy of GWs indeed contributes to the curvature of the homogeneous background universe. In other words, it back-reacts to the zeroth-order term in Eq. (B.1) once moved to the right-hand side. Let us, for simplicity, focus on subhorizon modes. We can then explicitly write down the stress-energy tensor of GWs,

$$\begin{aligned} T_{\mu\nu,\ \mathrm{GW}} &\equiv -\frac{c^4}{8\pi G}\left(\langle R^{(2)}_{\mu\nu}\rangle - \frac{1}{2}\bar{g}_{\mu\nu}\langle R^{(2)}\rangle\right) \\ &= \frac{c^4}{32\pi G}\langle (a^2 h_{ij})_{;\mu}(\frac{1}{a^2}h^{ij})_{;\nu}\rangle, \end{aligned} \tag{B.4}$$

where the brackets $\langle\cdot\rangle$ denote the spatial average over several wavelengths, and the semicolon denotes the covariant derivative with respect to the background metric $\bar{g}_{\mu\nu}$. This was first derived by Isaacson in [151, 152]. Therefore, $T_{\mu\nu,\ \mathrm{GW}}$ is also known as the Isaacson tensor.

Particularly, the time-time component of $T_{\mu\nu,\ \mathrm{GW}}$ defines the energy density of GWs,

$$\begin{aligned} \rho_{\mathrm{GW}} \equiv T^0_{\ 0,\ \mathrm{GW}} &= \frac{c^4}{32\pi G}\langle (a^2 h_{ij})_{;0}(\frac{1}{a^2}h^{ij})^{;0}\rangle \\ &= \frac{c^2}{32\pi G}\langle \partial_t h_{ij}\partial_t h^{ij}\rangle. \end{aligned} \tag{B.5}$$

Remember that $h^{ij} = h_{ij}$ (see also [147, 153, 120]).

B.1.2 Fourier decomposition of h_{ij}

It is customary to move into $\mathbf{k}$-space by Fourier transforming the tensor perturbations,

$$h_{ij}(\mathbf{x}, t) = \sum_P \int \frac{\mathrm{d}^3\mathbf{k}}{(2\pi)^3} h^P_{\mathbf{k}}(t)\mathrm{e}^{i\mathbf{k}\cdot\mathbf{x}}\epsilon^P_{ij}(\mathbf{k}), \tag{B.6}$$

where $\mathbf{k}$ is the comoving wave vector, and $\epsilon^P_{ij}(\mathbf{k})$ are the spin-2 polarization tensors for the "plus" and "cross" polarization states, $P = +$ or $\times$, with respect to the wave vector $\mathbf{k}$. Both

$\epsilon^{+}_{ij}(\mathbf{k})$ and $\epsilon^{\times}_{ij}(\mathbf{k})$ are symmetric, traceless ($\sum_i \epsilon^{P}_{ii}(\mathbf{k}) = 0$), and perpendicular to the direction in which the plane wave propagates (transverse), $\epsilon^{P}_{ij}(\mathbf{k}) \cdot \mathbf{k} = 0$. Also, $\epsilon^{P}_{ij}(-\mathbf{k}) = \epsilon^{P}_{ij}(\mathbf{k})$. They follow such normalization convention,

$$\sum_{i,j} \epsilon^{P}_{ij}(\mathbf{k}) \epsilon^{P'}_{ij}(\mathbf{k}) = 2\delta_{PP'}, \tag{B.7}$$

where $\delta_{PP'}$ is the Kronecker delta. In three-dimensional space with Cartesian coordinates, if $\mathbf{k}$ goes along the z-direction, the explicit form of ϵ^{P}_{ij} can be written as

$$\begin{aligned} \epsilon^{+}_{ij} &= \mathbf{e}_x \otimes \mathbf{e}_x - \mathbf{e}_y \otimes \mathbf{e}_y = \begin{pmatrix} 1 & 0 & 0 \\ 0 & -1 & 0 \\ 0 & 0 & 0 \end{pmatrix}, \\ \epsilon^{\times}_{ij} &= \mathbf{e}_x \otimes \mathbf{e}_y + \mathbf{e}_y \otimes \mathbf{e}_x = \begin{pmatrix} 0 & 1 & 0 \\ 1 & 0 & 0 \\ 0 & 0 & 0 \end{pmatrix}, \end{aligned} \tag{B.8}$$

where $\mathbf{e}_x$ and $\mathbf{e}_y$ are unit polarization vectors in the xy plane, both perpendicular to $\mathbf{k}$.

B.2 Thin-horizon approximation: analytical solution and asymptotic behavior of tensor modes

In this appendix, we show that the thin-horizon approximation is valid for tensor modes which reenter the horizon during an era with constant w for the EOS of the background universe, the case of most interest to us throughout the ΛSFDM expansion history. For this purpose, we show an example of how well the exact analytical solution matches the asymptotic sub- and superhorizon evolution, in their respective regime of validity (we draw this example from other work in progress, Rindler-Daller, Shapiro, Li, in prep.). Fig. B.1 shows plots of the evolution of $h_k(\tau)$ and $\Omega_{\rm GW}(k, \tau)$ in the case of a matter-like ($w = 0$) EOS of the background universe. We confirm that the range in $k\tau$ around horizon crossing

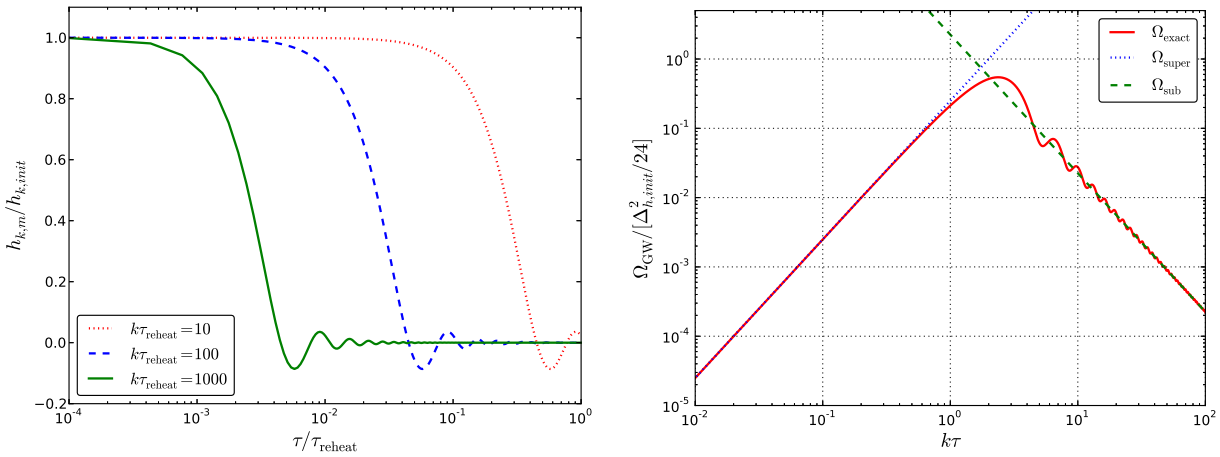

Figure B.1: *Left-hand plot:* Tensor perturbations for different k-modes, as they reenter the horizon during reheating (with $w = 0$) at different times. At $\tau/\tau_{\rm reheat} = 1$, the reheating era gives rise to the stiff era. The tensor modes (strains) are normalized over their initial amplitude $h_{k,\ \rm init}$, for each k. *Right-hand plot:* The exact solution for $\Omega_{\rm GW}(k,\tau)$ as a function of $k\tau$ (solid curve), as well as the respective asymptotic expressions (superhorizon in dot, subhorizon in dash), for a reheating era with $w = 0$. $\Omega_{\rm GW}$ is normalized over $\Delta^2_{h,\ \rm init}/24$.

is rather narrow, justifying the thin-horizon approximation in which the horizon crossing is deemed to occur suddenly at $k = aH(a)/c$ for each k.

B.3 Marginally-allowed ΛSFDM models with given r and $\lambda/(mc^2)^2$: $f_{\rm reheat} \propto T_{\rm reheat}$

It can be analytically shown that for ΛSFDM models which marginally satisfy the cosmological constraints, with given values of r and $\lambda/(mc^2)^2$, $f_{\rm reheat}$ is nearly proportional to $T_{\rm reheat}$.

First, let us express $f_{\rm reheat}$ as follows:

$$f_{\rm reheat} = \frac{f_{\rm reheat}}{f_{\rm sr}} \frac{f_{\rm sr}}{f_{\rm r,late}} f_{\rm r,late}, \tag{B.9}$$

where $f_{\rm sr}$ is the frequency of the mode that reenters the horizon (approximately) at $a_{\rm sr} = 2\pi f_{\rm sr}/H_{\rm sr}$, the transition between the stiff-SFDM-dominated era and the radiation-dominated era, and $f_{\rm r,late}$ is the frequency of a mode that reenters later in the radiation-dominated era at $a_{\rm r,late} = 2\pi f_{\rm r,late}/H_{\rm r,late}$. Both $f_{\rm r,late}$ and $a_{\rm r,late}$ are required to be the same for all models, the feasibility of which is guaranteed by the fact that these marginally-allowed ΛSFDM models share a uniform expansion history in the radiation-dominated era, since the values of r and $\lambda/(mc^2)^2$ are fixed.

Since the area of the triangle in $\Omega_{\rm GW}(f)$ is almost constant, the triangle itself must be almost identical for all marginally-allowed ΛSFDM models, as the slopes of the two "sides" of the triangle are fixed by the power-law indices. In other words, they can be approximated by the same triangle which slides on a fixed plateau, whose height is determined by the value of r alone. Thus, the ratio $f_{\rm reheat}/f_{\rm sr}$ must be the same for all marginally-allowed models, since the x-axis in the $\Omega_{\rm GW}(f)$ plots is logarithmic. This implies that the number of e-foldings between $a_{\rm reheat}$ and $a_{\rm sr}$ must be the same as well, shown by the following equation:

$$\begin{aligned}\frac{f_{\rm reheat}}{f_{\rm sr}} &= \frac{a_{\rm reheat}H_{\rm reheat}}{a_{\rm sr}H_{\rm sr}} = \left(\frac{a_{\rm reheat}}{a_{\rm sr}}\right)\left(\frac{a_{\rm reheat}}{a_{\rm sr}}\right)^{-3} \\ &= \left(\frac{a_{\rm reheat}}{a_{\rm sr}}\right)^{-2}. \end{aligned} \tag{B.10}$$

Also,

$$\begin{aligned}\frac{f_{\rm sr}}{f_{\rm r,late}} &= \frac{a_{\rm sr}H_{\rm sr}}{a_{\rm r,late}H_{\rm r,late}} = \left(\frac{a_{\rm sr}}{a_{\rm r,late}}\right)\left(\frac{a_{\rm sr}}{a_{\rm r,late}}\right)^{-2} \\ &= \left(\frac{a_{\rm sr}}{a_{\rm reheat}}\right)^{-1}\left(\frac{a_{\rm reheat}}{a_{\rm r,late}}\right)^{-1}. \end{aligned} \tag{B.11}$$

Combining the above two equations yields

$$\begin{aligned} f_{\rm reheat} &= f_{\rm r,late}\left(\frac{a_{\rm reheat}}{a_{\rm sr}}\right)^{-2}\left(\frac{a_{\rm sr}}{a_{\rm reheat}}\right)^{-1}\left(\frac{a_{\rm reheat}}{a_{\rm r,late}}\right)^{-1} \\ &= f_{\rm r,late}\left(\frac{a_{\rm reheat}}{a_{\rm sr}}\right)^{-1}\left(\frac{a_{\rm reheat}}{a_{\rm r,late}}\right)^{-1} \\ &\propto a_{\rm reheat}^{-1}. \end{aligned} \tag{B.12}$$

Since $T_{\rm reheat} \propto a_{\rm reheat}^{-1}$ to a very good accuracy, ignoring the details in the thermal history of the universe, we conclude that $f_{\rm reheat} \propto T_{\rm reheat}$, for all marginally-allowed ΛSFDM models with fixed r and $\lambda/(mc^2)^2$.

B.4 Calculating the expected SNR and the integrated sensitivity curve for a given SGWB signal for aLIGO/Virgo with the noise characteristics from the completed O1 run

B.4.1 Expected signal-to-noise ratio

According to [147], a potential SGWB signal can be detected by cross-correlating the strain outputs of two laser interferometric GW detectors, e.g., the Advanced LIGO/Virgo experiment [119, 142]. For this study, the expected SNR for a generic SGWB whose spectrum is $\Omega_{\rm GW}(f)$ today can be derived as [147] [1]

$$\mathrm{SNR} = \frac{3H_0^2}{10\pi^2}\sqrt{2T}\left[\int_0^\infty \mathrm{d}f \left(\frac{\gamma^2(f)}{f^6 P_1(f) P_2(f)}\right)\Omega_{\rm GW}^2(f)\right]^{1/2}, \tag{B.13}$$

where $P_1(f)$ and $P_2(f)$ are the one-sided strain noise power spectral densities of the two detectors; $\gamma(f)$ is the normalized isotropic overlap reduction function [154, 155]; and T is the accumulated coincident observation time. $T = 29.85$ days for the O1 run. Eq. (B.13) is consistent with Eq. (21) in [148] and can be rearranged into

$$\mathrm{SNR} = \sqrt{2T}\left[\int_0^\infty \mathrm{d}f \frac{\Omega_{\rm GW}^2(f)}{\Omega_{\rm eff}^2(f)}\right]^{1/2}, \tag{B.14}$$

[1] For simplicity, the treatment described in this Appendix applies for a cross-correlation study with only two detectors, as is the case for the completed aLIGO O1 run. However, for a network of detectors (i.e., no less than three detectors, as is the case for the full aLIGO/Virgo experiment after Virgo comes online), this treatment can be easily generalized to combine the SNR values from each pair of detectors, as shown by [148].

where $\Omega_{\rm eff}(f)$ is defined as

$$\Omega_{\rm eff}(f) \equiv \frac{10\pi^2}{3H_0^2}\left(\frac{\gamma^2(f)}{f^6 P_1(f) P_2(f)}\right)^{-1/2}. \tag{B.15}$$

Therefore, calculating the SNR for a given SGWB amounts to determining the function $\Omega_{\rm eff}(f)$ which basically reflects the noise characteristics of a given observing run. For future observing runs, e.g. aLIGO/Virgo O5, one can estimate the noise characteristics and provide a theoretical prediction of $\Omega_{\rm eff}(f)$, as shown by [148], to calculate the expected SNR for a given SGWB signal using Eq. (B.14). However, since the aLIGO O1 run is already completed, it is reasonable to replace the theoretical function of $\Omega_{\rm eff}(f)$ with the actual noise characteristics from the O1 run data [142], as explained below.

It is shown, for example, in [145] (a cross-correlation analysis for two colocated LIGO detectors with data from the initial LIGO S5 run) that $\Omega_{\rm eff}(f)$ can be related to the expectation value of the variance of the frequency-dependent estimator for the amplitude of a flat SGWB signal ($\Omega_{\rm GW}(f) = \Omega_0$), as follows:

$$\Omega_{\rm eff}^2(f) = (2T\Delta f) \cdot \sigma_{\hat{\Omega}_0}^2(f), \tag{B.16}$$

where Δf is the width of the frequency bin, and $\sigma_{\hat{\Omega}_0}^2(f)$ is the variance of the estimator $\hat{\Omega}_0(f)$ in each frequency bin. A detailed derivation of the equation above can be found in [147]. While the function $\Omega_{\rm eff}(f)$ depends *only* upon the noise characteristics of the experiment of interest, independent from the spectral form of the SGWB signal, Eq. (B.16) implies that one can use $\Omega_{\rm eff}(f)$ to construct frequency-dependent variance estimators for power-law SGWB spectra, and, particularly, $\Omega_{\rm eff}(f)$ is encoded in the variance estimator, $\sigma_{\hat{\Omega}_0}^2(f)$, for the flat spectrum. We communicated with the LIGO Scientific Collaboration with regard to

the noise characteristics (encoded in) $\sigma^2_{\hat{\Omega}_0}(f)$ in the recently reported SGWB analysis with O1 data (plotted in Fig. 1 of [142]), which they kindly provided us for the entire frequency range ($20 - 1726$ Hz) to which the aLIGO O1 run is sensitive. The width of the frequency bin in their analysis is $\Delta f = 0.031$ Hz. We are thus able to calculate the expected SNR for the inflationary SGWB predicted in our ΛSFDM model as follows:

$$\mathrm{SNR} = \left(\sum_{f=f_{\rm min}}^{f_{\rm max}} \frac{\Omega^2_{\rm GW}(f)}{\sigma^2_{\hat{\Omega}_0}(f)} \right)^{1/2}, \tag{B.17}$$

where the summation is over the frequency bins of $\sigma^2_{\hat{\Omega}_0}(f)$. We use Eq. (B.17) to calculate the expected SNR for any given SGWB signal for the completed aLIGO O1 run.

B.4.2 Integrated Sensitivity Curves

The construction of the frequency-integrated sensitivity curves for the inflationary SGWB spectrum predicted in ΛSFDM is analogous to the procedure developed in [148] where they constructed the sensitivity curves for arbitrary power-law spectra, $\Omega_{\rm GW}(f) \propto f^\beta$. However, as described in §2.5.1, the SGWB from inflation predicted in our model has a triangle-shaped feature with fixed slopes, which can be parametrized as the following broken power-law spectrum:

$$\Omega_{\rm GW}(f) = \begin{cases} \Omega_{\rm GW}(f_{\rm reheat}) \left(\dfrac{f}{f_{\rm reheat}} \right), & f \lesssim f_{\rm reheat}, \quad \text{(B.18)} \\ \dfrac{9\pi}{64} \cdot \Omega_{\rm GW}(f_{\rm reheat}) \left(\dfrac{f}{f_{\rm reheat}} \right)^{-2}, & f > f_{\rm reheat}. \quad \text{(B.19)} \end{cases}$$

As explained in §2.5.1, at $f = f_{\rm reheat}$, the SGWB spectrum has the maximum value, $\Omega_{\rm GW}(f_{\rm reheat})$, which corresponds to the peak of the triangle. Therefore, to construct a sen-

sitivity curve with a fixed value of SNR, e.g. SNR = 1, we can carry out the following procedure.

1. We choose a sample of values of $f_{\rm reheat}$ over a frequency range which includes the available range of the noise characteristics, $(f_{\rm min},\ f_{\rm max})$. For each value of $f_{\rm reheat}$, we calculate the corresponding value of $\Omega_{\rm GW}(f_{\rm reheat})$ which yields that fixed SNR, using Eq. (B.14) or (B.17).

2. For each pairs of values for $f_{\rm reheat}$ and $\Omega_{\rm GW}(f_{\rm reheat})$ in the sample, plot the spectrum $\Omega_{\rm GW}(f)$ using Eqs. (B.18) and (B.19). The envelope of these spectra yields the integrated sensitivity curve for the inflationary SGWB in ΛSFDM with the fixed SNR.

The interpretation of these integrated sensitivity curves is as follows (repeating the description in §2.5.1): for the curve with SNR = 1, for example, if the predicted $\Omega_{\rm GW}(f)$ for the inflationary SGWB from a given set of ΛSFDM model parameters touches the curve for the O1(O5) run at any f, this SGWB will be detected with 1σ significance (SNR = 1) by the O1(O5) run, respectively. These curves are plotted in Figs. 2.8 – 2.10. The O1 curve uses the actual noise characteristics from data while the O5 curve is based on the theoretical prediction of $\Omega_{\rm eff}(f)$ provided by [148].

Bibliography

[1] B. Li, T. Rindler-Daller, and P. R. Shapiro. Cosmological constraints on Bose-Einstein-condensed scalar field dark matter. *Phys. Rev. D*, 89(8):083536, April 2014.

[2] M. W. Goodman and E. Witten. Detectability of certain dark-matter candidates. *Phys. Rev. D*, 31:3059–3063, June 1985.

[3] R. J. Scherrer and M. S. Turner. On the relic, cosmic abundance of stable, weakly interacting massive particles. *Phys. Rev. D*, 33:1585–1589, March 1986.

[4] A. K. Drukier, K. Freese, and D. N. Spergel. Detecting cold dark-matter candidates. *Phys. Rev. D*, 33:3495–3508, June 1986.

[5] E. Komatsu, K. M. Smith, J. Dunkley, C. L. Bennett, B. Gold, G. Hinshaw, N. Jarosik, D. Larson, M. R. Nolta, L. Page, D. N. Spergel, M. Halpern, R. S. Hill, A. Kogut, M. Limon, S. S. Meyer, N. Odegard, G. S. Tucker, J. L. Weiland, E. Wollack, and E. L. Wright. Seven-year Wilkinson Microwave Anisotropy Probe (WMAP) Observations: Cosmological Interpretation. *Astrophys. J. Suppl. Ser.*, 192:18, February 2011.

[6] G. Hinshaw, D. Larson, E. Komatsu, D. N. Spergel, C. L. Bennett, J. Dunkley, M. R. Nolta, M. Halpern, R. S. Hill, N. Odegard, L. Page, K. M. Smith, J. L. Weiland, B. Gold, N. Jarosik, A. Kogut, M. Limon, S. S. Meyer, G. S. Tucker, E. Wollack, and

E. L. Wright. Nine-year Wilkinson Microwave Anisotropy Probe (WMAP) Observations: Cosmological Parameter Results. *Astrophys. J. Suppl. Ser.*, 208:19, October 2013.

[7] Planck Collaboration, P. A. R. Ade, N. Aghanim, C. Armitage-Caplan, M. Arnaud, M. Ashdown, F. Atrio-Barandela, J. Aumont, C. Baccigalupi, A. J. Banday, and et al. Planck 2013 results. XVI. Cosmological parameters. *Astron.& Aastrophys.*, 571:A16, November 2014.

[8] L. Anderson, E. Aubourg, S. Bailey, D. Bizyaev, M. Blanton, A. S. Bolton, J. Brinkmann, J. R. Brownstein, A. Burden, A. J. Cuesta, L. A. N. da Costa, K. S. Dawson, R. de Putter, D. J. Eisenstein, J. E. Gunn, H. Guo, J.-C. Hamilton, P. Harding, S. Ho, K. Honscheid, E. Kazin, D. Kirkby, J.-P. Kneib, A. Labatie, C. Loomis, R. H. Lupton, E. Malanushenko, V. Malanushenko, R. Mandelbaum, M. Manera, C. Maraston, C. K. McBride, K. T. Mehta, O. Mena, F. Montesano, D. Muna, R. C. Nichol, S. E. Nuza, M. D. Olmstead, D. Oravetz, N. Padmanabhan, N. Palanque-Delabrouille, K. Pan, J. Parejko, I. Pâris, W. J. Percival, P. Petitjean, F. Prada, B. Reid, N. A. Roe, A. J. Ross, N. P. Ross, L. Samushia, A. G. Sánchez, D. J. Schlegel, D. P. Schneider, C. G. Scóccola, H.-J. Seo, E. S. Sheldon, A. Simmons, R. A. Skibba, M. A. Strauss, M. E. C. Swanson, D. Thomas, J. L. Tinker, R. Tojeiro, M. V. Magaña, L. Verde, C. Wagner, D. A. Wake, B. A. Weaver, D. H. Weinberg, M. White, X. Xu, C. Yèche, I. Zehavi, and G.-B. Zhao. The clustering of galaxies in the SDSS-III Baryon Oscillation Spectroscopic Survey: baryon acoustic oscillations in the Data Release 9 spectroscopic galaxy sample. *Mon. Not. Roy. Astron. Soc.*, 427:3435–3467, December 2012.

[9] A. G. Sánchez, C. G. Scóccola, A. J. Ross, W. Percival, M. Manera, F. Montesano, X. Mazzalay, A. J. Cuesta, D. J. Eisenstein, E. Kazin, C. K. McBride, K. Mehta, A. D. Montero-Dorta, N. Padmanabhan, F. Prada, J. A. Rubiño-Martín, R. Tojeiro, X. Xu, M. V. Magaña, E. Aubourg, N. A. Bahcall, S. Bailey, D. Bizyaev, A. S. Bolton, H. Brewington, J. Brinkmann, J. R. Brownstein, J. R. Gott, J. C. Hamilton, S. Ho, K. Honscheid, A. Labatie, E. Malanushenko, V. Malanushenko, C. Maraston, D. Muna, R. C. Nichol, D. Oravetz, K. Pan, N. P. Ross, N. A. Roe, B. A. Reid, D. J. Schlegel, A. Shelden, D. P. Schneider, A. Simmons, R. Skibba, S. Snedden, D. Thomas, J. Tinker, D. A. Wake, B. A. Weaver, D. H. Weinberg, M. White, I. Zehavi, and G. Zhao. The clustering of galaxies in the SDSS-III Baryon Oscillation Spectroscopic Survey: cosmological implications of the large-scale two-point correlation function. *Mon. Not. Roy. Astron. Soc.*, 425:415–437, September 2012.

[10] M. G. Walker, M. Mateo, E. W. Olszewski, J. Peñarrubia, N. Wyn Evans, and G. Gilmore. A Universal Mass Profile for Dwarf Spheroidal Galaxies? *Astrophy. J.*, 704:1274–1287, October 2009.

[11] A. B. Newman, T. Treu, R. S. Ellis, D. J. Sand, C. Nipoti, J. Richard, and E. Jullo. The Density Profiles of Massive, Relaxed Galaxy Clusters. I. The Total Density Over Three Decades in Radius. *Astrophy. J.*, 765:24, March 2013.

[12] A. Vikhlinin, R. A. Burenin, H. Ebeling, W. R. Forman, A. Hornstrup, C. Jones, A. V. Kravtsov, S. S. Murray, D. Nagai, H. Quintana, and A. Voevodkin. Chandra Cluster Cosmology Project. II. Samples and X-Ray Data Reduction. *Astrophy. J.*, 692:1033–1059, February 2009.

[13] D. H. Weinberg, J. S. Bullock, F. Governato, R. Kuzio de Naray, and A. H. G. Peter. Cold dark matter: Controversies on small scales. *Proceedings of the National Academy of Science*, 112:12249–12255, October 2015.

[14] A. Klypin, A. V. Kravtsov, O. Valenzuela, and F. Prada. Where Are the Missing Galactic Satellites? *Astrophy. J.*, 522:82–92, September 1999.

[15] B. Moore, S. Ghigna, F. Governato, G. Lake, T. Quinn, J. Stadel, and P. Tozzi. Dark Matter Substructure within Galactic Halos. *Astrophy. J. Letter*, 524:L19–L22, October 1999.

[16] V. Springel, J. Wang, M. Vogelsberger, A. Ludlow, A. Jenkins, A. Helmi, J. F. Navarro, C. S. Frenk, and S. D. M. White. The Aquarius Project: the subhaloes of galactic haloes. *Mon. Not. Roy. Astron. Soc.*, 391:1685–1711, December 2008.

[17] M. Boylan-Kolchin, V. Springel, S. D. M. White, A. Jenkins, and G. Lemson. Resolving cosmic structure formation with the Millennium-II Simulation. *Mon. Not. Roy. Astron. Soc.*, 398:1150–1164, September 2009.

[18] J. F. Navarro, C. S. Frenk, and S. D. M. White. A Universal Density Profile from Hierarchical Clustering. *Astrophy. J.*, 490:493, December 1997.

[19] B. Moore, T. Quinn, F. Governato, J. Stadel, and G. Lake. Cold collapse and the core catastrophe. *Mon. Not. Roy. Astron. Soc.*, 310:1147–1152, December 1999.

[20] W. J. G. de Blok, S. S. McGaugh, A. Bosma, and V. C. Rubin. Mass Density Profiles of Low Surface Brightness Galaxies. *Astrophy. J. Letter*, 552:L23–L26, May 2001.

[21] S.-H. Oh, W. J. G. de Blok, F. Walter, E. Brinks, and R. C. Kennicutt, Jr. High-Resolution Dark Matter Density Profiles of THINGS Dwarf Galaxies: Correcting for Noncircular Motions. *Astron. J.*, 136:2761–2781, December 2008.

[22] N. C. Amorisco and N. W. Evans. Dark matter cores and cusps: the case of multiple stellar populations in dwarf spheroidals. *Mon. Not. Roy. Astron. Soc.*, 419:184–196, January 2012.

[23] D. Bauer, J. Buckley, M. Cahill-Rowley, R. Cotta, A. Drlica-Wagner, J. L. Feng, S. Funk, J. Hewett, D. Hooper, A. Ismail, M. Kaplinghat, A. Kusenko, K. Matchev, D. McKinsey, T. Rizzo, W. Shepherd, T. M. P. Tait, A. M. Wijangco, and M. Wood. Dark matter in the coming decade: Complementary paths to discovery and beyond. *Physics of the Dark Universe*, 7:16–23, March 2015.

[24] K. Griest and M. Kamionkowski. Supersymmetric dark matter. *Physics Reports*, 333:167–182, August 2000.

[25] G. Aad, T. Abajyan, B. Abbott, J. Abdallah, S. Abdel Khalek, O. Abdinov, R. Aben, B. Abi, M. Abolins, O. S. AbouZeid, and et al. Search for new phenomena in final states with large jet multiplicities and missing transverse momentum at TeV proton-proton collisions using the ATLAS experiment. *Journal of High Energy Physics*, 10:130, October 2013.

[26] CMS Collaboration. Search for gluino mediated bottom- and top-squark production in multijet final states in pp collisions at 8 TeV. *ArXiv e-prints*, May 2013.

[27] S. Weinberg. *Cosmology*. Oxford University Press, 2008.

[28] P. Sikivie. An argument that the dark matter is axions. *ArXiv e-prints*, September 2012.

[29] S. M. Carroll. Quintessence and the Rest of the World: Suppressing Long-Range Interactions. *Physical Review Letters*, 81:3067–3070, October 1998.

[30] N. Arkani-Hamed, S. Dimopoulos, and G. Dvali. Phenomenology, astrophysics, and cosmology of theories with submillimeter dimensions and TeV scale quantum gravity. *Phys. Rev. D*, 59(8):086004, April 1999.

[31] R. Kallosh, A. Linde, S. Prokushkin, and M. Shmakova. Supergravity, dark energy, and the fate of the universe. *Phys. Rev. D*, 66(12):123503, December 2002.

[32] A. Arvanitaki, S. Dimopoulos, S. Dubovsky, N. Kaloper, and J. March-Russell. String axiverse. *Phys. Rev. D*, 81(12):123530, June 2010.

[33] T. Harko. Cosmological dynamics of dark matter Bose-Einstein condensation. *Phys. Rev. D*, 83(12):123515, June 2011.

[34] T. Fukuyama and M. Morikawa. Stagflation: Bose-Einstein condensation in the early universe. *Phys. Rev. D*, 80(6):063520, September 2009.

[35] J. I. Kapusta. Bose-Einstein condensation, spontaneous symmetry breaking, and gauge theories. *Phys. Rev. D*, 24:426–439, July 1981.

[36] H. E. Haber and H. A. Weldon. Finite-temperature symmetry breaking as Bose-Einstein condensation. *Phys. Rev. D*, 25:502–525, January 1982.

[37] L. P. Pitaevskii and S. Stringari. *Bose-Einstein Condensation*. International Series of Monographs on Physics. Clarendon Press, 2003.

[38] P. Sikivie and Q. Yang. Bose-Einstein Condensation of Dark Matter Axions. *Physical Review Letters*, 103(11):111301, September 2009.

[39] O. Erken, P. Sikivie, H. Tam, and Q. Yang. Cosmic axion thermalization. *Phys. Rev. D*, 85(6):063520, March 2012.

[40] S.-J. Sin. Late-time phase transition and the galactic halo as a Bose liquid. *Phys. Rev. D*, 50:3650–3654, September 1994.

[41] J.-W. Lee and I.-G. Koh. Galactic halos as boson stars. *Phys. Rev. D*, 53:2236–2239, February 1996.

[42] J. Goodman. Repulsive dark matter. *New Astronomy*, 5:103–107, April 2000.

[43] W. Hu, R. Barkana, and A. Gruzinov. Fuzzy Cold Dark Matter: The Wave Properties of Ultralight Particles. *Physical Review Letters*, 85:1158–1161, August 2000.

[44] J. Magaña, T. Matos, A. Suárez, and F. J. Sánchez-Salcedo. Structure formation with scalar field dark matter: the field approach. *J. Cosm. Astropart. Phys.*, 10:003, October 2012.

[45] T. Rindler-Daller and P. R. Shapiro. Angular momentum and vortex formation in Bose-Einstein-condensed cold dark matter haloes. *Mon. Not. Roy. Astron. Soc.*, 422:135–161, May 2012.

[46] P. H. Chavanis. Growth of perturbations in an expanding universe with Bose-Einstein condensate dark matter. *Astron.& Aastrophys.*, 537:A127, January 2012.

[47] L. H. Ford. Gravitational particle creation and inflation. *Phys. Rev. D*, 35:2955–2960, May 1987.

[48] P. J. E. Peebles and A. Vilenkin. Quintessential inflation. *Phys. Rev. D*, 59(6):063505, March 1999.

[49] P. J. E. Peebles. Fluid Dark Matter. *Astrophy. J. Letter*, 534:L127–L129, May 2000.

[50] J. A. Frieman, C. T. Hill, and R. Watkins. Late-time cosmological phase transitions: Particle-physics models and cosmic evolution. *Phys. Rev. D*, 46:1226–1238, August 1992.

[51] A. Arbey, J. Lesgourgues, and P. Salati. Cosmological constraints on quintessential halos. *Phys. Rev. D*, 65(8):083514, April 2002.

[52] T. Rindler-Daller and P. R. Shapiro. Finding New Signature Effects on Galactic Dynamics to Constrain Bose-Einstein-Condensed Cold Dark Matter. In C. Moreno González, J. E. Madriz Aguilar, and L. M. Reyes Barrera, editors, *Accelerated Cosmic Expansion*, volume 38 of *Astrophysics and Space Science Proceedings*, page 163, 2014.

[53] N. C. Amorisco, A. Agnello, and N. W. Evans. The core size of the Fornax dwarf spheroidal. *Mon. Not. Roy. Astron. Soc.*, 429:L89–L93, February 2013.

[54] T.-P. Woo and T. Chiueh. High-Resolution Simulation on Structure Formation with Extremely Light Bosonic Dark Matter. *Astrophy. J.*, 697:850–861, May 2009.

[55] M. Joyce. Electroweak baryogenesis and the expansion rate of the Universe. *Phys. Rev. D*, 55:1875–1878, February 1997.

[56] S. Dutta and R. J. Scherrer. Big bang nucleosynthesis with a stiff fluid. *Phys. Rev. D*, 82(8):083501, October 2010.

[57] G. Steigman. Neutrinos And Big Bang Nucleosynthesis. *ArXiv e-prints*, July 2012.

[58] L. A. Boyle, R. R. Caldwell, and M. Kamionkowski. Spintessence! New models for dark matter and dark energy. *Physics Letters B*, 545:17–22, October 2002.

[59] P. J. E. Peebles and A. Vilenkin. Noninteracting dark matter. *Phys. Rev. D*, 60(10):103506, November 1999.

[60] J. Magaña and T. Matos. A brief Review of the Scalar Field Dark Matter model. *Journal of Physics Conference Series*, 378(1):012012, August 2012.

[61] M. S. Turner. Coherent scalar-field oscillations in an expanding universe. *Phys. Rev. D*, 28:1243–1247, September 1983.

[62] T. Matos and L. Arturo Ureña-López. Further analysis of a cosmological model with quintessence and scalar dark matter. *Phys. Rev. D*, 63(6):063506, March 2001.

[63] M. Colpi, S. L. Shapiro, and I. Wasserman. Boson stars - Gravitational equilibria of self-interacting scalar fields. *Physical Review Letters*, 57:2485–2488, November 1986.

[64] W. Hu and N. Sugiyama. Anisotropies in the cosmic microwave background: an analytic approach. *Astrophy. J.*, 444:489–506, May 1995.

[65] G. Mangano, G. Miele, S. Pastor, T. Pinto, O. Pisanti, and P. D. Serpico. Relic neutrino decoupling including flavour oscillations. *Nuclear Physics B*, 729:221–234, November 2005.

[66] C. G. Böhmer and T. Harko. Can dark matter be a Bose Einstein condensate? *J. Cosm. Astropart. Phys.*, 6:025, June 2007.

[67] S. Bashinsky and U. Seljak. Signatures of relativistic neutrinos in CMB anisotropy and matter clustering. *Phys. Rev. D*, 69(8):083002, April 2004.

[68] B. Ratra and P. J. E. Peebles. Cosmological consequences of a rolling homogeneous scalar field. *Phys. Rev. D*, 37:3406–3427, June 1988.

[69] D. J. H. Chung, L. L. Everett, and K. T. Matchev. Inflationary cosmology connecting dark energy and dark matter. *Phys. Rev. D*, 76(10):103530, November 2007.

[70] Y. B. Zeldovich. The equation of state at ultrahigh densities and its relativistic limitations. *Sov. Phys. JETP*, 14(5):1143–1147, May 1962. (original in Russian).

[71] Y. B. Zeldovich. A hypothesis, unifying the structure and the entropy of the Universe. *Mon. Not. Roy. Astron. Soc.*, 160:1P, 1972.

[72] M. Kamionkowski and M. S. Turner. Thermal relics: Do we know their abundances? *Phys. Rev. D*, 42:3310–3320, November 1990.

[73] M. I. Khlopov, B. A. Malomed, and I. B. Zeldovich. Gravitational instability of scalar fields and formation of primordial black holes. *Mon. Not. Roy. Astron. Soc.*, 215:575–589, August 1985.

[74] B. Li, P. R. Shapiro, and T. Rindler-Daller. Bose-Einstein-condensed scalar field dark matter and the gravitational wave background from inflation: new cosmological constraints and its detectability by LIGO. *Phys. Rev. D,* in press (published online August 2017 issue), *arXiv:* 1611.07961, November 2016.

[75] Planck Collaboration, P. A. R. Ade, N. Aghanim, M. Arnaud, M. Ashdown, J. Aumont, C. Baccigalupi, A. J. Banday, R. B. Barreiro, J. G. Bartlett, and et al. Planck 2015 results. XIII. Cosmological parameters. *Astron.& Aastrophys.*, 594:A13, September 2016.

[76] É. Aubourg, S. Bailey, J. E. Bautista, F. Beutler, V. Bhardwaj, D. Bizyaev, M. Blanton, M. Blomqvist, A. S. Bolton, J. Bovy, H. Brewington, J. Brinkmann, J. R. Brownstein, A. Burden, N. G. Busca, W. Carithers, C.-H. Chuang, J. Comparat, R. A. C. Croft, A. J. Cuesta, K. S. Dawson, T. Delubac, D. J. Eisenstein, A. Font-Ribera, J. Ge, J.-M. Le Goff, S. G. A. Gontcho, J. R. Gott, J. E. Gunn, H. Guo, J. Guy, J.-C. Hamilton, S. Ho, K. Honscheid, C. Howlett, D. Kirkby, F. S. Kitaura, J.-P. Kneib, K.-G. Lee, D. Long, R. H. Lupton, M. V. Magaña, V. Malanushenko, E. Malanushenko, M. Manera, C. Maraston, D. Margala, C. K. McBride, J. Miralda-Escudé, A. D. Myers, R. C. Nichol, P. Noterdaeme, S. E. Nuza, M. D. Olmstead, D. Oravetz, I. Pâris, N. Padmanabhan, N. Palanque-Delabrouille, K. Pan, M. Pellejero-Ibanez, W. J. Percival, P. Petitjean, M. M. Pieri, F. Prada, B. Reid, J. Rich, N. A. Roe, A. J. Ross, N. P. Ross, G. Rossi, J. A. Rubiño-Martín, A. G. Sánchez, L. Samushia, R. T. G. Santos, C. G. Scóccola, D. J. Schlegel, D. P. Schneider, H.-J. Seo, E. Sheldon, A. Simmons, R. A. Skibba, A. Slosar, M. A. Strauss, D. Thomas, J. L. Tinker, R. Tojeiro, J. A.

Vazquez, M. Viel, D. A. Wake, B. A. Weaver, D. H. Weinberg, W. M. Wood-Vasey, C. Yèche, I. Zehavi, G.-B. Zhao, and BOSS Collaboration. Cosmological implications of baryon acoustic oscillation measurements. *Phys. Rev. D*, 92(12):123516, December 2015.

[77] S. Alam, M. Ata, S. Bailey, F. Beutler, D. Bizyaev, J. A. Blazek, A. S. Bolton, J. R. Brownstein, A. Burden, C.-H. Chuang, J. Comparat, A. J. Cuesta, K. S. Dawson, D. J. Eisenstein, S. Escoffier, H. Gil-Marín, J. N. Grieb, N. Hand, S. Ho, K. Kinemuchi, D. Kirkby, F. Kitaura, E. Malanushenko, V. Malanushenko, C. Maraston, C. K. McBride, R. C. Nichol, M. D. Olmstead, D. Oravetz, N. Padmanabhan, N. Palanque-Delabrouille, K. Pan, M. Pellejero-Ibanez, W. J. Percival, P. Petitjean, F. Prada, A. M. Price-Whelan, B. A. Reid, S. A. Rodríguez-Torres, N. A. Roe, A. J. Ross, N. P. Ross, G. Rossi, J. A. Rubiño-Martín, S. Saito, S. Salazar-Albornoz, L. Samushia, A. G. Sánchez, S. Satpathy, D. J. Schlegel, D. P. Schneider, C. G. Scóccola, H.-J. Seo, E. S. Sheldon, A. Simmons, A. Slosar, M. A. Strauss, M. E. C. Swanson, D. Thomas, J. L. Tinker, R. Tojeiro, M. V. Magaña, J. A. Vazquez, L. Verde, D. A. Wake, Y. Wang, D. H. Weinberg, M. White, W. M. Wood-Vasey, C. Yèche, I. Zehavi, Z. Zhai, and G.-B. Zhao. The clustering of galaxies in the completed SDSS-III Baryon Oscillation Spectroscopic Survey: cosmological analysis of the DR12 galaxy sample. *Mon. Not. Roy. Astron. Soc.*, 470:2617–2652, September 2017.

[78] A. Vikhlinin, A. V. Kravtsov, R. A. Burenin, H. Ebeling, W. R. Forman, A. Hornstrup, C. Jones, S. S. Murray, D. Nagai, H. Quintana, and A. Voevodkin. Chandra Cluster Cosmology Project III: Cosmological Parameter Constraints. *Astrophy. J.*, 692:1060–1074, February 2009.

[79] J. Wolf, G. D. Martinez, J. S. Bullock, M. Kaplinghat, M. Geha, R. R. Muñoz, J. D. Simon, and F. F. Avedo. Accurate masses for dispersion-supported galaxies. *Mon. Not. Roy. Astron. Soc.*, 406:1220–1237, August 2010.

[80] A. B. Newman, R. S. Ellis, and T. Treu. Luminous and Dark Matter Profiles from Galaxies to Clusters: Bridging the Gap with Group-scale Lenses. *Astrophy. J.*, 814:26, November 2015.

[81] W. J. G. de Blok, F. Walter, E. Brinks, C. Trachternach, S.-H. Oh, and R. C. Kennicutt, Jr. High-Resolution Rotation Curves and Galaxy Mass Models from THINGS. *Astron. J.*, 136:2648–2719, December 2008.

[82] S.-H. Oh, D. A. Hunter, E. Brinks, B. G. Elmegreen, A. Schruba, F. Walter, M. P. Rupen, L. M. Young, C. E. Simpson, M. C. Johnson, K. A. Herrmann, D. Ficut-Vicas, P. Cigan, V. Heesen, T. Ashley, and H.-X. Zhang. High-resolution Mass Models of Dwarf Galaxies from LITTLE THINGS. *Astron. J.*, 149:180, June 2015.

[83] K. A. Oman, J. F. Navarro, L. V. Sales, A. Fattahi, C. S. Frenk, T. Sawala, M. Schaller, and S. D. M. White. Missing dark matter in dwarf galaxies? *Mon. Not. Roy. Astron. Soc.*, 460:3610–3623, August 2016.

[84] M. Boylan-Kolchin, J. S. Bullock, and M. Kaplinghat. Too big to fail? The puzzling darkness of massive Milky Way subhaloes. *Mon. Not. Roy. Astron. Soc.*, 415:L40–L44, July 2011.

[85] M. Boylan-Kolchin, J. S. Bullock, and M. Kaplinghat. The Milky Way's bright satellites as an apparent failure of ΛCDM. *Mon. Not. Roy. Astron. Soc.*, 422:1203–1218,

May 2012.

[86] D. S. Akerib, H. M. Araújo, X. Bai, A. J. Bailey, J. Balajthy, P. Beltrame, E. P. Bernard, A. Bernstein, T. P. Biesiadzinski, E. M. Boulton, A. Bradley, R. Bramante, S. B. Cahn, M. C. Carmona-Benitez, C. Chan, J. J. Chapman, A. A. Chiller, C. Chiller, A. Currie, J. E. Cutter, T. J. R. Davison, L. de Viveiros, A. Dobi, J. E. Y. Dobson, E. Druszkiewicz, B. N. Edwards, C. H. Faham, S. Fiorucci, R. J. Gaitskell, V. M. Gehman, C. Ghag, K. R. Gibson, M. G. D. Gilchriese, C. R. Hall, M. Hanhardt, S. J. Haselschwardt, S. A. Hertel, D. P. Hogan, M. Horn, D. Q. Huang, C. M. Ignarra, M. Ihm, R. G. Jacobsen, W. Ji, K. Kazkaz, D. Khaitan, R. Knoche, N. A. Larsen, C. Lee, B. G. Lenardo, K. T. Lesko, A. Lindote, M. I. Lopes, D. C. Malling, A. Manalaysay, R. L. Mannino, M. F. Marzioni, D. N. McKinsey, D.-M. Mei, J. Mock, M. Moongweluwan, J. A. Morad, A. S. J. Murphy, C. Nehrkorn, H. N. Nelson, F. Neves, K. O'Sullivan, K. C. Oliver-Mallory, R. A. Ott, K. J. Palladino, M. Pangilinan, E. K. Pease, P. Phelps, L. Reichhart, C. Rhyne, S. Shaw, T. A. Shutt, C. Silva, V. N. Solovov, P. Sorensen, S. Stephenson, T. J. Sumner, M. Szydagis, D. J. Taylor, W. Taylor, B. P. Tennyson, P. A. Terman, D. R. Tiedt, W. H. To, M. Tripathi, L. Tvrznikova, S. Uvarov, J. R. Verbus, R. C. Webb, J. T. White, T. J. Whitis, M. S. Witherell, F. L. H. Wolfs, K. Yazdani, S. K. Young, C. Zhang, and LUX Collaboration. Improved Limits on Scattering of Weakly Interacting Massive Particles from Reanalysis of 2013 LUX Data. *Physical Review Letters*, 116(16):161301, April 2016.

[87] R. Agnese, A. J. Anderson, T. Aramaki, M. Asai, W. Baker, D. Balakishiyeva, D. Barker, R. Basu Thakur, D. A. Bauer, J. Billard, A. Borgland, M. A. Bowles, P. L. Brink,

R. Bunker, B. Cabrera, D. O. Caldwell, R. Calkins, D. G. Cerdeno, H. Chagani, Y. Chen, J. Cooley, B. Cornell, P. Cushman, M. Daal, P. C. F. Di Stefano, T. Doughty, L. Esteban, S. Fallows, E. Figueroa-Feliciano, M. Ghaith, G. L. Godfrey, S. R. Golwala, J. Hall, H. R. Harris, T. Hofer, D. Holmgren, L. Hsu, M. E. Huber, D. Jardin, A. Jastram, O. Kamaev, B. Kara, M. H. Kelsey, A. Kennedy, A. Leder, B. Loer, E. Lopez Asamar, P. Lukens, R. Mahapatra, V. Mandic, N. Mast, N. Mirabolfathi, R. A. Moffatt, J. D. Morales Mendoza, S. M. Oser, K. Page, W. A. Page, R. Partridge, M. Pepin, A. Phipps, K. Prasad, M. Pyle, H. Qiu, W. Rau, P. Redl, A. Reisetter, Y. Ricci, A. Roberts, H. E. Rogers, T. Saab, B. Sadoulet, J. Sander, K. Schneck, R. W. Schnee, S. Scorza, B. Serfass, B. Shank, D. Speller, D. Toback, R. Underwood, S. Upadhyayula, A. N. Villano, B. Welliver, J. S. Wilson, D. H. Wright, S. Yellin, J. J. Yen, B. A. Young, J. Zhang, and SuperCDMS Collaboration. New Results from the Search for Low-Mass Weakly Interacting Massive Particles with the CDMS Low Ionization Threshold Experiment. *Physical Review Letters*, 116(7):071301, February 2016.

[88] M. Ackermann, A. Albert, B. Anderson, W. B. Atwood, L. Baldini, G. Barbiellini, D. Bastieri, K. Bechtol, R. Bellazzini, E. Bissaldi, R. D. Blandford, E. D. Bloom, R. Bonino, E. Bottacini, T. J. Brandt, J. Bregeon, P. Bruel, R. Buehler, G. A. Caliandro, R. A. Cameron, R. Caputo, M. Caragiulo, P. A. Caraveo, C. Cecchi, E. Charles, A. Chekhtman, J. Chiang, G. Chiaro, S. Ciprini, R. Claus, J. Cohen-Tanugi, J. Conrad, A. Cuoco, S. Cutini, F. D'Ammando, A. de Angelis, F. de Palma, R. Desiante, S. W. Digel, L. Di Venere, P. S. Drell, A. Drlica-Wagner, R. Essig, C. Favuzzi, S. J. Fegan, E. C. Ferrara, W. B. Focke, A. Franckowiak, Y. Fukazawa, S. Funk, P. Fusco,

F. Gargano, D. Gasparrini, N. Giglietto, F. Giordano, M. Giroletti, T. Glanzman, G. Godfrey, G. A. Gomez-Vargas, I. A. Grenier, S. Guiriec, M. Gustafsson, E. Hays, J. W. Hewitt, D. Horan, T. Jogler, G. Jóhannesson, M. Kuss, S. Larsson, L. Latronico, J. Li, L. Li, M. Llena Garde, F. Longo, F. Loparco, P. Lubrano, D. Malyshev, M. Mayer, M. N. Mazziotta, J. E. McEnery, M. Meyer, P. F. Michelson, T. Mizuno, A. A. Moiseev, M. E. Monzani, A. Morselli, S. Murgia, E. Nuss, T. Ohsugi, M. Orienti, E. Orlando, J. F. Ormes, D. Paneque, J. S. Perkins, M. Pesce-Rollins, F. Piron, G. Pivato, T. A. Porter, S. Rainò, R. Rando, M. Razzano, A. Reimer, O. Reimer, S. Ritz, M. Sánchez-Conde, A. Schulz, N. Sehgal, C. Sgrò, E. J. Siskind, F. Spada, G. Spandre, P. Spinelli, L. Strigari, H. Tajima, H. Takahashi, J. B. Thayer, L. Tibaldo, D. F. Torres, E. Troja, G. Vianello, M. Werner, B. L. Winer, K. S. Wood, M. Wood, G. Zaharijas, S. Zimmer, and Fermi-LAT Collaboration. Searching for Dark Matter Annihilation from Milky Way Dwarf Spheroidal Galaxies with Six Years of Fermi Large Area Telescope Data. *Physical Review Letters*, 115(23):231301, December 2015.

[89] A. Drlica-Wagner, A. Albert, K. Bechtol, M. Wood, L. Strigari, M. Sánchez-Conde, L. Baldini, R. Essig, J. Cohen-Tanugi, B. Anderson, R. Bellazzini, E. D. Bloom, R. Caputo, C. Cecchi, E. Charles, J. Chiang, A. de Angelis, S. Funk, P. Fusco, F. Gargano, N. Giglietto, F. Giordano, S. Guiriec, M. Gustafsson, M. Kuss, F. Loparco, P. Lubrano, N. Mirabal, T. Mizuno, A. Morselli, T. Ohsugi, E. Orlando, M. Persic, S. Rainò, N. Sehgal, F. Spada, D. J. Suson, G. Zaharijas, S. Zimmer, Fermi-LAT Collaboration, T. Abbott, S. Allam, E. Balbinot, A. H. Bauer, A. Benoit-Lévy, R. A. Bernstein, G. M. Bernstein, E. Bertin, D. Brooks, E. Buckley-Geer, D. L. Burke, A. Carnero Rosell, F. J. Castander, R. Covarrubias, C. B. D'Andrea, L. N. da Costa, D. L. DePoy, S. Desai,

H. T. Diehl, C. E. Cunha, T. F. Eifler, J. Estrada, A. E. Evrard, A. Fausti Neto, E. Fernandez, D. A. Finley, B. Flaugher, J. Frieman, E. Gaztanaga, D. Gerdes, D. Gruen, R. A. Gruendl, G. Gutierrez, K. Honscheid, B. Jain, D. James, T. Jeltema, S. Kent, R. Kron, K. Kuehn, N. Kuropatkin, O. Lahav, T. S. Li, E. Luque, M. A. G. Maia, M. Makler, M. March, J. Marshall, P. Martini, K. W. Merritt, C. Miller, R. Miquel, J. Mohr, E. Neilsen, B. Nord, R. Ogando, J. Peoples, D. Petravick, A. Pieres, A. A. Plazas, A. Queiroz, A. K. Romer, A. Roodman, E. S. Rykoff, M. Sako, E. Sanchez, B. Santiago, V. Scarpine, M. Schubnell, I. Sevilla, R. C. Smith, M. Soares-Santos, F. Sobreira, E. Suchyta, M. E. C. Swanson, G. Tarle, J. Thaler, D. Thomas, D. Tucker, A. R. Walker, R. H. Wechsler, W. Wester, P. Williams, B. Yanny, J. Zuntz, and The DES Collaboration. Search for Gamma-Ray Emission from DES Dwarf Spheroidal Galaxy Candidates with Fermi-LAT Data. *Astrophy. J. Letter*, 809:L4, August 2015.

[90] T. Rindler-Daller and P. R. Shapiro. Complex Scalar Field Dark Matter on Galactic Scales. *Modern Physics Letters A*, 29:1430002, January 2014.

[91] B. Li, P. R. Shapiro, and T. Rindler-Daller. Complex Scalar Field Dark Matter and its Imprint on Gravitational Waves. In *Proceedings of the Frank N. Bash Symposium 2015 (BASH2015). 18-20 October. The University of Texas at Austin, USA.*, page 28, 2015.

[92] D. J. E. Marsh. Nonlinear hydrodynamics of axion dark matter: Relative velocity effects and quantum forces. *Phys. Rev. D*, 91(12):123520, June 2015.

[93] L. Hui, J. P. Ostriker, S. Tremaine, and E. Witten. Ultralight scalars as cosmological dark matter. *Phys. Rev. D*, 95(4):043541, February 2017.

[94] H.-Y. Schive, T. Chiueh, and T. Broadhurst. Cosmic structure as the quantum interference of a coherent dark wave. *Nature Physics*, 10:496–499, July 2014.

[95] D. J. E. Marsh, E. Macaulay, M. Trebitsch, and P. G. Ferreira. Ultralight axions: Degeneracies with massive neutrinos and forecasts for future cosmological observations. *Phys. Rev. D*, 85(10):103514, May 2012.

[96] R. Hlozek, D. Grin, D. J. E. Marsh, and P. G. Ferreira. A search for ultralight axions using precision cosmological data. *Phys. Rev. D*, 91(10):103512, May 2015.

[97] A. Suárez and T. Matos. Structure formation with scalar-field dark matter: the fluid approach. *Mon. Not. Roy. Astron. Soc.*, 416:87–93, September 2011.

[98] E. Calabrese and D. N. Spergel. Ultra-light dark matter in ultra-faint dwarf galaxies. *Mon. Not. Roy. Astron. Soc.*, 460:4397–4402, August 2016.

[99] Z. Slepian and J. Goodman. Ruling out bosonic repulsive dark matter in thermal equilibrium. *Mon. Not. Roy. Astron. Soc.*, 427:839–849, November 2012.

[100] T. Matos, F. S. Guzmán, and D. Núñez. Spherical scalar field halo in galaxies. *Phys. Rev. D*, 62(6):061301, September 2000.

[101] B. Kain and H. Y. Ling. Cosmological inhomogeneities with Bose-Einstein condensate dark matter. *Phys. Rev. D*, 85(2):023527, January 2012.

[102] A. Suárez and P.-H. Chavanis. Cosmological evolution of a complex scalar field with repulsive or attractive self-interaction. *Phys. Rev. D*, 95(6):063515, March 2017.

[103] D. N. Spergel and P. J. Steinhardt. Observational Evidence for Self-Interacting Cold Dark Matter. *Physical Review Letters*, 84:3760–3763, April 2000.

[104] K. Ahn and P. R. Shapiro. Formation and evolution of self-interacting dark matter haloes. *Mon. Not. Roy. Astron. Soc.*, 363:1092–1110, November 2005.

[105] J. Koda and P. R. Shapiro. Gravothermal collapse of isolated self-interacting dark matter haloes: N-body simulation versus the fluid model. *Mon. Not. Roy. Astron. Soc.*, 415:1125–1137, August 2011.

[106] S. Davidson and M. Elmer. Bose-Einstein condensation of the classical axion field in cosmology? *J. Cosm. Astropart. Phys.*, 12:034, December 2013.

[107] A. H. Guth, M. P. Hertzberg, and C. Prescod-Weinstein. Do dark matter axions form a condensate with long-range correlation? *Phys. Rev. D*, 92(10):103513, November 2015.

[108] G. Mangano, G. Miele, S. Pastor, and M. Peloso. Bose-Einstein condensation at reheating. *Phys. Rev. D*, 64(12):123509, December 2001.

[109] F. Briscese. Viability of complex self-interacting scalar field as dark matter. *Physics Letters B*, 696:315–320, February 2011.

[110] P. G. Ferreira and M. Joyce. Cosmology with a primordial scaling field. *Phys. Rev. D*, 58(2):023503, July 1998.

[111] V. A. Belinsky, L. P. Grishchuk, I. M. Khalatnikov, and Y. B. Zeldovich. Inflationary stages in cosmological models with a scalar field. *Physics Letters B*, 155:232–236, May 1985.

[112] D. Scialom and P. Jetzer. Asymptotic behavior of complex scalar fields in a Friedmann-Lemaitre universe. *Phys. Rev. D*, 51:5698–5706, May 1995.

[113] Planck Collaboration, P. A. R. Ade, N. Aghanim, M. Arnaud, F. Arroja, M. Ashdown, J. Aumont, C. Baccigalupi, M. Ballardini, A. J. Banday, and et al. Planck 2015 results. XX. Constraints on inflation. *Astron.& Aastrophys.*, 594:A20, September 2016.

[114] BICEP2 Collaboration, Keck Array Collaboration, P. A. R. Ade, Z. Ahmed, R. W. Aikin, K. D. Alexander, D. Barkats, S. J. Benton, C. A. Bischoff, J. J. Bock, R. Bowens-Rubin, J. A. Brevik, I. Buder, E. Bullock, V. Buza, J. Connors, B. P. Crill, L. Duband, C. Dvorkin, J. P. Filippini, S. Fliescher, J. Grayson, M. Halpern, S. Harrison, G. C. Hilton, H. Hui, K. D. Irwin, K. S. Karkare, E. Karpel, J. P. Kaufman, B. G. Keating, S. Kefeli, S. A. Kernasovskiy, J. M. Kovac, C. L. Kuo, E. M. Leitch, M. Lueker, K. G. Megerian, C. B. Netterfield, H. T. Nguyen, R. O'Brient, R. W. Ogburn, A. Orlando, C. Pryke, S. Richter, R. Schwarz, C. D. Sheehy, Z. K. Staniszewski, B. Steinbach, R. V. Sudiwala, G. P. Teply, K. L. Thompson, J. E. Tolan, C. Tucker, A. D. Turner, A. G. Vieregg, A. C. Weber, D. V. Wiebe, J. Willmert, C. L. Wong, W. L. K. Wu, and K. W. Yoon. Improved Constraints on Cosmology and Foregrounds from BICEP2 and Keck Array Cosmic Microwave Background Data with Inclusion of 95 GHz Band. *Physical Review Letters*, 116(3):031302, January 2016.

[115] U. Seljak and M. Zaldarriaga. Signature of Gravity Waves in the Polarization of the Microwave Background. *Physical Review Letters*, 78:2054–2057, March 1997.

[116] M. A. Amin, M. P. Hertzberg, D. I. Kaiser, and J. Karouby. Nonperturbative dynamics of reheating after inflation: A review. *International Journal of Modern Physics D*,

24:1530003, December 2015.

[117] L. P. Grishchuk. Amplification of gravitational waves in an isotropic universe. *Zhurnal Eksperimentalnoi i Teoreticheskoi Fiziki*, 67:825–838, 1974.

[118] V. F. Mukhanov, H. A. Feldman, and R. H. Brandenberger. Theory of cosmological perturbations. *Physics Reports*, 215:203–333, June 1992.

[119] B. P. Abbott, R. Abbott, T. D. Abbott, M. R. Abernathy, F. Acernese, K. Ackley, C. Adams, T. Adams, P. Addesso, R. X. Adhikari, and et al. GW150914: Implications for the Stochastic Gravitational-Wave Background from Binary Black Holes. *Physical Review Letters*, 116(13):131102, April 2016.

[120] P. Binétruy, A. Bohé, C. Caprini, and J.-F. Dufaux. Cosmological backgrounds of gravitational waves and eLISA/NGO: phase transitions, cosmic strings and other sources. *J. Cosm. Astropart. Phys.*, 6:027, June 2012.

[121] Z. Arzoumanian, A. Brazier, S. Burke-Spolaor, S. J. Chamberlin, S. Chatterjee, B. Christy, J. M. Cordes, N. J. Cornish, K. Crowter, P. B. Demorest, X. Deng, T. Dolch, J. A. Ellis, R. D. Ferdman, E. Fonseca, N. Garver-Daniels, M. E. Gonzalez, F. Jenet, G. Jones, M. L. Jones, V. M. Kaspi, M. Koop, M. T. Lam, T. J. W. Lazio, L. Levin, A. N. Lommen, D. R. Lorimer, J. Luo, R. S. Lynch, D. R. Madison, M. A. McLaughlin, S. T. McWilliams, C. M. F. Mingarelli, D. J. Nice, N. Palliyaguru, T. T. Pennucci, S. M. Ransom, L. Sampson, S. A. Sanidas, A. Sesana, X. Siemens, J. Simon, I. H. Stairs, D. R. Stinebring, K. Stovall, J. Swiggum, S. R. Taylor, M. Vallisneri, R. van Haasteren,

Y. Wang, W. W. Zhu, and The NANOGrav Collaboration. The NANOGrav Nine-year Data Set: Limits on the Isotropic Stochastic Gravitational Wave Background. *Astrophy. J.*, 821:13, April 2016.

[122] R. M. Shannon, V. Ravi, L. T. Lentati, P. D. Lasky, G. Hobbs, M. Kerr, R. N. Manchester, W. A. Coles, Y. Levin, M. Bailes, N. D. R. Bhat, S. Burke-Spolaor, S. Dai, M. J. Keith, S. Osłowski, D. J. Reardon, W. van Straten, L. Toomey, J.-B. Wang, L. Wen, J. S. B. Wyithe, and X.-J. Zhu. Gravitational waves from binary supermassive black holes missing in pulsar observations. *Science*, 349:1522–1525, September 2015.

[123] L. Lentati, S. R. Taylor, C. M. F. Mingarelli, A. Sesana, S. A. Sanidas, A. Vecchio, R. N. Caballero, K. J. Lee, R. van Haasteren, S. Babak, C. G. Bassa, P. Brem, M. Burgay, D. J. Champion, I. Cognard, G. Desvignes, J. R. Gair, L. Guillemot, J. W. T. Hessels, G. H. Janssen, R. Karuppusamy, M. Kramer, A. Lassus, P. Lazarus, K. Liu, S. Osłowski, D. Perrodin, A. Petiteau, A. Possenti, M. B. Purver, P. A. Rosado, R. Smits, B. Stappers, G. Theureau, C. Tiburzi, and J. P. W. Verbiest. European Pulsar Timing Array limits on an isotropic stochastic gravitational-wave background. *Mon. Not. Roy. Astron. Soc.*, 453:2576–2598, November 2015.

[124] M. Giovannini. Gravitational wave constraints on post-inflationary phases stiffer than radiation. *Phys. Rev. D*, 58(8):083504, October 1998.

[125] M. Giovannini. Spikes in the relic graviton background from quintessential inflation. *Classical and Quantum Gravity*, 16:2905–2913, September 1999.

[126] M. Giovannini. Production and detection of relic gravitons in quintessential inflationary models. *Phys. Rev. D*, 60(12):123511, December 1999.

[127] L. A. Boyle and A. Buonanno. Relating gravitational wave constraints from primordial nucleosynthesis, pulsar timing, laser interferometers, and the CMB: Implications for the early universe. *Phys. Rev. D*, 78(4):043531, August 2008.

[128] L. A. Boyle and P. J. Steinhardt. Probing the early universe with inflationary gravitational waves. *Phys. Rev. D*, 77(6):063504, March 2008.

[129] M. Giovannini. Dynamical backreaction of relic gravitons. *Phys. Rev. D*, 73(8):083505, April 2006.

[130] V. Mukhanov. *Physical Foundations of Cosmology*. November 2005.

[131] C. W. Misner, K. S. Thorne, and J. A. Wheeler. *Gravitation*. 1973.

[132] S. Weinberg. Damping of tensor modes in cosmology. *Phys. Rev. D*, 69(2):023503, January 2004.

[133] D. A. Dicus and W. W. Repko. Comment on "Damping of tensor modes in cosmology". *Phys. Rev. D*, 72(8):088302, October 2005.

[134] B. P. Abbott, R. Abbott, T. D. Abbott, M. R. Abernathy, F. Acernese, K. Ackley, C. Adams, T. Adams, P. Addesso, R. X. Adhikari, and et al. Observation of Gravitational Waves from a Binary Black Hole Merger. *Physical Review Letters*, 116(6):061102, February 2016.

[135] É. É. Flanagan and S. A. Hughes. The basics of gravitational wave theory. *New Journal of Physics*, 7:204, September 2005.

[136] P. N. Brown, G. D. Byrne, and A. C. Hindmarsh. VODE: A Variable-coefficient ODE Solver. *SIAM Journal on Scientific and Statistical Computing*, 10(5):1038–1051, 1989.

[137] A. Suárez, V. H. Robles, and T. Matos. A Review on the Scalar Field/Bose-Einstein Condensate Dark Matter Model. In C. Moreno González, J. E. Madriz Aguilar, and L. M. Reyes Barrera, editors, *Accelerated Cosmic Expansion*, volume 38 of *Astrophysics and Space Science Proceedings*, page 107, 2014.

[138] Y. I. Izotov, T. X. Thuan, and N. G. Guseva. A new determination of the primordial He abundance using the He I λ10830 Å emission line: cosmological implications. *Mon. Not. Roy. Astron. Soc.*, 445:778–793, November 2014.

[139] K. M. Nollett and G. Steigman. BBN and the CMB constrain neutrino coupled light WIMPs. *Phys. Rev. D*, 91(8):083505, April 2015.

[140] R. J. Cooke, M. Pettini, K. M. Nollett, and R. Jorgenson. The Primordial Deuterium Abundance of the Most Metal-poor Damped Lyman-α System. *Astrophy. J.*, 830:148, October 2016.

[141] S. Dodelson. *Modern cosmology*. Academic Press, 2003.

[142] B. P. Abbott, R. Abbott, T. D. Abbott, M. R. Abernathy, F. Acernese, K. Ackley, C. Adams, T. Adams, P. Addesso, R. X. Adhikari, and et al. Upper Limits on the Stochastic Gravitational-Wave Background from Advanced LIGO's First Observing Run. *Physical Review Letters*, 118(12):121101, March 2017.

[143] P. D. Lasky, C. M. F. Mingarelli, T. L. Smith, J. T. Giblin, E. Thrane, D. J. Reardon, R. Caldwell, M. Bailes, N. D. R. Bhat, S. Burke-Spolaor, S. Dai, J. Dempsey, G. Hobbs, M. Kerr, Y. Levin, R. N. Manchester, S. Osłowski, V. Ravi, P. A. Rosado, R. M. Shannon, R. Spiewak, W. van Straten, L. Toomey, J. Wang, L. Wen, X. You, and X. Zhu. Gravitational-Wave Cosmology across 29 Decades in Frequency. *Physical Review X*, 6(1):011035, January 2016.

[144] J. Aasi, B. P. Abbott, R. Abbott, T. Abbott, M. R. Abernathy, T. Accadia, F. Acernese, K. Ackley, C. Adams, T. Adams, and et al. Improved Upper Limits on the Stochastic Gravitational-Wave Background from 2009-2010 LIGO and Virgo Data. *Physical Review Letters*, 113(23):231101, December 2014.

[145] J. Aasi, J. Abadie, B. P. Abbott, R. Abbott, T. Abbott, M. R. Abernathy, T. Accadia, F. Acernese, C. Adams, T. Adams, and et al. Searching for stochastic gravitational waves using data from the two colocated LIGO Hanford detectors. *Phys. Rev. D*, 91(2):022003, January 2015.

[146] P. Amaro-Seoane, S. Aoudia, S. Babak, P. Binétruy, E. Berti, A. Bohé, C. Caprini, M. Colpi, N. J. Cornish, K. Danzmann, J.-F. Dufaux, J. Gair, O. Jennrich, P. Jetzer, A. Klein, R. N. Lang, A. Lobo, T. Littenberg, S. T. McWilliams, G. Nelemans, A. Petiteau, E. K. Porter, B. F. Schutz, A. Sesana, R. Stebbins, T. Sumner, M. Vallisneri, S. Vitale, M. Volonteri, and H. Ward. Low-frequency gravitational-wave science with eLISA/NGO. *Classical and Quantum Gravity*, 29(12):124016, June 2012.

[147] B. Allen and J. D. Romano. Detecting a stochastic background of gravitational radiation: Signal processing strategies and sensitivities. *Phys. Rev. D*, 59(10):102001,

May 1999.

[148] E. Thrane and J. D. Romano. Sensitivity curves for searches for gravitational-wave backgrounds. *Phys. Rev. D*, 88(12):124032, December 2013.

[149] H. Mo, F. C. van den Bosch, and S. White. *Galaxy Formation and Evolution*. Cambridge University Press, May 2010.

[150] J.-A. Gu and W.-Y. P. Hwang. Can the quintessence be a complex scalar field? *Physics Letters B*, 517:1–6, September 2001.

[151] R. A. Isaacson. Gravitational Radiation in the Limit of High Frequency. I. The Linear Approximation and Geometrical Optics. *Physical Review*, 166:1263–1271, February 1968.

[152] R. A. Isaacson. Gravitational Radiation in the Limit of High Frequency. II. Nonlinear Terms and the Effective Stress Tensor. *Physical Review*, 166:1272–1279, February 1968.

[153] Y. Watanabe and E. Komatsu. Improved calculation of the primordial gravitational wave spectrum in the standard model. *Phys. Rev. D*, 73(12):123515, June 2006.

[154] N. Christensen. Measuring the stochastic gravitational-radiation background with laser-interferometric antennas. *Phys. Rev. D*, 46:5250–5266, December 1992.

[155] E. E. Flanagan. Sensitivity of the Laser Interferometer Gravitational Wave Observatory to a stochastic background, and its dependence on the detector orientations. *Phys. Rev. D*, 48:2389–2407, September 1993.